Surface Phase Diagrams Including Anharmonic Effects via a Replica-Exchange Grand-Canonical Method

Vorgelegt von
M. Sc. Yuanyuan Zhou
ORCID: 0000-0001-5268-5644

Von der Fakultät II – Mathematik und Naturwissenschaften
der Technischen Universität Berlin
zur Erlangung des akademischen Grades
Doktorin der Naturwissenschaften
Dr. rer. nat.

Vorgelegte Dissertation

Promotionsausschuss:
Vorsitzende: Prof. Dr. Ulrike Woggon
Gutachterin: Prof. Dr. Sabine Klapp
Gutachterin: Prof. Dr. Claudia Draxl
Gutachter: Prof. Dr. Matthias Scheffler

Tag der wissenschaftlichen Aussprache:

Berlin 2020

献给我挚爱的家人

Abstract

Phase diagrams of surfaces in a reactive atmosphere provide detailed information on surface composition and structure at thermodynamic equilibrium at realistic conditions, e.g., temperature (T) and pressure (p) of the reactive gas. The atomistic structure is a prerequisite to understand and control electronic properties and function of surfaces.

For decades, "*ab initio* atomistic thermodynamic" (aiAT) has been very successful in predicting phase diagrams for surfaces and gas-phase clusters at realistic T, p conditions. The approach was introduced by Scheffler in 1988 and reviewed by Reuter and Scheffler in 2005. However, aiAT phase diagrams usually rely on two approximations: One is that the phase space only consists of a pre-determined list of possible (to be tested) structures compiled by means of informed guess by researchers; the other is that often (but not necessarily) the vibrational contributions from free-energy difference of both substrate and adsorbate are neglected. These approximations do not always yield accurate phase diagram, especially at high temperature and/or coverage. In contrast, an unbiased sampling of the configurational and compositional space could reveal unexpected (metastable) structures. The work in this thesis paves the way towards calculating surface phase diagrams taking accurately into account all anharmonic contributions (e.g., configurational and vibrational entropy), through the unbiased configurational sampling.

To this end, we have developed a Replica-Exchange (RE) Grand-Canonical (GC) algorithm that enables the unbiased calculation of complete temperature-pressure phase diagrams of surfaces or clusters in reactive atmospheres including anharmonic effects. Moreover, the multi-canonical sampling within the given model Hamiltonian yields the T-p dependence of all equilibrium observables, e.g., the radial distribution function, when post-processed with the multistate-Bennet-acceptance-ratio (MBAR) approach. MBAR is the Bolzmann-reweighting-based lowest-variance unbiased estimator of both free energies and ensemble average, introduced in 2008 by Shirts and Chodera. If the unbiased configurational sampling is rigorously conducted in the grand-canonical ensemble, all vibrational contributions can be accurately accounted for.

Our approach is demonstrated for a model of Lennard-Jones system describing a surface in contact with a gas phase. Furthermore, the algorithm is applied to Si_M clusters ($M = 2, 4$) in contact with an H_2 atmosphere, with all interactions described at the *ab initio* level, (density-functional theory with generalized gradient corrected exchange-correlation functional). In both cases, we identify the thermodynamically sta-

ble phases at T, p conditions. As an example of the insight one can achieve by analyzing configurations sampled via REGC, we inspect the formation of regular vs amorphous structures for Lennard-Jones surface adsorbates and we analyze the order-disorder phase transitions. Moreover, the T-p map for other observables (e.g., number of chemisorbed atoms/molecules and HOMO-LUMO gap) can be evaluated without further sampling. We also analyze at which conditions the aiAT approach yields a good approximation of T-p phase diagrams. Finally, we apply REGC to the study of the phases of Si(100) surface in the H_2 atmosphere. The focus of this study is the characterization of the surface and surface+adsorbate structures. The coordination histogram is adopted as the descriptor to distinguish the surface and surface+adsorbate structures with the same composition. This yields a phase diagram populated by several distinct phases including the H-saturated Si(100)-(3×1) phase, which is identified to be thermodynamically stable at around 380 K, in agreement with the reported experimental results. Moreover, we analyze the order-disorder phase transitions and estimate the phase boundary. These results are the first step, though, as performed only on 3×3 lateral supercell and needed to confirmed for a larger system.

The approach introduced in this thesis can be computationally expensive, especially when interactions are described at the *ab initio* level, but it is by construction embarrassingly parallel as the replicas do not communicate among each other except for the inexpensive exchange of thermodynamic variables (T and chemical potential of the gas phase) at each swap. Furthermore, in post-production it allows for diverse analyses, not necessarily planned before starting the unbiased sampling. Overall, our results demonstrate that the method presented in this thesis is a rigorous, innovative approach for studying the phase stability of surfaces and clusters at reactive atmosphere in an automated fashion.

Zusammenfassung

Phasendiagramme von Oberflächen in einer reaktiven Gasatmosphäre liefern detaillierte Informationen über die Zusammensetzung und Struktur der Oberfläche unter realistischen thermodynamischen Bedingungen wie Temperatur und Druck. Dieses atomistische Verständnis ist eine Voraussetzung dafür die elektronischen Eigenschaften von Oberflächen sowie deren Funktion zu verstehen und zu kontrollieren.

Seit Jahrzehnten wird "ab initio atomistic thermodynamics" (aiAT) mit großem Erfolg verwendet um Phasendiagramme für Oberflächen und Gasphasencluster unter realistischen T, p-Bedingungen zu simulieren. Dieser Ansatz wurde erstmals 1988 von Scheffler vorgeschlagen und 2005 von Reuter und Scheffler überarbeitet. Der aiAT-Ansatz beruht jedoch auf zwei Annahmen: Zunächst wird der Phasenraum vor Beginn der Untersuchung aus einer Liste an Teststrukturen gebildet die vom Wissenschaftler als relevant eingeschätzt werden. Desweiteren werden die Schwingungsbeiträge zur Differenz der Freien Energie zwischen der Oberfläche und der Oberfläche mit Adsorbats vernachlässigt oder nur stark vereinfacht berücksichtigt. Im Rahmen dieser Näherungen werden nicht immer genaue Phasendiagramme erzielt, insbesondere bei hoher Temperatur und/oder großer Abdeckung. Im Gegensatz dazu kann ein von diesen Näherungen unabhängiges Sampling des Konfigurations- und Kompositionsraums zur Entdeckung neuer stabiler und metastabiler Strukturen führen. Die hier präsentierte Arbeit ebnet den Weg zur akkuraten Berechnung der Phasendiagramme von Oberflächen unter Berücksichtigung aller anharmonischer Beiträge, d.h. der Konfigurations- und Vibrationsentropie, durch uneingeschränktes Sampling.

Zu diesem Zweck haben wir einen "Replica-Exchange Grand-Canonical"–Algorithmus (REGC) entwickelt der eine uneingeschränkte Berechnung von vollständig temperatur- und druckabhängigen Phasendiagrammen von Oberflächen und Clustern in reaktiven Umgebungen einschließlich anharmonischer Effekte erlaubt. Desweiteren kann durch multikanonisches Sampling die T-p-Abhängigkeit aller Obersvablen im thermischen Gleichgewicht, wie z.B. der radialen Verteilungsfunktion, bestimmt werden, wenn für die Auswertung der "multistate-Bennet-acceptance-ratio" -Ansatz (MBAR) gewählt wird. MBAR wurde 2008 von Shirts und Chodera als Schätzfunktion für die Freie Energie und Ensemble-Mittelwerte eingeführt. Mit einem sorgfältig durchgeführten großkanonischen Sampling lassen sich so alle vibrationellen Beiträge akkurat berücksichtigen.

Wir validieren unseren Ansatz für ein Lennard-Jones-Modell einer Oberfläche in

Kontakt mit einem Gas. Weiterhin wenden wir den Algorithmus auf ein System mit Si_M-Clustern (M=2, 4) in einer H_2-Atmosphäre an, bei dem alle Wechselwirkungen auf ab initio-Level beschrieben werden (Dichtefunktionaltheorie mit Gradienten-korrigiertem Austausch-Korrelations-Funktional). In beiden Fällen identifizieren wir thermodynamisch stabile Phasen bei unterschiedlichen T, p-Bedingungen. Als weiterführendes Beispiel analysieren wir die via REGC gesampleten Konfigurationen und untersuchen die Formation regelmäßiger und amorpher Strukturen für die Lennard-Jones-Oberflächen-Adsorbate und analysieren die Ordnungs-Unordnungs-Übergänge dieses Modells. Weiterhin kann eine T, p-Karte für andere Observablen ohne weiteres Sampling ausgewertet werden, z.B. die Anzahl chemisorbierter Atome und Moleküle oder HOMO-LUMO-Lücke. Wir analysieren unter welchen Bedingungen der aiAT-Ansatz gute Näherungen von T-p-Phasendiagrammen erzielt. Schließlich wenden wir die REGC-Methode an um die Phasen der Si(100)-Oberfläche in H2-Atmosphäre zu untersuchen. Im Mittelpunkt dieser Untersuchung steht die Charakterisierung von Strukturen die sich auf der Oberfläche bilden, mit ohne ohne Adsorbat. Als Deskriptor zur Unterscheidung von Strukturbildung mit und ohne Adsorption bei gleicher chemischer Zusammensetzung werden die Koordinations-Histogramme der Konfiguration genutzt. Somit kann eine Phasendiagramm erstellt werden welches unterschiedliche Phasen aufweist, einschließlich einer H-saturierten Si(100)-(3x1)-Phase welche als thermodynamisch stabil bei ca. 380 K vorhergesagt wird, in Übereinstimmung mit veröffentlichten experimentellen Ergebnissen. Wir analysieren den Ordnungs-Unordnungs-Übergang und schätzen die Phasengrenzen ab. preliminary

Der in dieser Arbeit vorgestelle Ansatz kann zum Zeitpunkt der Fertigstellung als sehr rechenintensiv eingestuft werden, insbesondere wenn alle Wechselwirkungen auf ab initio-Level beschrieben werden. Jedoch ist der Ansatz durch seine Konstruktion trivial parallelisierbar weil die Replikas nur dann kommunizieren müssen wenn der unaufwändige Austausch der thermodynamischen Bedingungen stattfindet. Außerdem können weitere Analysen auf den generierten Daten durchgeführt werden, auch solche die vor Beginn der Simulation noch nicht beabsichtigt waren. Insgesamt zeigen unsere Ergebnisse, dass die in dieser Arbeit präsentierte Methode einen präzisen und innovativen Ansatz für die automatisierte Untersuchung von Oberflächenstrukturen unter realistischen thermodynamischen Bedingungen darstelllt.

Contents

LIST OF ABBREVIATIONS

REGC replica-exchange grand-canonical

RE replica-exchange

GC grand-canonical

MD molecular dynamics

MC monte carlo

MBAR multistate Bennett acceptance ratio

aiAT *ab initio* atomistic thermodynamics

MBAR@REGC post-processing REGC sampling data by MBAR

aiAT@REGC post-processing REGC sampling data by *ab initio* atomistic thermody-
namics

VEA vertical electronic affinity

VIP vertical ionization potential

UHV ultra-high-vacuum

DFT density-functional theory

HOMO highest occupied molecular orbital

LUMO lowest unoccupied molecular orbital

PT parallel tempering

1. Introduction

Surfaces of solids define a boundary between the bulk of a material and its surrounding environment, e.g., liquid or gas phases or vacuum. Compared to the atoms in the bulk, surface atoms have a different chemical environment, that is, fewer nearest neighbors leading to surface reconstructions. The reactions and processes occurring at surfaces play pivotal role to describe a large number of surface phenomena including crystal growth, semiconductor processing, electrochemistry, and heterogeneous catalysis. One of the great motivation for studying chemical reactions on surfaces is to understand heterogeneous catalytic reactions which is at the heart of problem for the sustainable energy development and the production of many important chemicals. The main prerequisites for reaching a microscopic (molecular level) understanding of heterogeneous catalysis are the identification of the composition and geometry of the catalyst's surface and the determination of the various chemical reactions that take place under realistic conditions.

1.1. Pressure gap and materials gap

Heterogeneous catalytic reactions occur on the surface of solid catalysts and involve elementary surface chemical processes such as adsorption of reactants from a reaction mixture, surface diffusion and reaction of adsorbed species, and desorption of reaction products. The acceleration of a chemical reaction is due to the high reactivity of surface atoms that facilitates bond breaking and bond rearrangement of adsorbed molecules. Over the past decades, surface science has undergone revolutionary progress revealing the atomic- and molecular-level structural, dynamic, compositional, and thermodynamic properties of surfaces. Thus it has tremendously advanced the understanding of the nature of catalyst.

In fact, a number of present techniques, widespread in surface science for studying catalytic reactions provide reactivity data for only well-defined single crystals under ultra-high-vacuum (UHV) conditions. To identify the molecular factors that control

selectivity, however, it is required to monitor surface chemical processes under reaction conditions. [1] The pressure of actual industrial reactors is more than 13 orders of magnitude compared to that of UHV. Moreover, there is obvious discontinuity between single-crystal surfaces and practical catalyst for application. These two significant differences have been a long-standing conundrum in the community of heterogeneous catalysis, better known as the *pressure gap* and *materials gap* [2] illustrated in Fig. 1.1. Therefore, the extrapolation of results obtained with well-defined single crystals under UHV conditions to industrial application is not possible. In following sections, we confined the discussion mainly on experimental techniques and theoretical method to bridge the pressure gap.

1.2. In situ surface characterization to bridge the pressure gap

UHV studies on single-crystal surfaces have manifested the power of electron spectroscopy. The instrumentation techniques developed for surface studies include electron-in/electron-out (LEED surface crystallography and Auger electron spectroscopy (AES)), and photon-in/electron-out (XPS), and other such techniques. The theory behind these techniques is that electron travels through the condensed matter and has very short elastic mean free path, to the order of a few atomic distances. As a result, the information of the top first few atomic layers can be obtained by the analysis of emitted and scattered electrons from a surface. However, all of these techniques are limited by high scattering cross sections of electrons that would not allow electrons to survive through high-pressure gas or liquid at the interfaces.

Such limitations are partially circumvented by the in situ surface characterization techniques. Since the 1980s, researchers have worked to develop techniques that can probe the structure, composition, mechanical properties, and dynamics of surfaces at higher (compared to UHV) pressure. [4] The near-ambient pressure (NAP) XPS, for instance, can be operated at total reactant pressure up to 0.01 atm. [5,6] Different from conventional XPS, the kinetic energy of the pumped photoelectrons can be tuned to an appropriate value by varying the energy of the X-ray source. The mean free path can be minimized for the sample surface, thereby, chemical composition of the surface layer with a thickness of ≈ 1 nm can be determined. However, the NAP-XPS offer little information about the structural information of the sample surface. Scanning tunneling microscopy (STM) provides atomic resolution of nanostructures on the surface by measuring the tunneling current between a sharp metallic tip and a conducting sample. Despite the fact that electrons are used to probe surface morphology, the STM is not limited to low pressures as the electrons only have to tunnel through the very narrow gap between the tip and the surface. High-pressure (HP) STM made a significant contribution to bridging the "pressure gap" by monitoring the structure of surfaces and adsorbates on the molecular level during the reactions [7]. A recent developed system in Somorjai's group shows that it is capable of imaging surfaces with atomic resolution under the temperatures ranging from 300 to 700 K and pressures from 10^{-13} atm to several atm. [8] Despite its advantages, HP-STM is just a pure imaging technique and provides little

chemical information.

There are also other in situ characterization techniques, e.g., atomic force microscopy (AFM), but we will not introduce all of them. Despite their own advantages, the working conditions of these in situ techniques still have the distance from the industrial catalytic conditions. For instance, in Haber-Bosch process, the conversion is typically conducted at 150-250 atm while the in situ techniques work under the gas pressure up to several atm. Moreover, each technique also suffers from their own limitation as mentioned above. Last but not least, there is no specific one technique able to provide thorough information including chemical composition, structure, and electronic structure of surface at reaction conditions.

1.3. Theoretical methods to bridge pressure gap

As pointed out, a prerequisite for analyzing and understanding the electronic properties and the function of surfaces is the detailed knowledge of the surface composition and atomistic geometry under realistic conditions. The structure of a surface at thermodynamic equilibrium with its environment is in fact a configurational statistical average over adsorption, desorption, and diffusion processes.

A temperature-pressure phase diagram describes the composition and structure of a system at thermal equilibrium and is an essential tool for understanding material properties. density-functional theory (DFT) is routinely used to calculate various physical properties of a wide range of materials e.g., molecules, bulk solids, and surfaces. The results obtained in DFT calculations, however, represent the total energies including nuclei-nuclei, electrons-nuclei, and electrons-electrons interactions at zero temperature and zero pressure of surrounding gas phase, and thus do not directly relate to catalytically relevant conditions at high pressure and high temperature. In order to account for finite-temperature effects, *ab initio* molecular dynamics (MD) is employed. *Ab initio* here refers to that the forces on all the atoms are evaluated by DFT. The dynamics of the atoms follow the Newton's equation of motion with these calculated forces. However, the computation of *ab initio* MD to sample the canonical distribution of surfaces and its adsorbates is not feasible.

Ab initio thermodynamics, the scheme combining DFT and thermodynamics, was proposed in 1980s [9, 10], and enables us to calculate surface phase diagrams. Later, Reuter *et al.* have described in detail how DFT in combination with thermodynamics

can be used to construct phase diagrams of surface structures as functions of partial gas pressures and temperatures. [11–13] In the approach, the surface free energy, γ, is expressed in terms of the chemical potentials, μ_i of the different species i. Furthermore, μ_i is in turn function of the temperature, T, and the pressure, p_i.

$$\gamma(T,\{p_i\}) = \frac{1}{A}\left[G - \sum_i N_i\mu_i(T, p_i)\right] \tag{1.1}$$

where G is the Gibbs free energy of the solid with the surface of interest. A is the surface area. Here, $\mu_i(T, p_i)$ is the chemical potential of the ith species, and N_i is the number of atoms (molecules) of the ith species in the reservoir. T and $\{p_i\}$ are the temperature and partial pressures of the various species.

The *ab initio* atomistic thermodynamics (aiAT) approach [9–16] has been very successful in predicting phase diagrams for surfaces [12, 13] and gas-phase clusters [17–19] at realistic T, p conditions. The key assumption is that *all* relevant local minima of the potential-energy surface (PES) of a given system are enumerated, a limitation in case of unexpected surface stoichiometries or geometries. Such limitation can only be overcome by an unbiased sampling of configurational and compositional space. A further assumption is that the vibrational contributions are largely cancelled to the change of the free energy from gas particles at the surface to their counterparts in the clean surface, and can be neglected. At most, the vibrational contributions are evaluated at the harmonic or quasi-harmonic level. We will see below that either cancellation or the harmonic approximation is not always justified and does not lead to accurate phase diagram.

In the harmonic approximation [20], the full Hamiltonian is replaced by a harmonic expansion about the equilibrium positions. The vibrational frequencies can then be computed by diagonalization of the dynamical matrix and the thermodynamic function e.g., free energy and heat capacity can be computed from these frequencies. The principal advantages of quasiharmonic theory(QHT) in free-energy calculations are that it is relatively easy to implement, that it requires relatively few calculations. It also includes zero-point vibrations. However, there are two potential shortcomings with this approach. First, the harmonic approximation may break down at higher temperatures. It is also problematic for some systems at low temperature, e.g., the dynamical Jahn-Teller systems [21]. The QHT takes into account only the effect of thermal expansion since the free energy is a function of the volume and can be minimized with respect to this variable for each T - the temperature enters through the Bose-Einstein occupation

of the harmonic phonons, while other sources of anharmonicity are neglected. This picture is in principle valid when phonons do not interact, for example at low T. However, when the temperature increases, phonons undergo mutual scattering, which corresponds to the anharmonic vibrations of atoms. Several studies show that the QHT is not reliable for any of the phases under study at higher temperatures, and explicit anharmonic contributions are key to obtain correct vibrational spectra. [22] The other drawback of QHT is that it only evaluates for one structure at a time, i.e., it does not account for fluxional or liquid-like systems, where the time scale of structural rearrangement (bond breaking and reforming) is short compared to the sampling time.

In this thesis, we introduce a Replica-Exchange (RE) Grand-Canonical (GC) monte carlo (MC)/MD algorithm, that performs largely unbiased sampling in the phase space and enables the efficient calculation of complete temperature-pressure phase diagrams of surfaces, nanoparticles, or clusters in contact with reactive gas atmospheres. The only but significant limitation is the fixed shape and size of the unit cell (super cell) for solid systems. The RE and GC steps of the algorithm are formulated in the Metropolis MC framework, while the canonical sampling of configurations is supported via both MC and MD. In the case of a surface in contact with a gas phase reservoir, the gas molecules can physi-/chemisorb on the surface, while adsorbed molecules or single atoms can desorb from the surface to the gas phase. At thermodynamic equilibrium, the number of desorbed molecules/atoms balances the adsorbed one, so that on average a constant number of molecules/atoms is present on the surface. During the adsorption, the surface itself probably undergoes local re-structuring. We specifically target thermodynamically open systems in the GC ensemble, aiming at describing (nano)structured surfaces in a reactive atmosphere at realistic T, p condition, so that the adsorbate can exchange particles with the gas reservoir. The molecule adsorption on the surface includes the association adsorption where individual molecules remain intact and the dissociative adsorption where the molecule is dissociated into fragments. However, there exist strong activation barriers for ($\sim$ several eV) the dissociation. Here, the dissociation barrier of the molecules is circumvented by allowing the insertion and removal of both molecules and atoms (i.e.,"dissociated molecules") in the GC ensemble. The initial idea of RE [23–26] is to allow for an efficient sampling of the configurational space by shuttling configurations from regions of low T to regions of high T. Later, de Pablo *et al.* [27, 28] extended the concept to other intensive thermodynamic variables, such as the chemical potential (μ) in order to simulate the phase equilibria of Lennard-Jones (LJ) systems.

This allows systems with different number of particles (the conjugate variable of μ) to be shuttled across different values of μ, thus enhancing the sampling, following the same spirit of the temperature replicas in traditional RE. By combining advantages of both GC and RE, our massively parallel algorithm requires no prior knowledge of the phase diagram and takes only the potential energy function together with the desired μ and T ranges as inputs. In practice, the reservoir is modelled as the gas phase imposing temperature T and chemical potential μ on the adsorbed particles and μ depends on T and the pressure p.

The post-processing of the output of the REGC simulation is performed by multistate Bennett Acceptance ratio (MBAR) approach [29] to estimate both free energies and ensemble averages. After a REGC simulation, a series of equilibrium samples are obtained from each thermodynamic state within the GC ensemble. The distribution of each equilibrium sample is normalized, therefore, the mixture distribution obtained by pooling all the distributions together should be also normalized. Under this condition, the normalization constant can be obtained, that is simply the *partition function* in statistical mechanics. Therefore, it is feasible to calculate free energies and expectation averages of observables at any thermodynamic state (T, μ).

The structure of this thesis is as follows. In the first part, the method and flowchart of our REGC algorithm will be discussed in details. In the second chapter, the Replica-Exchange Grand-Canonical method is proposed to perform efficient sampling by relieving the kinetic barriers and diffusional bottleneck. The following chapter includes a brief introduction of grand-canonical ensemble and how it is applied to surfaces in a gas-phase environment. Later, we review the history of replica-exchange method and its theoretical background. The fifth chapter lays out the theoretical framework for our replica-exchange grand-canonical algorithm. Then the MC moves or MD after each replica or particle exchange to relax the configuration will be explained in detail. The next chapter addresses the theoretical method to describe the potential-energy surface (PES), in particular, the force-field approach and density-functional theory. Chapter 8 describes how to use replica-exchange grand-canonical simulations to calculate phase diagrams and free-energy surfaces. The last chapter of part I addresses the implementation for REGC.

In the part II of this thesis, we show three applications of the REGC method. The first, in chapter 10, proof-of-concept application is the determination of the T-p phase diagram of a LJ (frozen) surface in contact with a LJ gas phase. The model aims to

mimic the interaction between a gas-phase particles and a substrate.

Next, in chapter 11, we address the calculation of the phase diagram of the Si_M cluster ($M = 2,\ 4$) in a H_2 gas phase. This is an *ab initio* REGC study using the Perdew-Burke-Ernzerhof (PBE) [30] exchange-correlation (xc) functional. The binary clusters of silicon and hydrogen are thought to be present in porous silicon and hydrogenated amorphous silicon. [31] During the last several decades, numerous efforts were devoted to identify the ground-state structure for different size and the corresponding electronic properties. [31–33] However, little knowledge has been obtained on the thermodynamic stability of silicon clusters in a hydrogen gas phase. Therefore, the purpose of this application is to investigate the phase diagrams of silicon hydrides in reactive hydrogen atmosphere.

Chapter 12 describes an extensive (still ongoing) application of our approach to the Si(100) surface in contact with H_2. Also this is a full DFT-PBE study. The preliminary but promising results reveal the evolution of surface structure at realistic T, p_{H_2} conditions. In particular, the H-saturated Si(100)-(3×1) phase is identified to be the most stable phase at 380 K, which is in excellent agreement with reported experimental results. [34] In the future work, the finite-size effect on the reconstruction and adsorption patterns of Si(100) surface structure in the reactive H_2 gas atmosphere should be taken into account.

In the conclusions and outlook chapter, we discuss the capabilities and current limitations of our REGC method. An outlook includes the ideas and suggestions for future development and remaining challenges.

Part I.

Methodology

2. Replica-Exchange Grand-Canonical Monte Carlo / Molecular Dynamics

The sampling of systems composed of many atoms arranged in molecules, clusters, condensed phases, etc., remains a challenge. The main factors that limit sampling efficiency is (i) that systems' configurations get easily trapped in local minima especially at low temperatures and (ii) the inherently long characteristic diffusion times in many-atoms systems (e.g., atoms' diffusion that require collective motions involving several degrees of freedom). During the last decades, many powerful methods have been developed to deal with the first difficulty, e.g., J-walking [35, 36], multicanonical sampling [37, 38], nested sampling [39], simple tempering [24, 40], 1/k sampling [41], Wang-Landau sampling [42], expanded ensembles [43], and parallel tempering [23, 26]. While these methods are effective in overcoming kinetic barriers, they do little to "accelerate" the slow diffusion at low temperatures.

Open ensembles, described at equilibrium by the grand-canonical-ensemble formalism, provide an effective mean to overcome slow-diffusion problems: Atoms can get in and out of a system, effectively generating thermodynamically possible defects, along unphysical pathways (e.g., atoms' insertion or removal), thereby circumventing diffusional bottlenecks by disentangling degrees of freedom. Another difficulty for the molecule adsorption on the surface is the strong ($\sim$ several eV) activation barriers for the molecular dissociation. In our approach, the dissociation barrier of the molecules is circumvented by allowing the insertion and removal of both molecules and atoms (i.e.,"dissociated molecules") in the GC ensemble. The approach that are developed and implemented in this thesis includes both the replica-exchange and grand-canonical-ensemble concepts to deal with both kinetic trapping and slow phase space diffusion.

Our Replica-Exchange Grand-Canonical Monte Carlo or Molecular-Dynamics approach is outlined in Fig. 2.1. In a REGCMC or REGCMD simulation, S replicas of the original system of interest are considered, each evolving in a different thermodynamic states (T_i , μ_i, where i is the index of the replica). In the present discussion,

we limit ourselves to a single species exchanged with the reservoir, but a generalization to more reservoir is straightforward. During the simulation, first the system has a probability x_0 ($0 \leq x_0 \leq 1$) to attempt exchanging a particle with the reservoir and the replica-exchange move is set to $(1-x_0)$ (see below). After the particle-/replica-exchange attempt, S parallel molecular dynamics or Monte Carlo runs follow, to relax the configuration in the canonical ensemble. i.e., at temperature T_i, with fixed number of particles N and volume V of the system (NVT ensemble). Then, the procedure is iterated until convergence of defined quantities is achieved. Currently the convergence criterion we adopted is that the distribution of the adsorption energy at each thermodynamic (T_i, μ_i) does not change when more REGC steps are performed.

Figure 2.1.: The flow chart of the Replica-Exchange Grand-Canonical Monte Carlo/Molecular Dynamics algorithm. Here rand is a pseudo-random number generated uniformly distributed between 0 and 1.

In principle, the REGC approach shares the same idea with that of *ab initio* atomistic thermodynamics (aiAT) to deal with the problem that a surface is in contact with a gas phase. In the aiAT approach, the gas environment is regared as a reservoir of constant p and T, while the gas phase acts also as a reservoir of constant μ and T in our REGC method. Essentially, the relationship between μ, T, and p is $\mu(p,T) = k_B T \ln(p/p_0)$ is the same, where p_0 is chosen such that $-k_B T \ln(p_0)$ summarizes all the pressure-independent components of μ, i.e., translational, rotational, vibrational etc. degrees of freedom. [12, 17, 44] and k_B is the Boltzmann constant. However, in the aiAT method, the calculation of the Gibbs free energy relies on two approximations: One is only some of pre-selected structures considered; The other is that the vibrational contribution is neglected or treated at harmonic approximation. These approximations do not always result in accurate phase diagram, especially at high temperature and/or coverage. However, our developed REGC method enable to perform largely unbiased sampling, thereby, all vibrational contributions can be accounted for accurately.

3. Grand-Canonical Monte Carlo

This chapter describes the implementation of how each replica exchanges particles with the reservoir in the Grand-Canonical scheme from the theory behind to practical techniques.

Statistical mechanics is based on the *Gibbs' ensemble* concept. That is, the macroscopic observables of a system is simply the averaged quantity over a large number of identical systems, each in a different microscopic configuration. The thermodynamic variables that characterize an ensemble can be regarded as experimental control parameters that specify the conditions under which an experiment is performed. For instance, the microcanonical ensemble and is characterized by constant particle number (N), constant volume (V), and constant total energy (E). Other examples include the canonical (NVT) ensemble, the isothermal-isobaric (NPT) ensemble, and the grand canonical (μVT) ensemble.

When a surface is in contact with a realistic atmosphere, e.g., a molecular hydrogen gas, molecules or atom after dissociation from the environment can physically/chemically adsorb on the surface, and adsorbed atoms or molecules on the surface can be released into the environment. The structure of a surface at thermodynamic equilibrium with its environment is in fact a configurational statistical average over adsorption, desorption, and diffusion processes. For such adsorption studies, a natural ensemble to use is the grand-canonical ensemble.

A grand canonical ensemble is constructed by building a collection of systems in a large heat bath at temperature T and a large reservoir of molecules. Every system can exchange energy and particle with its surroundings. The number of particles in the system, therefore, is different in various states of the system. After the equilibrium is reached, the whole ensemble equilibrates with the its surroundings with respect to the heat and matter transport, thereby, each system is represented by its volume V, and the temperature (T) and chemical potential (μ) of the reservoir. For the more than one species, the chemical potential of each is the same from system to system.

A system is specified by not only in which quantum state j (a set of particles'

positions), but also the number of particles (N) in the system. Each value of $\{N, j\}$ has a particular energy-level set $\{E_{N,j}(V)\}$ corresponding to it. $a_{N,j}$ is defined to be the number of systems in the ensemble that have N particles and are in state j and is also named as occupation number. A distribution is a set of occupation numbers $\{\boldsymbol{a}\} = \{a_{N,1}, a_{N,2}, ..., a_{N,j}, ...\}$.

$$\sum_N \sum_j a_{N,j} = \mathscr{A} \tag{3.1}$$

$$\sum_N \sum_j a_{N,j} E_{N,j} = \mathscr{E} \tag{3.2}$$

$$\sum_N \sum_j a_{N,j} N = \mathscr{M} \tag{3.3}$$

$\mathscr{A}$, $\mathscr{E}$ and $\mathscr{M}$ signify the total number of systems in the ensemble, the total energy of the ensemble, and the total number of particles in the ensemble.

Any ensemble obeys the principle of equal a priori probabilities. That is, an isolated system is equally likely to be in any of its possible quantum states and all possible quantum states satisfy the conservation of mass in Eq. (3.3) and the conservation of energy in Eq. (3.2). Here it means that every distribution of occupation numbers $\{\boldsymbol{a}\}$ is equally probable and must be given equal weight in performing ensemble averages. $W(\boldsymbol{a})$ is the number of ways that $\mathscr{A}$ *distinguishable* objects arranged into groups.

$$W(\boldsymbol{a}) = \frac{\mathscr{A}!}{\prod_N \prod_j a_{N,j}!} \tag{3.4}$$

The most probable distribution $a_{N,j}^*$ that maximizes W under the constraints of Eqs. (3.1), (3.2) and (3.3) can be obtained by applying the method of Lagrange multipliers. The deriviation details of $a_{N,j}^*$ are thoroughly explained in Ref. [45].

$$a_{N,j}^* = e^{\mu \beta N} e^{-\beta E_{N,j}(V)} \tag{3.5}$$

where $\beta = 1/k_{\mathrm{B}} T$.

The particle insertion/removal step is handled by applying the formalism of the grand-canonical ensemble, where the subsystem of our interest (e.g., a surface or a cluster in contact with a gas phase), defined in a volume (V), is in equilibrium with a reservoir at given temperature (T), and chemical potential (μ) of one species (or more species, each with its own chemical potential). In practice, the reservoir is modeled as an ideal gas (where "ideal" refers to the lack of inter-molecular interactions, the intra-molecular

vibrations are still taken into account). The one-to-one mapping of gas chemical potential to its pressure is the same as that of *ab initio* atomistic thermodynamics [9,10], as will be specified in the application cases. The number of atoms or molecules in the subsystem is a fluctuating variable, determined by specifying the chemical potential and temperature of the reservoir of (quasi ideal) gas-phase atoms or molecules. The probability density of a grand-canonical ensemble of identical particles is: [46]

$$\mathscr{N}_{\mu,V,T}(\boldsymbol{R}; N) \propto \frac{e^{(\beta \mu N)} V^N}{\Lambda^{3N} N!} e^{[-\beta E(\boldsymbol{R};N)]} \tag{3.6}$$

where $\Lambda = h/\sqrt{2\pi m k_{\mathrm{B}} T}$ is the thermal wavelength of a particle of mass m, and $E(\boldsymbol{R})$ is the potential energy of a configuration $\boldsymbol{R}$ of the N-particle system. The GCMC algorithm consists of the following MC moves: 1) insertion of a gas atom/molecule into the system at a random position, 2) removal of a randomly selected gas atom/molecule from the system, 3) displacement of a gas atom to a new random position in the system to sample the potential energy surface (PES). In our algorithm, the displacement is taken care of separately and can be done via either Metropolis MC (see section 6.1) or MD (see section 6.2). Here, we consider the insertion and removal moves, where microscopic reversibility (also called 'detailed balance', a *sufficient* condition for an MC scheme to converge the evaluation of observable properties in the desired ensemble [46]) is ensured by having equal number of insertion and removal attempts, for all particles described by the given chemical potential.

The configurations where the molecules are dissociated are accessible when the insertion and removal of both molecules and atoms (i.e., dissociated molecules) are allowed. Therefore, the dissociation barrier has been fully circumvented. The surface is in thermodynamic (constrained) equilibrium with an environment, which indicates that the direct formation of gas molecules by gas atoms are ignored because of its negligible rate. [12,13] The atoms from the substrate can be also exchanged with the reservoir by simply adding the chemical potential of the atom species forming the substrate. This is the solution adopted within the *ab initio* atomistic thermodynamics approach and and will be implemented in REGC in the near future. In this thesis, only one gas species is considered and the atom in the substrate is not involved in the exchange.

In practice, we first randomly select if a particle will be inserted or removed, i.e., by generating a pseudo-random number y_1^{GC} uniformly distributed between 0 and 1 and performing a removal if $y_1^{\mathrm{GC}} < 0.5$.

15

For a removal, a particle (an atom or a molecule) is selected at random (by generating a new random number y_2^{GC} and selecting particle i if $(i-1)/N \leq y_2^{\mathrm{GC}} < i/N$). In order to fulfill detailed balance, a possible (and common) choice for accepting the removal of the selected particle is with probability [46]:

$$P_{(N \to N-1)} = \min\left[1, \frac{\Lambda^3 N}{V} e^{-\beta[\mu + E_{N-1} - E_N]}\right] \tag{3.7}$$

where N is the number of atoms (or molecules) for which a reservoir at given temperature T and chemical potential μ is defined, and which are in the system before the attempted removal. E_N is the energy of the system of N particles, E_{N-1} is the energy of the same system, without the selected particle, and V is the system volume, which is fixed during the simulation. According to this formula, if the change in energy due to the particle removal is similar in value to μ, there is a high probability that the removal is accepted.

For the insertion, first a location is randomly chosen, uniformly in the simulation volume (in a rectangular cell, by driving three independent uniformly distributed random numbers, one for each Cartesian coordinate). Then, a particle is positioned in the selected location and its insertion is accepted with probability [46]:

$$P_{(N \to N+1)} = \min\left[1, \frac{V}{\Lambda^3 (N+1)} e^{-\beta[\mu - E_{N+1} - E_N]}\right] \tag{3.8}$$

The probability of accepting an insertion can be low in dense systems as random locations will have high probability to end up too close to already present atoms, henceforth yielding large, positive values of $(E_{N+1} - E_N)$ and consequent rejection of the insertion. Since we are modeling adsorption on surfaces or clusters in contact with a gas phase, we have a relatively rarefied system, especially if the considered volume of particle insertion (and removal) does not include the subsurface (see further).

4. Replica Exchange

To investigate systems with rugged free-energy landscapes with numerous minima and large free-energy barriers, standard Metropolis MC or molecular dynamics simulations are computationally not feasible and lead to incomplete sampling of configuration space. For example, a straightforward application of MD to sample the canonical distribution of surfaces will be either trapped in metastable minima of the potential-energy surface or locked in some region of the phase space due to diffusional bottlenecks. The diffusional bottlenecks can be alleviated by open ensemble, the framework of which is explained in detail in chapter 3. Methods to overcome the kinetic barriers are demanding. Many methods have developed to relief the kinetic trapping in the context of atomistic simulations. Classified accordingly to their philosophy to overcome barrier, these methods usually belong to two general categories: (*i*) adding biased terms to the Hamiltonian of the original system such as metadynamics [47, 48], umbrella sampling [49, 50], and accelerated molecular dynamics [51–53]; (*ii*) constructing a generalized ensemble of the original system. In a generalized ensemble simulation, a broader sampling of the potential energy is performed instead of only the canonical probability distribution. Simulated tempering [54], multicanonical sampling [37] and parallel tempering (PT) [55, 56], also referred to replica exchange (RE) are classified into this category.

The methods in the first category are efficient to sample the conformational dynamics along reaction coordinates or a few collective variables. The appropriate choice for these parameters is crucial for accurate calculations, [58] however, it is not trivial to choose proper collective variables for a complex simulation. Additionally, there is a reported issue with convergence, as it is non-trivial to determine the point at which sampling should stop, resulting in errors in the estimated free-energy surface. [59]

Among the second category, Simulated tempering and multicanonical sampling in the second category overcome the multiple-minima problem by introducing a random walk in the phase space based on non-Boltzmann probability weight factors. Random walks allow the simulation to pass any energy barrier and to sample a much wider phase space than by conventional methods. These two generalized-ensemble methods are pow-

erful, but, the probability weight factors are not a priori known and the process to determine these factors can be non-trivial and tedious by iterations of short trial simulations. In replica exchange, the weight factor is essentially known before the simulation and there is no complication in its determination.

Figure 4.2.: Energy histograms for a model system at five different temperatures. Overlap of energy distributions between neighboring replicas ensures the swapping acceptance ratio between all adjacent replicas. The image is from Ref. [57].

4.1. History and Formalism of Replica Exchange

The original idea of the parallel tempering (PT) was proposed by Swendsen and Wang in 1986 [60] and generalized by Geyer in 1991 [61]. The use of PT in interdisciplinary fields spanning physics, chemistry, biology, engineering, and material sciences rapidly increases. [55, 62–69]

As illustrated in Fig. 4.1, a typical replica exchange simulation has L replicas of the studied system, each in the canonical ensemble at different temperature, T_l. A replica is a set of atomic atoms of the specific configuration. During the RE simulation, configurations (replicas) swap the thermodynamic states (e.g., T) between each other. Generally, $T_1 < T_2 < \cdots < T_L$, and T_1 is normally the temperature of the system of interest. Then a extended (generalized) ensemble is established, that is the combination of all L subsystems. The partition function of this extended ensemble is the product of all individual NVT_l canonical ensembles:

$$Q_{\text{extended canonical}} = \prod_{l=1}^{L} \frac{1}{\Lambda_l^{3N} N!} \int d\boldsymbol{R}\, e^{-\beta_l E(\boldsymbol{R};N)} \tag{4.1}$$

where $\beta_l = 1/k_{\mathrm{B}}T_l$, $\Lambda = h/\sqrt{2\pi m k_{\mathrm{B}}T}$ is the thermal wavelength of a particle of mass m, and $E(\boldsymbol{R})$ is the potential energy of a configuration $\boldsymbol{R}$ (the atomic positions of the system) of the N-particle system. If the probability of performing a swap move is equal for all conditions, exchanges between ensembles i and j are accepted with the probability;

$$P_{[\beta_i \to \beta_j]} = \min\left[1, e^{[-(\beta_j - \beta_i)(E(\boldsymbol{R}_i) - E(\boldsymbol{R}_j))]}\right] \tag{4.2}$$

Swaps are normally attempted between systems with neighboring temperatures , $j = i + 1$. An important advantage of replica exchange over simulated annealing is that the ensemble average can be evaluated since RE satisfied the detailed balance condition. [70] There are constant-temperature MC moves between swap moves. The swap moves can be performed either with a certain probability or after a fixed number of constant-temperature MC moves. Both cases satisfy the detailed balance condition. [70] The constant-temperature MC moves can be also replaced by molecular dynamics. In the REMD, not only particles' positions but also their momenta are taken into account. There is no pre-selection of barriers and pathways. In the REMD proposed by Sugita

and Okamoto [56], the momenta should be updated after every successful exchange and determined as

$$p^{(i)'} = \sqrt{\frac{T_{new}}{T_{old}}} p^{(i)} \tag{4.3}$$

where $p^{(i)}$ are the old momenta of replica i. T_{old} and T_{new} are the temperatures of replica before and after swap, respectively. The momenta update procedure ensures that the average kinetic energy remains equal to $\frac{3}{2} N k_B T$. The acceptance rule of REMD follows the same as that for REMC and also satisfies detailed balance.

4.2. Open Issues of Replica Exchange

The open question of PT is how to select the number of replicas and the temperature intervals in a parallel tempering simulations. What we wish is to achieve the optimal sampling with the minimum amount of computational cost. In a replica exchange calculation, an optimal sampling means that (i) the highest temperature must be high enough in order to ensure that no replicas get trapped in metastable minima and (ii) the overlaps of energy histograms between all adjacent replicas must be large enough to ensure that acceptance of the exchange between neighboring replicas as shown in Fig. 4.2.

There are several studies to address how to choose optimal temperature sequence. As illustrated in Fig. 4.3, the black square indicates the whole phase space denoted by Γ. The while region indicates the configuration space at high temperature, while the gray disconnected region indicates the low-temperature configuration space. The black lines are the high-temperature (T_{H}) and low-temperature (T_{L}) trajectories, respectively. The swap is therefore accepted when the high-temperature trajectory occasionally crosses into one of the low-temperature subregions. Accordingly, the acceptance rate is related to the fraction of these low-temperature subregions occupying in the high-temperature subregions. The size of regions strongly correlates with the entropy of corresponding system at respective temperature. Thus, in the entropy-related model [71–73], the average acceptance probability is in relation to the entropy difference as below,

$$\overline{P}_{\mathrm{acc}} \sim e^{(-\Delta S/k)} \tag{4.4}$$

The commonly used geometric distribution [74] is considered to be a good approximation for the optimal choice of temperatures under the condition that the specific heat of the

Figure 4.3.: Phase space as they pertain to the replica exchange method. The large black square represents all of phase or configuration space. The large white region inside it depicts the set of configurations important to the high-temperature system, while the disconnected gray regions are those important to the low-temperature system. Lines portray trajectories followed by a high- or low-temperature simulation. The image is from Ref. [71]

studied system is approximately constant. Several iterative methods have been proposed to ensure that the acceptance rates remain within acceptable range. For example, a target acceptance ratio, P_{target} [75]can be calculated iteratively by

$$P_{\text{target}} = e^{(\frac{\Delta\beta}{\Delta E})} \qquad (4.5)$$

where ΔE is the difference of the average energies of temperature-adjacent replicas.

An acceptance rate of 20% is observed to yield the best performance for a variety of systems including a coarse-grained protein, an atomistic model polypeptide, and the Lennard-Jones fluid, which indicate additional replicas can not improve the accuracy of the simulation at given computational time. [76]

23

5. Replica Exchange in a Grand-Canonical ensemble

We define an extended ensemble that is the collection of $S = L \times M$ replica of a given system, arranged in L values of temperature and M values of the chemical potential, as illustrated in Fig. 5.1(a). In this thesis, we consider only one species that exchange particles with the reservoir. The generalization of the method to study more than one gas species is straightforward.

5.1. Formalism of Replica-Exchange in a Grand-Canonical ensemble

The *partition function* of this extended ensemble is the product of the partition functions of the individual (μ_m, V, T_l) ensembles, where $l = 1, 2, \ldots, L$ and $m = 1, 2, \ldots, M$:

$$Q_{\text{extended}} = \prod_{l=1}^{L} \prod_{m=1}^{M} \frac{e^{\beta_l \mu_m N_{l,m}} V^{N_{l,m}}}{\Lambda_l^{3N_{l,m}} N_{l,m}!} \int d\boldsymbol{R} \, e^{-\beta_l E\left(\boldsymbol{R}; N_{l,m}\right)} \tag{5.1}$$

In the following, we label the temperature by T_l or $\beta_l = 1/k_{\text{B}} T_l$. The key observation is that taking one configuration along the evolution of a replica at given (μ_m, V, T_l), statistical mechanics defines the probability that the same configuration belongs to the another state (μ_o, V, T_k). We now randomly select a pair of replicas. The replica at state (μ_m, V, T_l) is in configuration $\boldsymbol{R}_i$ (positions of all atoms of system in (μ_m, V, T_l) and represented by the $3 \times N_{l,m}$ matrix of coordinates) and the replica at state (μ_o, V, T_k) is in configuration $\boldsymbol{R}_j$. We then aim at defining a rule for accepting the swap of the configurations between the two replicas, in order to satisfy the detailed balance in the extended ensemble. To the purpose, one has to impose the following equality:

$$\mathscr{N}_{(\beta_l,\mu_m,\boldsymbol{R}_i)}\mathscr{N}_{(\beta_k,\mu_o,\boldsymbol{R}_j)} \times P_{[(\beta_l,\mu_m,\boldsymbol{R}_i),(\beta_k,\mu_o,\boldsymbol{R}_j)\rightarrow(\beta_l,\mu_m,\boldsymbol{R}_j),(\beta_k,\mu_o,\boldsymbol{R}_i)]} =$$
$$\mathscr{N}_{(\beta_l,\mu_m,\boldsymbol{R}_j)}\mathscr{N}_{(\beta_k,\mu_o,\boldsymbol{R}_i)} \times P_{[(\beta_l,\mu_m,\boldsymbol{R}_j),(\beta_k,\mu_o,\boldsymbol{R}_i)\rightarrow(\beta_l,\mu_m,\boldsymbol{R}_i),(\beta_k,\mu_o,\boldsymbol{R}_j)]} \tag{5.2}$$

where $\mathscr{N}$ is the probability density in the grand-canonical ensemble (Eq. 3.6), and P is the probability to swap configurations. Our choice of P that satisfies detailed balance is:

$$P_{[(\beta_l,\mu_m,\boldsymbol{R}_i)(\beta_k,\mu_o,\boldsymbol{R}_j)\rightarrow(\beta_l,\mu_m,\boldsymbol{R}_j)(\beta_k,\mu_o,\boldsymbol{R}_i)]} =$$
$$\min\left[1,\left(\frac{\beta_l}{\beta_k}\right)^{\frac{3}{2}(N_{l,m}-N_{k,o})} \times e^{[-(\beta_l-\beta_k)(E(\boldsymbol{R}_j)-E(\boldsymbol{R}_i))+(\beta_l\mu_m-\beta_k\mu_o)(N_{l.m}-N_{k,o})]}\right] \tag{5.3}$$

5.2. Two-Dimensional Swap Scheme

A similar swap-acceptance probability has been proposed in Refs. 27 and 28, but we include a factor $\left(\frac{\beta_l}{\beta_k}\right)^{\frac{3}{2}(N_{l,m}-N_{k,o})}$ that is neglected in those papers. Furthermore, our scheme adopts a two-dimensional grid of values of temperatures and chemical potentials, while in Refs. 27 and 28 the values of T and μ are constrained to be along a phase boundary of the studied system (vapor-fluid coexistence for the LJ system), therefore being a invariate scheme, i.e., one-dimensional in practice. It is clear from Eq. 5.3

Figure 5.1.: The 2D schematic of Replica-Exchange Grand-Canonical method.

that swap trial moves are more likely to be accepted the larger the overlap between the energy distributions of the two replicas. A large overlap of energy distribution is verified if the values of the thermodynamic variables (μ, T) defining the two replicas are not too dissimilar. In traditional one-dimensional RE, swap moves are attempted only between neighbor replicas. In that case, each replica has two neighbors (or one, for the largest and smallest values of the chosen replicated thermodynamic variable, typically T). In our two-dimensional scheme (Fig. 5.1), each replica has between 3 and 8 neighbors, thus

enhancing the possibility for configurations to "diffuse" across replicas. We adopted a "collective" scheme for the attempted swaps that involves the definition of four different types of neighboring swaps, as illustrated in Fig. 5.1. At each RE move, one type of swaps is selected at random (each with probability 1/4). This choice has the advantage to involve all replicas (when the number of T-replicas and μ-replicas is even) in one attempted swap. An alternative scheme could be to select randomly one replica and independently one neighbor to perform the attempted swap, then to repeat until no replica has an unselected neighbor. This scheme is easily implemented and general for higher-dimensional settings (e.g., T and more than one μ for more than one type of particles that are exchanged with the reservoir).

The selection of T and μ range is of great importance and system-dependent. For instance, the lowest μ is selected to be slightly lower than the adsorption energy of the studied surface to make sure that the adsorption of at least one atom/molecule occurs. The highest μ is close to the condensation line of the gas phase. As explained in Ref. [19], the gas is in equilibrium with its droplets on the condition of $\Delta\mu = \mu - E^{\mathrm{DFT}} - E^{\mathrm{ZPE}} = 0$. This means that μ is chosen to be close to $E^{\mathrm{DFT}} + E^{\mathrm{ZPE}}$ to touch the condensation line, where E^{DFT} and E^{ZPE} are the DFT energy and the zero-point energy of the gas molecule, respectively. The choice of T is according to the experimental settings or catalytic reaction conditions. The T and μ intervals require individual GC MC/MD pre-tests in (T, μ) and $(T + \Delta T, \mu + \Delta\mu)$ states so that there is overlap between the energy distributions in (T, μ) and $(T + \Delta T, \mu + \Delta\mu)$ states, thus, the RE works.

6. Displacement of Atoms

At each cycle of our REGC scheme, after the RE or GC move has been performed, the atoms in each replica perform a sampling of the canonical (fixed N, fixed V, fixed T) ensemble. This is achieved with the standard Metropolis MC or with MD. This chapter describes these two techniques (MC and MD) to treat the movement of the nuclei on the potential-energy surface (PES). The method to characterize the PES will be described in chapter. 7.

6.1. Metropolis Monte Carlo

The Metropolis method was introduced as Markov process where a random walk is constructed so that the probability of visiting a particular atomic configuration $\boldsymbol{R}^N$ is proportional to the Boltzmann factor $e^{-\beta E(\boldsymbol{R}^N)}$.

According to MC, one atom-displacement step requires to select at random one atom and assigning to it a random displacement, typically uniformly distribute in a cube or sphere of size comparable with the typical interatomic distances at equilibrium. The move is accepted with probability [46]:

$$P_{(\boldsymbol{R}\to\boldsymbol{R}+\Delta\boldsymbol{R})} = \min\left[1, e^{-\beta[E(\boldsymbol{R}+\Delta\boldsymbol{R},\boldsymbol{R}^{N-1})-E(\boldsymbol{R},\boldsymbol{R}^{N-1})]}\right] \tag{6.1}$$

where $\boldsymbol{R}$ is the position of the selected atom, and $\Delta\boldsymbol{R}$ is the random displacement. $[E(\boldsymbol{R}+\Delta\boldsymbol{R},\boldsymbol{R}^{N-1})-E(\boldsymbol{R},\boldsymbol{R}^{N-1})]$ is the potential-energy difference between the system with one atom displaced and all the other $N-1$ atoms kept in place, and the system before displacement. In one MC cycle, N times of the attempted displacement are performed, so that on average each atom is attempted to be displacement once.

6.2. Born-Oppenheimer Molecular Dynamics

Molecular Dynamics simulation is a technique for computing the equilibrium thermo-dynamic properties, and dynamical phenomena such as transport of a classical many-

body system at finite temperature. *Classical* means that the nuclear motion of the constituent particles obeys the laws of classical mechanics. In this work, we use *ab initio* molecular dynamics (AIMD) which combines finite temperature dynamics with forces obtained from electronic structure calculations performed 'on the fly' as the MD simulation proceeds. In the following of this section, we confine the discussion on the Born-Oppenheimer molecular dynamics. An alternative type of AIMD is known as Car-Parrinello molecular dynamics (CPMD). [77] In CPMD, the dynamics of electrons and nulei are coupled by adding an extra term (the electronic degrees of freedom) to the Hamiltonian/Langrangian of the system. We will not discuss the CPMD further, since it is not used in the thesis.

Due to large difference between the masses of atomic nulei and electron mass, the time scales of their respective motion are also much different. In the Born-Oppenheimer molecular dynamics, the static electronic-structure problem is straightforwardly solved in each molecular-dynamics step given the set of fixed nuclear positions at that instant of time. That is, the electronic-structure part is reduced to solving a time-independent Schrödinger equation, concurrently to propagating the nuclei according to classical mechanics. Accordingly, the Hamiltonian H for the nuclei is classically described as

$$H(\boldsymbol{p}, \boldsymbol{R}) \equiv H(\boldsymbol{p}_1, \cdots, \boldsymbol{p}_N, \boldsymbol{R}_1, \cdots, \boldsymbol{R}_N) = \sum_{I=1}^{N} \frac{\boldsymbol{p}_I^2}{2M_I} + V(\boldsymbol{R}_1, \cdots, \boldsymbol{R}_N) \qquad (6.2)$$

where $\boldsymbol{p}_1, \cdots, \boldsymbol{p}_N$ are the momenta of the particles and $V(\boldsymbol{R}_1, \cdots, \boldsymbol{R}_N)$ is the interparticle potential.

One of the most significant aspects of an MD calculation is the calculation of the forces. Forces are calculated by evaluating the negative gradient of the total energy with respect to the nuclear coordinates, as proved in Hellmann-Feynman theorem. [78, 79]

MD simulations are performed via a series of time steps (t_0, t_1, t_k, ...). At t_0, (i) the initial velocities are assigned according to the Maxwell-Boltzmann distribution at the desired temperature T, (ii) the forces on each atomic nucleus are evaluated, (iii) the new velocities and positions are computed for all nuclei. At each t_k ($k > 0$) time step, the (ii) and (iii) steps are repeat.

6.2.1. Integration of Equation of Motion

This section describes the techniques to solve the equation of motion. Since there is no analytical solution to the equation of motion, the fundamental idea of the numerical

integrator is the discretization of time. There are several algorithms designed to solve the equation of motion.

If the position of particle is $\boldsymbol{R}(t)$ at time t, the coordinate of a particle at an adjacent time can be represented by a Taylor expansion:

$$\boldsymbol{R}(t + \Delta t) = \boldsymbol{R}(t) + \boldsymbol{v}(t)\Delta t + \frac{\boldsymbol{F}(t)}{2M}\Delta t^2 + \frac{\Delta t^3}{3!}\dddot{\boldsymbol{R}}(t) + \mathscr{O}(\Delta t^4) \tag{6.3}$$

where Δt is the time step in the molecular dynamics simulation. The size of the time step is of significant importance for a reliable MD trajectory since it determines the accuracy of the integration. Too large time steps can lead to inaccuracies of the integration that the molecule falls apart after just a few MD steps while the small time steps cause too expensive computations. The time step adopted in this thesis is $\delta t = 1$ fs. Tests for the accuracy of this time step can be found in Appendix A.2.

One of the simplest numerical integration method is the *Euler Scheme* where the expansion is truncated after the second order. The error of Euler integrator is $\mathscr{O}(t^3)$, the least accurate. Therefore, It is crucial to select a integration algorithm resulting in a reliable MD trajectory. There are some well-known criteria to follow:

- Accuracy for large time steps Δt in a long time span
- The MD trajectory should be time-reversible
- Conservation of total energy
- Low memory and fast execution speed

The term "time-reversible" means that the trajectory gets back to the starting point after running forward and then backward by the same number of time steps.

The previous position of the particle is expanded,

$$\boldsymbol{R}(t - \Delta t) = \boldsymbol{R}(t) - \boldsymbol{v}(t)\Delta t + \frac{\boldsymbol{F}(t)}{2M}\Delta t^2 - \frac{\Delta t^3}{3!}\dddot{\boldsymbol{R}} + \mathscr{O}(\Delta t^4) \tag{6.4}$$

Summation of Eq. 6.3 and Eq. 6.4, results in the Verlet integration [80] step for the position:

$$\boldsymbol{R}(t + \Delta t) = 2\boldsymbol{R} - \boldsymbol{R}(t - \Delta t) + \frac{\boldsymbol{F}(t)}{M}\Delta t^2 + \mathscr{O}(t^4) \tag{6.5}$$

The estimation of the new position includes an error of order Δt^4. Notice that there is no need for knowing velocities when computing the new positions. But the velocities can be derived if needed by Eq. 6.3 subtracting Eq. 6.4:

$$\boldsymbol{v}(t) = \frac{\boldsymbol{R}(t + \Delta t) - \boldsymbol{R}(t - \Delta t)}{2\Delta t} + \mathscr{O}(t^2) \tag{6.6}$$

The velocities obtained by Verlet integrator is less accurate than the positions, but it is accurate enough to conserve the kinetic energy with a proper choice of time step.

Verlet algorithm was first introduced by Loup Verlet in 1957 and offers greater stability than the Euler method. Generally, Verlet-like algorithm are regarded to be *symplectic* integrators, which indicates that the conservation of the volume element of the phase space and time-reversibility are included in these integrators. The merits of Verlet integrator are: the algorithm is straightforward, and needs only modest storage, and is time-reversible. However, it only reaches moderate precision, especially the precision of velocities are $\mathcal{O}(\Delta t^2)$. Furthermore, it needs initialization of $\boldsymbol{R}(t - \Delta t)$.

Another related, and more commonly used algorithm is Velocity Verlet algorithm, which requires no information of the position at $t - \Delta t$. In this integrator, the position is estimated same as that of Euler method, and the velocity is calculated by

$$\boldsymbol{v}(t + \Delta t) = \boldsymbol{v}(t) + \frac{\boldsymbol{F}(t) + \boldsymbol{F}(t + \Delta t)}{2} \Delta t + \mathcal{O}(t^2) \tag{6.7}$$

The error of the velocity Verlet integrator is of the same order as the original Verlet method. It requires the information of velocities at time t and forces at times t and $t + \Delta t$, So the Velocity algorithm is more memory consuming than the basic one.

Another very important criterion is to keep energy conservation. Typically, high-order algorithms tend to obtain good energy conservation for a few time steps, but have the energy drift for long times. Among those, Verlet and its related algorithm proved to have moderate energy conservation while little long-term drift. In this thesis, the velocity Verlet integrator is used.

6.2.2. Thermostats

During a MD simulation, the forces among atoms are calculated and the Newton equation is numerically integrated in order to obtain one displacement step for all atoms [46]. This scheme samples the constant energy E, constant V, constant N ensemble (micro-canonical). In order to sample the canonical ensemble, the velocities of the atoms need to be modified in order to obey the Maxwell-Boltzmann distribution at the desired T. Controlling the temperature and guaranteeing the quality of the generated trajectories are crucial issues in any molecular dynamics. This is achieved via numerical thermostats [46]. There are different schemes [81, 81–83] to perform Molecular Dynamics simulations at constant temperature.

In a canonical ensemble, the number of particles, the volume and the temperature are constant. Under the constant temperature condition, the absolute value of momenta follow the Maxwell-Boltzmann distribution:

$$P(p) = \left(\frac{\beta}{2\pi M}\right)^{3/2} e^{-\beta p^2/(2M)} \tag{6.8}$$

In recent years, another very popular thermostat was presented for canonical sampling by Bussi, Donadio and Parrinello. [84] and named as stochastic velocity-rescaling thermostat. In this algorithm, the velocities of all particles are rescaled by a properly constructed random force, in order to enforce correct canonical distribution of kinetic energy. Any deviation of the instantaneous kinetic energy $K(t)$ is corrected in the following way:

$$dK = \left[\bar{K} - K(t)\right]\frac{dt}{\tau} + 2\sqrt{\frac{K(t)\bar{K}}{N_{\mathrm{f}}\tau}}\xi(t) \tag{6.9}$$

where $\bar{K}$ is the target kinetic energy, the instantaneous kinetic energy is $K(t) = \frac{p^2(t)}{2m}$, τ is the relaxation time of the thermostat, N_{f} is the number of degrees of freedom of the system, and ξ is Wiener noise term obeying $\langle\xi(t)\xi(t') = \delta(t-t')\rangle$. In practice, velocities are updated by the velocity-verlet integrator. After the kinetic energy is evaluated, the velocities are rescaled by a factor α:

$$\begin{aligned}
\alpha^2 =& e^{-\Delta t/\tau} + \frac{\bar{K}}{N_{\mathrm{f}}K}\left(1 - e^{-\Delta t/\tau}\right)\left(W_1^2 + \sum_{i=2}^{N_f} W_i^2\right) \\
&+ 2e^{-\Delta t/2\tau}\sqrt{\frac{\bar{K}}{N_{\mathrm{f}}K}\left(1 - e^{-\Delta t/\tau}\right)}W_1
\end{aligned} \tag{6.10}$$

where W_i are random numbers generated based on Gaussian distribution with unitary variance. [85]

A quantity named pseudo-Hamiltonian $\tilde{H}(t)$ can be defined to be constant and plays a role similar to that of the energy in the microcanonical ensemble.

$$\tilde{H}(t) = H(t) - \int_0^t \left(\bar{K} - K(t')\right)\frac{dt'}{\tau} - 2\int_0^t \sqrt{\frac{K(t')\bar{K}}{N_f}\tau}\,\xi(t') \tag{6.11}$$

The conservation of $\tilde{H}$ provides a way to evaluate the accuracy of the integration. The physical meaning of Eq. 6.11 is that the fluxes of energy between the system and the thermostat are exactly balanced.

A relaxation time of the thermostat can be chosen such that the dynamic trajectories are not significantly affected. It does not have ergodicity problems and yields the correct canonical distribution of kinetic energy. The pseudo Hamiltonian is constant and can be used to verify how much the numerical procedure generates configurations that belong to the desired NVT ensemble and to provide a guideline for the choice of the integration time step. In this thesis, the stochastic velocity-rescaling thermostat is used together with velocity Verlet integrator to perform the molecular dynamicsin NVT ensemble, which has been already implemented in the FHI-aims [86]..

To sum up, in this chapter, the standard Metropolis MC moves and Born-Oppenheimer molecular dynamics simulation in NVT ensemble are described to treat the movement of the atom on the PES. The choice between the two schemes, MC or MD, for the canonical sampling step of our REGCMC or REGCMD algorithm is dictated only by convenience. In both case our choice is to perform few (about 20) MD steps or MC cycles between two applications of the REMC step, in order to take full advantage of the enhanced sampling allowed by the REGC accepted moves.

7. Potential-Energy Surface

A *potential-energy surface*(PES) is a mathematical function that gives the internal energy of a molecules as a function of its geometry. This chapter describes the methods characterizing the PES.

7.1. Force Field

Force Field (FF) is a mathematical expression with a set of parameters in this formula to calculate the interatomic potential energy as a function of atomic positions. The parameters are typically determined from *ab initio* quantum-mechanical calculation. One of the simplest interatomic potentials is the Lennard-Jones (LJ) potential [87]. The general form of the LJ potential is as follows:

$$E_{\text{LJ}} = \sum_{i \neq j} \left(4\epsilon_{ij} \left[\left(\frac{\sigma_{ij}}{r_{ij}} \right)^{12} - \left(\frac{\sigma_{ij}}{r_{ij}} \right)^6 \right] \right) \tag{7.1}$$

where r_{ij} is the interatomic distance between atoms i and j. The parameter σ_{ij} represents the interatomic distance where the LJ energy is zero while ϵ_{ij} represents the minimum interaction energy as show in Fig. 7.1. This potential only include the interactions between pairs of atoms and is thus named two-body potential. The two-body potential consists of an attractive term $(-4\epsilon_{ij}(\sigma_{ij}/r_{ij})^6)$ that describes the van der Waals polarization energy and a repulsive term $(4\epsilon_{ij}(\sigma_{ij}/r_{ij})^{12})$. Usually, the individual atomic parameters are given, while the parameters for each different pair of atoms are calculated by combine the individual ones. For instance, $\epsilon_{ij} = (\epsilon_i \epsilon_j)^{1/2}$ and $\sigma_{ij} = \frac{1}{2}(\sigma_i + \sigma_j)$.

The potential described in Eq. 7.1 is also referred to 12-6 LJ potential. In our first application, we just like to demonstrate the concept of REGC method is applied to two-species Lennard-Jones surfaces. The interactions in that system are described by this simple 12-6 LJ potential, and the details of parameters are listed in chapter. 10. Besides the simplest LJ potential, there are many other classical (non-reactive) force-field potentials. The functional form of classical force-field potential includes terms representing bond stretching, angle bending, rotation about dihedrals, improper dihedrals,
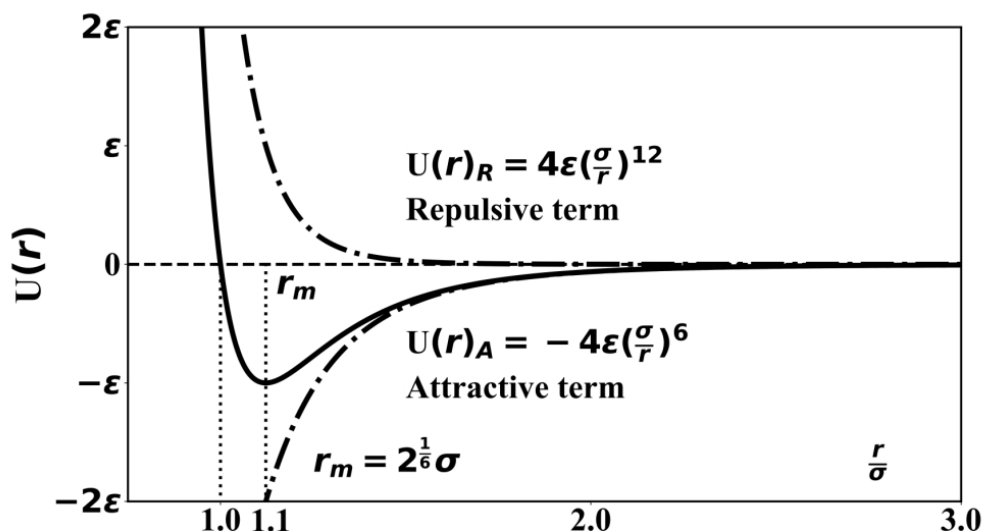
Figure 7.1.: 12-6 Lennard-Jones potential.

and non-bonded interactions. Bond stretching, angle bending, and improper dihedrals are all modeled by harmonic functions. However, such descriptions are inadequate for modelling chemical reactions as bonds break and form. ReaxFF is a reactive force field technique that uses the concept of bond order to model the interactions within a chemical system. [89–91] All other force-field potentials except LJ potential are not used in this thesis, so the relevant technique details are not discussed here.

7.2. Many-Body Problem

The dynamics of a time-independent scalar-relativistic system is governed by the time-independent Schrödinger equation

$$\hat{H}\Psi(\boldsymbol{r}, \boldsymbol{R}) = E\Psi(\boldsymbol{r}, \boldsymbol{R}) \tag{7.2}$$

where $\Psi(\boldsymbol{r}, \boldsymbol{R})$ is the many-body wavefunctions, E is the total energy of the system and $\hat{H}$ is the Hamiltonian of the system in atomic units.

$$\hat{H} = \hat{T}_{\text{nuc}} + \hat{T}_{\text{e}} + \hat{V}_{\text{nuc}-\text{e}} + \hat{V}_{\text{e}-\text{e}} + \hat{V}_{\text{nuc}-\text{nuc}} \tag{7.3}$$

where $\hat{T}_{\text{nuc}}$ and $\hat{T}_{\text{e}}$ are nuclei an electron kinetic operators, respectively.

$$\hat{T}_{\text{nuc}} = -\sum_{I}^{N_{\text{nuc}}} \frac{\hbar}{2M_I} \nabla_I^2 \tag{7.4}$$

34

$$\hat{T}_e = -\sum_{i}^{N_e} \frac{\hbar}{2m_e} \nabla_i^2 \tag{7.5}$$

$\hat{V}_{\text{nuc}-\text{nuc}}$ and $\hat{V}_{\text{e}-\text{e}}$ are nucleus-nucleus and electron-electron Coulomb interaction operators, respectively.

$$\hat{V}_{\text{nuc}-\text{nuc}} = \frac{1}{2} \sum_{I \neq J}^{N_{\text{nuc}}} \frac{Z_I Z_J e^2}{|\boldsymbol{R}_I - \boldsymbol{R}_J|} \tag{7.6}$$

$$\hat{V}_{\text{e}-\text{e}} = \frac{1}{2} \sum_{i \neq j}^{N_e} \frac{e^2}{|\boldsymbol{r}_i - \boldsymbol{r}_j|} \tag{7.7}$$

The nucleus-electron Coulomb interaction operator $\hat{V}_{nuc-nuc}$ is expressed:

$$\hat{V}_{\text{nuc}-\text{e}} = \sum_{i}^{N_e} \sum_{I}^{N_{\text{nuc}}} \frac{Z_I e^2}{|\boldsymbol{r}_i - \boldsymbol{R}_I|} \tag{7.8}$$

where N_{nuc} and N_{e} are the total number of nuclei and electrons in the simulated system, respectively. I and J are the indices of the nuclei, i, j are the indices of electrons, M_I and m_e are the masses of the nuclei and electrons, respectively. In total, there are $3N_{\text{nuc}} + 3N_{\text{e}}$ degrees of freedom since each electron or nucleus can move in x, y and z coordinates. There is no exact solutions of Eq. 7.2 except for a few number of systems, such as hydrogen atom, ionized hydrogen molecule and helium ion. In order to obtain a feasible solution of the many-body Hamiltonian, some approximations are needed to be introduced, as the Born-Oppenheimer approximation.

7.3. Born-Oppenheimer Approximation

Born-Oppenheimer (BO) approximation [92]allows us to decouple the nuclear and electronic degrees of motion; the nuclei are of order $\sim 10^3 - 10^5$ times more massive than the electrons, and therefore may be considered to be stationary on the electronic timescale. As a result of this, it is possible to neglect the nuclear kinetic energy contribution to the system energy. The "electronic" part of Hamiltonian $\hat{H}_{\text{e}}$ is

$$\hat{H}_{\text{e}} = \hat{T}_{\text{e}} + \hat{V}_{\text{nuc}-\text{e}} + \hat{V}_{\text{e}-\text{e}} \tag{7.9}$$

Considering $\Phi_l(\boldsymbol{r}; \boldsymbol{R})$ is to be the electronic eigenfunctions for $\hat{H}_{\text{e}}$, thereby, the nonrelativistic Schrödinger equation for the many-electron wavefunction $\Phi_l(\boldsymbol{r}; \boldsymbol{R})$,

$$\left\{ -\sum_{i}^{N_e} \frac{\hbar}{2m_e} \nabla_i^2 + \sum_{i}^{N_e} \sum_{I}^{N_{\text{nuc}}} \frac{Z_I e^2}{|\boldsymbol{r}_i - \boldsymbol{R}_I|} + \frac{1}{2} \sum_{i \neq j}^{N_e} \frac{e^2}{|\boldsymbol{r}_i - \boldsymbol{r}_j|} \right\} \Phi_l(\boldsymbol{r}; \boldsymbol{R}) = E_l^{\text{e}}(\boldsymbol{R}) \Phi_l(\boldsymbol{r}; \boldsymbol{R}) \tag{7.10}$$

The many-body wavefunction are then expressed by:

$$\Psi(\boldsymbol{r}, \boldsymbol{R}) = \sum_{l}^{L} \chi_l(\boldsymbol{R})\Phi_l(\boldsymbol{r}; \boldsymbol{R}) \tag{7.11}$$

As a consequence, the Schrödinger equation for nuclear dynamics is

$$\left[\hat{T}_{\text{nuc}} + \hat{V}_{\text{nuc}-\text{nuc}} + E_l^{\text{e}}(\boldsymbol{R})\right]\chi_l(\boldsymbol{R}) = E_l\chi_l(\boldsymbol{R}) \tag{7.12}$$

To investigate the validity of the BO approximation, left multiplication $\left\langle\Phi_{l'}(\boldsymbol{r}; \boldsymbol{R})\right|$ to Eq. 7.2, obtaining

$$\left[\left\langle\Phi_{l'}(\boldsymbol{r}; \boldsymbol{R})|\hat{T}_{\text{nuc}}|\Phi_l(\boldsymbol{r}; \boldsymbol{R})\right\rangle + V_{\text{nuc}-\text{nuc}} + E_l^{\text{e}}(\boldsymbol{R})\right]|\chi_l(\boldsymbol{R})\rangle = E_l|\chi_l(\boldsymbol{R})\rangle \tag{7.13}$$

based on the property

$$\left\langle\Phi_{l'}(\boldsymbol{r}; \boldsymbol{R})|\Phi_l(\boldsymbol{r}; \boldsymbol{R})\right\rangle = \delta_{ll'} \tag{7.14}$$

$$\left\langle\Phi_{l'}(\boldsymbol{r}; \boldsymbol{R})|\hat{T}_{\text{nuc}}|\Phi_l(\boldsymbol{r}; \boldsymbol{R})\right\rangle = -\sum_{l}^{L}\sum_{I}^{N_{\text{nuc}}}\frac{\hbar}{2M_I}\big[\nabla_I^2\chi_l(\boldsymbol{R})\delta_{ll'}+$$
$$2\Phi_{l'}^*(\boldsymbol{r}; \boldsymbol{R})\nabla_I\chi_l(\boldsymbol{R})\nabla_I\Phi_l(\boldsymbol{r}; \boldsymbol{R})+$$
$$\Phi_{l'}^*\chi_l(\boldsymbol{R})\nabla_I^2\Phi_l(\boldsymbol{r}; \boldsymbol{R})\big] \tag{7.15}$$

The first term in the Eq. 7.15 is the kinetic energy of nuclei T_{nuc}, and the last two terms are the interaction between two different electronic states caused by the nuclei motion, referred to *non-adiabatic* or *vibronic* interactions. According to BO approximation, these interactions are very small and commonly neglected. [92] Thus the E_l in Eq. 7.12 is termed as the $E_l^{\text{BO}}(\boldsymbol{R})$, the Born-Oppenheimer potential energy surface, corresponding to $V(\boldsymbol{R}_1, \cdots, \boldsymbol{R}_N)$ in Sec. 6.2

Although this equation is exact within the non-relativistic regime, it is not possible, except for trivially simple cases, to solve it. There are two reasons for this: one mole of a solid/gas/liquid contains $N > 10^{24}$ electrons; since the many-electron wavefunction contains $3N$ degrees of freedom, this is simply intractable; further, the electron-electron Coulomb interaction results in the electronic motions being correlated. Consequently the many-body wavefunction is a complicated mathematical object that incorporates the effects of this correlation, preventing a separation of the electronic degrees of freedom into N single-body problems. Further, the interaction is too strong to be treated as a perturbation. Thus we must search for approximations that render the Schrödinger equation tractable to numerical solution, whilst retaining as much of the key physics as is possible.

7.4. Hartree-Fock Method

Hartree-Fock theory is fundamental to much of electronic-structure theory. It was developed to solve *electronic Schrödinger equation* Eq. 7.10 which results from time-independent Schrödinger equation after involving Born-Oppenheimer approximation.

The exact eigenfunctions of the full electronic Hamiltonian are known only for one-electron systems, like hydrogen atom or He^+. Therefore, the basic idea of Hartree-Fock theory is from the simplest atom, hydrogen, to solve the Eq. 7.10. In Hartree approximation, if more than one electron are added to the system, electrons are assumed to not interact with each other, then the total electronic wavefunction would be the product of hydrogen atom eigenfunctions. Obviously, the assumption is pretty serious. Nonetheless, it provides a way to start with a general form of wavefunction

$$\Phi(\boldsymbol{r}_1, \boldsymbol{r}_2, \cdots, \boldsymbol{r}_{N_e}) = \phi_1(\boldsymbol{r}_1)\phi_2(\boldsymbol{r}_2)\cdots\phi_{N_e}(\boldsymbol{r}_{N_e}) \tag{7.16}$$

Which is known as *Hartree product.* [93] The Hartree method is fairly convenient and useful, but the major drawback is that it fails to satisfy the *Pauli exclusion principle* that two or more identical fermions cannot occupy the same quantum state simultaneously. In order to satisfy the criteria that the wavefunction is antisymmetry for fermions, the Slater determinant is proposed [94, 95]

$$\Phi = \frac{1}{\sqrt{N_e!}} \begin{vmatrix} \phi_1(\boldsymbol{r}_1) & \phi_2(\boldsymbol{r}_1) & \cdots & \phi_{N_e}(\boldsymbol{r}_1) \\ \phi_1(\boldsymbol{r}_2) & \phi_2(\boldsymbol{r}_2) & \cdots & \phi_{N_e}(\boldsymbol{r}_2) \\ \vdots & \vdots & \ddots & \vdots \\ \phi_1(\boldsymbol{r}_{N_e}) & \phi_2(\boldsymbol{r}_{N_e}) & \cdots & \phi_{N_e}(\boldsymbol{r}_{N_e}) \end{vmatrix} \tag{7.17}$$

As a consequence, the electrons in the Slater determinant functional form are all indistinguishable and each electron is associated with every orbital. It turns out that the assumption that the electrons can be described by an antisymmetrized product (Slater determinant) is equivalent to the assumption that each electron moves independently of all the others except that it feels the Coulomb repulsion due to the average positions of all electrons and it also experiences a "exchange" interaction due to antisymmetrization. Hence, Hatree-Fock theory is also referred to as an independent particle model or a mean field theory.

A determinant can be constructed and written in shorthand as $|ij \cdots k\rangle$ by a list of occupied orbitals $\{\phi_i(\boldsymbol{r}), \phi_j(\boldsymbol{r}), \cdots \phi_k(\boldsymbol{r})\}$. So the Hartree-Fock energy can be re-written

as:

$$E_{\mathrm{HF}} = \sum_i \langle i|\hat{h}|i\rangle + \frac{1}{2}\sum_{i\neq j}\left[\langle ii|\hat{V}_{\mathrm{e-e}}|jj\rangle - \langle ij|\hat{V}_{\mathrm{e-e}}|ji\rangle\right] \tag{7.18}$$

Where $\hat{h}$ is the sum of electron kinetic operator and electron-nucleus interaction operator. $\frac{1}{2}\sum_{i\neq j}\langle ii|\hat{V}_{\mathrm{e-e}}|jj\rangle$ is named as Hartree energy E_{Hartree}, while $\frac{1}{2}\sum_{i\neq j}\langle ij|\hat{V}_{\mathrm{e-e}}|ji\rangle$ is labelled as HF exchange energy E_{x}. If $i = j$, the self-interaction of electrons is cancelled automatically from exchange term. While HF energy is variational and includes correct exchange energy, it has no explicit correlation of electron movement. Therefore, the correlation energy is defined as the difference between HF energy and the exact energy calculated from true wavefunction. The correlation energy are included by improving the many-particle wave function, known as configuration interaction (CI). [96] In principle, it provides the exact wave function from which most properties can be calculated. However, the explosive increase in the number of configurations with increasing electron number limits the application of CI only to the systems with few electrons.

7.5. Density Functional Theory

Wave-function-based methods have been presented in the previous chapter. In this section, A different approach was taken to handle the many-electron problem to obtain the ground state of the system using electronic density instead of $3N_{\mathrm{e}}$ dimensional wave function. The prototype for modern density-functional theories is Thomas-Fermi (TF) scheme [97, 98]. Till 1964, Hohenberg and Kohn gave a mathematically rigorous demonstration that the ground-state properties can be the functional of the electronic distribution $n(\boldsymbol{r})$. [99]

• **Theorem I** The external potential $V_{\mathrm{ext}}(\boldsymbol{r})$ acting on any system of interacting particles is uniquely determined by the ground-state particle density $n_0(\boldsymbol{r})$

• **Theorem II** A *universal functional* for the energy $E[n]$ can be defined in terms of density $n(\boldsymbol{r})$: $E[n] = F[n] + V_{\mathrm{ext}}$ where $F[n] = T[n] + E_{\mathrm{e-e}}[n]$. The exact ground-state density minimize the functional $E[n]$ to get the exact ground-state energy.

Notice that $E[n]$ and $F[n]$ are the functionals of electron density n. These assertions are so encompassing and the following proofs are simple enough and included most textbooks (e.g., ref [100]) Another instructive definition of a functional was give by Levy [101, 102]and Lieb [103]. While these theorem are rigorously proved, they provide no practical way to how to calculate the densities or how to build the functional forms.

7.5.1. The Kohn-Sham equations

The necessity of both Hohenberg-Kohn and Levy-Lieb theorems is that a functional of density need to be known. The exact kinetic functional of density, however, is unknown. The challenge of finding reasonable approximation to energy functionals is greatly simplified by a different scheme proposed by Kohn and Sham (1965). [104] There are two assumptions in Kohn-Sham *ansatz*:

1. The exact ground-state density of the many-body system can be represented by the ground-state density of an auxiliary system of non-interacting particles

2. The Hamiltonian of the auxiliary system consists of the non-interacting electron kinetic functional $T_s[n]$ and the effective *local* potential $V_{\text{eff}}(\boldsymbol{r})$

Where the effective potential $V_{\text{eff}}(\boldsymbol{r})$ is the summation of three terms: the Hartree energy $E_{\text{Hartree}}[n]$, the electron-nuclear energy (external field) and exchange-correlation energy $E_{\text{xc}}[n]$ where all many-body effects of exchange and correlation are grouped.

According to the first assumption, the ground state density n_0 of the interacting system is equal to the ground state density of the non-interacting system

$$n_0(\boldsymbol{r}) = n_{\text{KS}}(r) = \sum_{i=1}^{N_e} |\phi_i(\boldsymbol{r})|^2 \tag{7.19}$$

where $\phi_i(\boldsymbol{r})$ is single-electron wave functions (orbitals) The non-interacting kinetic energy T_s is given by

$$T_s = -\frac{1}{2} \sum_{i=1}^{N_e} \langle \phi_i | \nabla^2 | \phi_i \rangle \tag{7.20}$$

The Hartree energy is defined as a functional of electron density as

$$E_{\text{Hartree}}[n] = \frac{1}{2} \int d^3r d^3r' \frac{n(\boldsymbol{r})n(\boldsymbol{r}')}{|\boldsymbol{r} - \boldsymbol{r}'|} \tag{7.21}$$

As a consequence, in the Kohn-Sham scheme for the full interacting many-body problem, the ground state energy functional are in the following form

$$E_{\text{KS}} = T_s[n] + \int d^3r V_{\text{ext}}(\boldsymbol{r})n(\boldsymbol{r}) + E_{\text{Hartree}}[n] + E_{\text{xc}}[n] \tag{7.22}$$

Here V_{ext} is the external potential due to the nuclei or any other external fields. So V_{ext} and E_{Hartree} have the explicit functional form of electron density. The independent-particle kinetic energy T_s is also given clear functional of the orbitals. Therefore, the exchange-correlation energy is expressed as

$$E_{\text{xc}}[n] = \langle \hat{T}_{\text{e-e}} \rangle - T_s[n] + \langle \hat{V}_{\text{e-e}} \rangle - E_{\text{Hartree}}[n] \tag{7.23}$$

If the functional $E_{\text{xc}}[n]$ were known, the Kohn-Sham *ansatz* for independent particles can provide the exact ground state energy and density, also other ground state properties of the many-body interacting electron system. Unfortunately, there is no exact expression for $E_{\text{xc}}[n]$ but many approximate forms proposed, so that it is feasible for Kohn-Sham approach to calculating the ground state properties of many-body electron systems.

Minimization of the KS energy functional with respect to the density $n(\boldsymbol{r})$ or the effective potential V_{eff}. The variational equation is derived from variation of wavefunctions as follows:

$$\frac{\partial E_{\text{KS}}}{\partial \phi_i(\boldsymbol{r})} = \frac{\partial T_{\text{s}}}{\partial \phi_i(\boldsymbol{r})} + \left[\frac{\partial E_{\text{ext}}}{\partial n(\boldsymbol{r})} + \frac{\partial E_{\text{Hartree}}}{\partial n(\boldsymbol{r})} + \frac{\partial E_{\text{xc}}}{\partial n(\boldsymbol{r})} \right] \frac{\partial n(\boldsymbol{r})}{\partial \phi_i(\boldsymbol{r})} = 0 \qquad (7.24)$$

subject to the orthogonalization constraints

$$\langle \phi_i | \phi_j \rangle = \delta_{ij} \qquad (7.25)$$

The non-interacting kinetic energy varied with respect to single-particle orbital given by

$$\frac{\partial T_{\text{s}}}{\partial \phi_i^*(\boldsymbol{r})} = -\frac{1}{2} \nabla \phi_i(\boldsymbol{r}); \frac{\partial n(\boldsymbol{r})}{\partial \phi_i^*(\boldsymbol{r})} = \phi_i(\boldsymbol{r}) \qquad (7.26)$$

The variation of the Lagrange function results in the KS eigenvalue equations

$$\left(H_{\text{KS}} - \epsilon_i \right) \phi_i(\boldsymbol{r}) = 0 \qquad (7.27)$$

where the ϵ_i are the eigenvalues, and H_{KS} is the effective Hamiltonian in KS scheme.

$$H_{\text{KS}} = -\frac{1}{2} \nabla^2 + V_{\text{KS}}(\boldsymbol{r}) \qquad (7.28)$$

with

$$\begin{aligned} V_{\text{KS}}(\boldsymbol{r}) &= V_{\text{ext}}(\boldsymbol{r}) + \frac{\partial E_{\text{Hartree}}}{\partial n(\boldsymbol{r})} + \frac{\partial E_{\text{xc}}}{\partial n(\boldsymbol{r})} \\ &= V_{\text{ext}}(\boldsymbol{r}) + V_{\text{Hartree}}(\boldsymbol{r}) + V_{\text{xc}}(\boldsymbol{r}) \end{aligned} \qquad (7.29)$$

Equations (7.24)-(7.29) are the well-known Kohn-Sham equations. Notice that during the derivation of these equations, there is no any approximation to the functional $E_{\text{xc}}[n(\boldsymbol{r})]$, which implies that KS equations works with any form of exchange-correlation functional and its accuracy relies on how exact the approximation of functional $E_{\text{xc}}[n(\boldsymbol{r})]$ is.

Given the explicit form of exchange-correlation functional, the Schrödinger-like independent-particle equations could be solved self-consistently. Generally, initial guess of electron density is given to calculate the effective KS potential in Eq. 7.29. With the Lagrange multipliers, KS eigenvalue equations Eq. 7.28 could be solved for the eigenfunctions $\phi_i(\boldsymbol{r})$, then the electron density is updated based on Eq. 7.19 with the eigenfunctions. This procedure is iterative until the convergence is reached, that is, the calculated total energy is closely approaching its minimum.

7.6. Exchange-Correlation Functional

Due to its success of practical, approximate functionals, density-functional theory become the most widely used method today for calculating electronic structure. The crucial term in the Kohn-Sham method is the exchange-correlation energy in the functional of density $E_{\mathrm{xc}}[n(\boldsymbol{r})]$. This part is devoted to discuss some approximations to the exact xc functional used in this thesis including PBE [105], PBE0 [106] and HSE [107, 108] functionals, and van der Waals correction proposed by Tkatchenko and Scheffler [109].

The most important approximations for $E_{\mathrm{xc}}[n(\boldsymbol{r})]$ have a quasilocal form. This form is

$$E_{\mathrm{xc}}[n(\boldsymbol{r})] = \int d\boldsymbol{r} n(\boldsymbol{r}) \epsilon_{\mathrm{xc}}([n(\tilde{\boldsymbol{r}})], \boldsymbol{r}) \tag{7.30}$$

where $\epsilon_{\mathrm{xc}}([n(\tilde{\boldsymbol{r}})], \boldsymbol{r})$ is an exchange-correlation energy per electron at point $\boldsymbol{r}$ that depends primarily upon the density $n(\tilde{\boldsymbol{r}})$ in at point $\tilde{\boldsymbol{r}}$ in the neighborhood of $\boldsymbol{r}$. The term "neighborhood" is a microscopic distance such as the local Germi wavelength $\lambda_{\mathrm{F}} \equiv \left[3\pi^2 n(\boldsymbol{r})\right]^{-1/3}$ or TF screening length. Notice that the xc energy density ϵ_{xc} is not uniquely defined by Eq. 7.30, this definition is motivated by the analysis of exchange-correlation hole. [110–112]

The exchange-correlation potential $V_{\mathrm{xc}}(\boldsymbol{r})$ as the third term in Eq: 7.29 is the functional derivative of E_{xc}. Together with Eq: 7.30, $V_{\mathrm{xc}}(\boldsymbol{r})$ can be written as

$$V_{\mathrm{xc}}(\boldsymbol{r}) = \epsilon_{\mathrm{xc}}([n(\tilde{\boldsymbol{r}})], \boldsymbol{r}) + n(\boldsymbol{r}) \frac{\partial \epsilon_{\mathrm{xc}}([n(\tilde{\boldsymbol{r}})], \boldsymbol{r})}{\partial n(\boldsymbol{r})} \tag{7.31}$$

The second term is called response potential [113] because it indicates the changes of the exchange hole with the change of density. In an insulator, the nature of electronic states changes discontinuously as a function of electron density n at a band gap, thereby this derivative is discontinuous at a band gap. This is named as "derivative discontinuity"

41

since adding a single electron leads to that the Kohn-Sham potential for all the electrons in a crystal shift by a constant. [114,115] None of these properties is incorporated in any simple xc functionals such as local density or gradient approximations.

7.6.1. Local-Density Approximation

It is already pointed out in the seminal paper by Kohn and Sham [104] that solids can be approximated as close to the limit of the homogeneous electron gas (HEG). In the HEG limit, the nature of the electron exchange and correlation have local characteristic. Thereby, the simplest and remarkable practical approximation for $E_{\mathrm{xc}}[n(\boldsymbol{r})]$, the so-called local-density approximation (LDA), is proposed

$$E_{\mathrm{xc}}^{\mathrm{LDA}}[n(\boldsymbol{r})] = \int d\boldsymbol{r}\, n(\boldsymbol{r})\epsilon_{\mathrm{xc}}(n(\boldsymbol{r})) = \int d\boldsymbol{r}\left[\epsilon_{\mathrm{x}} n(\boldsymbol{r}) + \epsilon_{\mathrm{c}} n(\boldsymbol{r})\right] \tag{7.32}$$

where $\epsilon_{\mathrm{xc}}(n(\boldsymbol{r}))$ is an exchange-correlation energy per particle of a *uniform* electron gas of density n. The exchange part is give by

$$\epsilon_{\mathrm{x}}(n) = -\frac{0.458}{r_s} \tag{7.33}$$

where r_s is the radius of a sphere containing one electron and given by $4\pi/3 r_s^3 = n^{-1}$. The correlation part is estimated by Wigner [116],

$$\epsilon_{\mathrm{c}}(n) = -\frac{0.44}{r_s + 7.8} \tag{7.34}$$

Despite of its simplicity, the LDA is exact for densities varying slowly on the scale of the local Fermi wavelength, and even provide comparable accuracy with HF for atoms and molecules, but less computational demanding. The error of the exchange part is typically within 10%, while normally overestimating the correlation energy by about a factor of 2. These two errors can be cancelled partially. On the one hand, LDA provides the ionization energies of atoms, dissociation energies of molecules and cohesive energies with a fair accuracy of $10-20\%$. On the other hand, the bond length is underestimated, leading to overestimation of bond strength. [117,118]

7.6.2. Generalized gradient approximations

To remedy the shortcomings of LDA, the gradients term of the density is proposed to include in the exchange-correlation potential via Taylor expansion (gradient expansion approximation) for the system where the density varies rapidly. However, the gradient

expansion approximation does not consistently improve over the LDA due to: 1) it violates the sum rules [119]; 2) Unphysical effects would be caused when only using Taylor expansion for the system where the density varies too rapidly, e.g., the correlation energies may become positive. [120] The basic problem is that in the real materials, the gradients are too large to break the expansion down.

The term *generalized*-gradient approximation (GGA) denotes there are a group of ways proposed to improve the large gradients behavior in order to preserve the desired properties. A general form is defined as

$$E_{\mathrm{xc}}^{\mathrm{GGA}}[n(\boldsymbol{r})] = \int d\boldsymbol{r} n(\boldsymbol{r}) \epsilon_{\mathrm{xc}}(n(\boldsymbol{r}), |\Delta n(\boldsymbol{r}|)$$
$$\equiv \int d\boldsymbol{r} n(\boldsymbol{r}) \epsilon_{\mathrm{x}}^{\mathrm{HEG}}(n(\boldsymbol{r})) F_{\mathrm{xc}}(n(\boldsymbol{r}), |\Delta n(\boldsymbol{r}|, \cdots,) \tag{7.35}$$

where $\epsilon_{\mathrm{x}}^{\mathrm{HEG}}$ is exchange energy of homogeneous electronic gas given in Eq. 7.33, while F_{xc} is dimensionless term including gradient of density. For this enhanced factor, there are three widely used forms proposed by Becke (B88) [121], Perdew and Wang (PW91) [122], and Perdew, Burke, and Enzerhof (PBE) [105]. PBE is non-empirical functional and does not rely on any experimental data.

GGA improves on LDA for atomization energies and cohesive energy, and describes well lattice constants, with 3 times computational cost. Especially for covalent bonds and weakly bonded systems many GGAs are far superior to LDA. However, GGA suffers the similar limitations with LDA since they are all semi-local XC functionals. The most well-known drawback of the semi-local XC functionals (LDA and GGA) is the discontinuity at the band gap for the insulator. The GGA-PBE is used throughout the Replica-Exchange Grand-Canonical molecular dynamics simulations in this work. The benchmark can be found in Appendix A.2.

7.6.3. Hybrid density functionals

The starting point of hybrid density functionals was proposed by Becke. [123] The idea behind it is to include a fraction of exchange energy in Hartree-Fock and mix the exchange (and the correlation) of a semi-local functional. Notice that the HF exact exchange energy is calculated using single-particle orbitals ϕ_i different from the HF ones (a slater determinant).

In the original idea of Becke, 50% of exact exchange energy was mixed with an equal 50% of XC contribution from LDA. Let's name it as half-and-half theory. [123]

The half-and-half theory is defective in several respects. The uniform electron-gas limit is not obtained, a disturbing failure from a formal density-functional perspective. Also, the semiempirical generalization gives good atomization energies only, while ionization potentials and proton affinities are extremely poor.

Accordingly, there were various schemes pointed out to refine the half-and-half one. One of the most popular way in quantum chemistry community is the B3LYP [124]. The B3LYP functional has a very broad use in chemistry community since it successfully predicts the atomization energies of molecules. Despite its great success, the B3LYP functional has its own shortcoming in several aspects. First of all, its accuracy is attributed to the cancellation of systematical errors. Besides, its computational cost limits its application to the extended systems.

One of the most popular non-empirical global hybrid GGA is PBE0 [125] (with pre-defined 25% exact exchange), which has the following form:

$$E_{\mathrm{xc}}^{\mathrm{PBE0}}[n] = 0.25 E_{\mathrm{x}}^{\mathrm{exact}} + 0.75 E_{\mathrm{x}}^{\mathrm{PBE}} + E_{\mathrm{c}}^{\mathrm{PBE}} \tag{7.36}$$

A screened Coulomb potential is introduced only to the exchange interaction in order to screen the long-range part of the HF exchange. [107,108] Thereby, the Coulomb operator are separated into short-range (SR) and long-range (LR) components in the form of:

$$\frac{1}{r} = \frac{\mathrm{erfc}(\omega r)}{r} + \frac{\mathrm{erf}(\omega r)}{r} \tag{7.37}$$

The first term is the SR term while the second is the LR component. ω is an adjustable parameter and $\mathrm{erfc}(\omega r) = 1 - \mathrm{erf}(\omega r)$. Therefore the pure exchange terms of PBE0 Eq. 7.36 can be re-expressed as follows:

$$E_{\mathrm{x}}^{\mathrm{PBE0}}[n] = \alpha E_{\mathrm{x}}^{\mathrm{exact,SR}}(\omega) + \alpha E_{\mathrm{x}}^{\mathrm{exact,LR}}(\omega) + (1-\alpha) E_{\mathrm{x}}^{\mathrm{PBE,SR}}(\omega) + E_{\mathrm{x}}^{\mathrm{PBE,LR}}(\omega) - (1-\alpha) E_{\mathrm{x}}^{\mathrm{PBE,SR}}(\omega) \tag{7.38}$$

Numerical tests indicate the contribution of long-range HF and PBE exchange part is rather small to the xc funcational compared to others and they tend to cancel out. Therefore, the long range exchange part is neglected , then getting a screened Coulomb potential hybrid density functional of the form:

$$E_{\mathrm{x}}^{\mathrm{HSE}}[n] = \alpha E_{\mathrm{x}}^{\mathrm{exact,SR}}(\omega) + (1-\alpha) E_{\mathrm{x}}^{\mathrm{PBE,SR}}(\omega) + E_{\mathrm{x}}^{\mathrm{PBE,LR}}(\omega) + E_{\mathrm{c}}^{\mathrm{PBE}} \tag{7.39}$$

Compared to PBE, PBE0 and HSE significantly improve the description of band gap for insulators and semiconductors. Therefore, the HSE functionals is used to calculate the HOMO-LUMO gap silicon surfaces in chapter 12.

7.6.4. Van der Waals corrections in density-functional theory

Density-functional theory has developed into the most successful and wide-spread approach for accurately predicting various physical properties of a wide range of materials systems. Despite its great success, there are situations where the approximation forms (LDA/GGA/hybrid) of the xc functionals failed. For instance, these local/semi-local xc functionals suffer from the inability when describing the long-range electron correlations, also known as electron dispersion. The electron dispersion can be regarded as an attractive interaction originating from the response of electrons in one region to instantaneous charge density fluctuations in another. The leading term of such an interaction is instantaneous dipole-induced dipole which gives rise to the well known $-\frac{1}{R^6}$ decay of the interaction energy with interatomic separation R. Standard XC functionals do not describe dispersion due to: (a)instantaneous density fluctuations are neglected; and (b) only local properties are accounted for to calculate the XC energy.

The electron dispersion is also referred to as van der Waals (vdW) forces since it was first introduced in J. D. van der Waals doctoral thesis "on the continuity of the gaseous and liquid state". [126]. In the terminology of chemistry the term vdW includes the following forces between molecules: (i) two permanent dipoles (Keesom force), (ii) a permanent dipole and a corresponding induced dipole (Debye force), and (iii) two instantaneously induced dipoles (London dispersion force). [127–129]

Many DFT-based dispersion techniques have been developed. The basic requirement for any DFT-based dispersion scheme should be that it yields reasonable $-1/R^6$ asymptotic behavior for the interaction of particles in the gas phase, where R is the distance between the particles. Therefore, a simplest approach is to add an long-range attractive energy term to the total energy of DFT E_{DFT} like

$$E_{\mathrm{tot}} = E_{\mathrm{DFT}} + E_{\mathrm{disp}} \tag{7.40}$$

where the long-range dispersion is then calculated by

$$E_{\mathrm{disp}} = -\sum C_6^{\mathrm{AB}}/R_{\mathrm{AB}}^6 \tag{7.41}$$

The dispersion here is calculated by summing over all pairs of atom A and B and therefore is assumed to be pairwise additive. The dispersion coefficients C_6^{AB} depend on the elemental pair A and B, and are independent of direction (isotropic) and constants.

The vdw correction used in this thesis is proposed by A. Tkatchenko and M. Scheffler (TS-vdw) in 2009. [109] The dispersion energy calculated in TS corrections shares the

same expression in Eq. **??**, but relies on reference atomic polarizabilities and reference atomic C_6 coefficients.

$$f_{\text{damp}}(R_{\text{AB}}, R_A^0, R_B^0) = \frac{1}{1 + e^{\left[-d\left(\frac{R_{\text{AB}}}{s_R R_{\text{AB}}^0} - 1\right)\right]}} \tag{7.42}$$

where $R_{\text{AB}}^0 = R_A^0 + R_B^0$, d and s_R are free parameters.

The *effective volume* is defined to take the environment dependence into C_6 term account expressed as

$$C_{6\text{AA}}^{\text{eff}} = \left(\frac{V_A^{\text{eff}}}{V_A^{\text{free}}}\right)C_{6\text{AA}}^{\text{free}} = \left(\frac{\int r^3 n^{\text{eff}}(\boldsymbol{r})d^3\boldsymbol{r}}{\int r^3 n^{\text{free}}(\boldsymbol{r})d^3\boldsymbol{r}}\right) \tag{7.43}$$

where $C_{6\text{AA}}^{\text{free}}$ are the coefficients of free atoms easily found in the Chu and Dalgarno database. [130] $n^{\text{free}}(\boldsymbol{r})$ is the density of the free atom. The effective density $n^{\text{eff}}(\boldsymbol{r})$ is calculated by Hirshfeld partition. [131] The accuracy of the TS-vdw correction is significantly high and only 5.5 % MAPD on the reference Meath et, al. data.

So far only pairwise additive vdW methods are discussed. To capture the contributions beyond the pairwise, the original TS-vdW method for molecules and solids is extended by self-consistently including long-range screening effects in the effective atomic polarizabilities. [132] The extended model is termed as TS-vdw+SCS. The detailed explanation of TS-vdw+SCS can be found in Reference [132].

8. Calculating Phase Diagrams

After a REGC simulation, we obtain $\Omega_{l,m}$ equilibrium samples from each of the $S = L \times M$ thermodynamic states (μ_m, V, T_l) within the grand-canonical ensemble. For each sample, a wide range of observable values can be collected, starting from the potential energy, the number of particles, and going to properties that are not related to the sampling rules. For instance, structural quantities like the radial distribution function or electronic properties such as the HOMO-LUMO gap of the system. In order to construct a phase diagram for the studied system, one has first to define which *phases* are of interest. For instance, we can define as one phase all samples with the same number of particles N. The task is then to evaluate the free energy $f_i(\mu, T)$ of phase i, as function of μ and T, and for each value of (μ, T) the most stable phase is the one with lowest free energy. From textbook statistical mechanics, the free energy is related to the probability p_i to find the sampled system in a certain phase (i.e., having a certain value of an observable quantity) as follows:

$$
\begin{aligned}
f_i(\mu, T) &= -k_B T \ln p_i(\mu, T) \\
&= -k_B T \ln \frac{\int_\Gamma d\boldsymbol{R} \, \chi_i(\boldsymbol{R}) \, q(\boldsymbol{R}; \mu, \beta)}{\int_\Gamma d\boldsymbol{R} \, q(\boldsymbol{R}; \mu, \beta)}
\end{aligned}
\tag{8.1}
$$

where $\boldsymbol{R}$ denotes the configuration of the system, χ_i is the indicator function for the state i — e.g., equal to 1 when N is a given N^* and 0 otherwise —, and $q(\boldsymbol{R}; \mu, \beta)$ is the density function for the specific statistical ensemble. The integrals are over the whole configuration space Γ.

The normalization term at the denominator of Eq. 8.1 is known as the *partition function*, $c(\mu, \beta)$. Once $q(\boldsymbol{R}; \mu, \beta)$ is defined for the sampled ensemble (see further), the nontrivial task is to estimate $c(\mu, \beta)$, in order to evaluate the free energy and find its minimum.

To efficiently estimate the partition function from our REGC sampling, we adopted the multistate Bennett acceptance ratio (MBAR) [29] approach, as implemented in the pymbar code (<https://github.com/choderalab/pymbar>). The MBAR method starts

47

from defining the reduced potential function for the grand-canonical ensemble $U(\boldsymbol{R}; \mu, \beta)$ for state (μ, β) [29]:

$$U(\boldsymbol{R}; \mu, \beta) = \beta \Big[E(\boldsymbol{R}) - \mu N(\boldsymbol{R}) \Big] \tag{8.2}$$

where $N(\boldsymbol{R})$ is the number of particles for the considered configuration. We note that there is a sign mistake in front of μN for the corresponding formula in the original MBAR paper [133]. The grand-canonical density function is then $q(\boldsymbol{R}; \mu, \beta) = \exp[-U(\boldsymbol{R}; \mu, \beta)]$. The MBAR approach provides the lowest-variance estimator for $c(\mu, \beta)$, first by determining its value over the set of actually sampled states, via the set of coupled nonlinear equations [29]:

$$\hat{c}_{l,m} = \sum_{i=1}^{\Omega_{l,m}} \frac{q(\boldsymbol{R}_{i,l,m}; \mu_m, \beta_l)}{\sum_{l=1}^{L} \sum_{m=1}^{M} \Omega_{l,m} \hat{c}_{l,m}^{-1} q(\boldsymbol{R}_{i,l,m}; \mu_m, \beta_l)} \tag{8.3}$$

where the index i runs over all the samples in one state. Crucially, all samples enter the estimator for $\hat{c}_{l,m}$, at state (l, m), irrespective of the state they were sampled in. Once the set of equations for the $L \times M$ $\hat{c}_{l,m}$'s is solved, $c(\mu, \beta)$ can be estimated for any new state (μ, β) via the same formula, with the observation that the $\hat{c}_{l,m}$'s at the denominator are now known.

Next, Eq. 8.1 can be evaluated. Following the example where the phase i is identified by the number of particles in the system, the values of N that minimizes $f_i(\mu, \beta)$ is the stable phase at the particular value of (μ, β). Graphically, one can assign a color to each value of N and, for each (μ_i, β_j) on a grid, the color is assigned to a pixel of size $(\delta\mu, \delta\beta)$ centred at (μ_i, β_j) (see Fig. 10.1).

In order to obtain a more familiar (p, T) phase diagram from the evaluated (μ, β), we use the relationship $\mu(p, T) = k_B T \ln(p/p_0)$, where p_0 is chosen such that $-k_B T \ln(p_0)$ summarizes all the pressure-independent components of μ, i.e., translational, rotational, vibrational etc. degrees of freedom. [12, 17, 44]

We now turn our attention to evaluating the ensemble-averaged value of some property, at a given state point (μ, β). To give a concrete example for which we actually give results in section 10.3, let's consider the radial distribution function $g(r)$, i.e., the probability to find a particle at a given distance r from any selected particles, averaged over all particles and samples. Here, we are in particular interested in the average (or expected) value of a property like $g(r)$ when the system is in a given phase, e.g., has a certain number of particles N. The ensemble average value of $g(r)$ at a given r and

given state point (μ, β), and phase i is:

$$\langle g(r) \rangle_{\mu, \beta, i} = \frac{\int_\Gamma d\boldsymbol{R} \, \chi_i(\boldsymbol{R}) \, g(r; \boldsymbol{R}) \, q(\boldsymbol{R}; \mu, \beta)}{\int_\Gamma d\boldsymbol{R} \, q(\boldsymbol{R}; \mu, \beta)} \tag{8.4}$$

where the function $g(r; \boldsymbol{R})$ at any given r depends on the whole configuration $\boldsymbol{R}$. In the MBAR formalism, the integrals are estimated over the sampled points via:

$$\langle g(r) \rangle_{\mu, \beta, i} = \sum_{n=1}^{\Omega_i} \frac{g(r; \boldsymbol{R}_n) \, c_{\mu, \beta}^{-1} \, q(\boldsymbol{R}_n; \mu, \beta)}{\sum_{l, m} \Omega_{l, m, i} c_{\mu_m, \beta_l}^{-1} q(\boldsymbol{R}_{l, m, i}; \mu_m, \beta_l)} \tag{8.5}$$

where Ω_i is the number of samples in phase i and therefore the sum over n runs over all samples belonging to phase i. Similarly, $\Omega_{l, m, i}$ is the number of samples in phase i in each sampled state point (m, l). In practice, $g(r)$ is discretized into a histogram, in which bin k counts how many particles are found between distance r_{k-1} and r_k (see section 10.3 for more details). One should note that the average value of each bin in the histogram is evaluated independently by MBAR.

9. Implementation

Due to the inherently parallel nature of replica exchange, the REGC method is well suitable for a massively parallel implementation on supercomputers. MD or MC simulation of each replica at different T are performed simultaneously and independently for a given number of MD time steps or MC moves. The required computational resources are proportional to the number of replicas S, e.g., if each replica requires q cores, in total, $S \times q$ cores are assigned to this REGC simulation. In practice, The memory requirements are fully given by the chosen MD/MC engine and the parallel scalability of REGC method mainly depends on the underlying MD/MC engine. The REGC method has been incorporated in the FHI-PANDA code (https://gitlab.com/zhouyuanyuan/fhi-panda), which is distributed under the MIT License. The FHI-panda code is python package and is distributed in source code form.

```
############### The Basic Parameters of REGCMD ################
# Temerpature sequence in the simulation.
Temperature = 360 560 760 960
# 540 600 660 720
# Chemical potential sequence in the simulation
Mu = -1.0 -0.9 -0.8 -0.7
# Upper Wall for the adsorbed atoms
Uwall = 4
```

Figure 9.1.: Example input file **REGC.in** for Si(100) surface.

FHI-panda requires three input files: **REGC.in**, **control.in** and **geometry.in**. Notice that **control.in** and **geometry.in** are the required files in FHI-aims [86] to perform the MD simulation and MD engine can be extended to any MD package not only FHI-aims. Fig. 9.1, 9.2, and 9.3 show as examples the **regc.in**, **control.in** and **geometry.in** files for Si(100) surface. The philosophy of their separation is simple:

- **REGC.in** contains information directly related to the settings for a REGC calculation. This obviously includes temperature sequence, chemical-potential sequence. Another important parameter is **Uwall**: It defines a sphere for the cluster where the adsorbed atoms are confined. The center of this sphere is the center of mass for the cluster and the radius is **Uwall**. For the surface, this parameter defines a distance from the top layer of the surface to the vacuum. Together with the surface lattice vector, a

box is formed where the adsorbed atoms are confined.

- **control.in** contains all other MD-run-specific information. Typically, this file depends on which code is chosen to perform the MD calculation. It is in the format of **INCAR** file for VASP.

- **geometry.in** contains the initial structure (atomic positions and species) for each replica. All replicas can share the same initial structure or different replicas can have different initial structures. It is in the format of **POSCAR** file for VASP.

```
xc  pbe
vdw_correction_hirshfeld
output hirshfeld
charge 0.0
spin none
relativistic atomic_zora scalar
use_dipole_correction
######SCF Accuracy###################
n_max_pulay      10
charge_mix_param  0.2
occupation_type gaussian 0.1
sc_accuracy_eev 1E-4
sc_accuracy_etot 1E-4
sc_accuracy_rho 1E-5
sc_iter_limit 1000
sc_accuracy_forces 1E-4
###EIGENVALUE SOVALTION#########
k_grid  4 4 1
###MD########################
MD_run    0.02 NVT_parrinello $T_Target$ 0.02
MD_time_step                 0.001
MD_restart                   .false.
output_level MD_light
MD_thermostat_units cm^-1
MD_maxsteps -1
postprocess_anyway .true.
##########################################################################
#
# FHI-aims code project
# VB, Fritz-Haber Institut, 2009
#
# Suggested "light" defaults for Si atom (to be pasted into control.in file)
# Be sure to double-check any results obtained with these settings for post-processing,
# e.g., with the "tight" defaults and larger basis sets.
#
##########################################################################
species        Si
```

Figure 9.2.: Example input file **control.in** for Si(100) surface. FHI-aims is used to perform MD calculations.

The REGC algorithm itself is embarrassingly parallel. However, inherently parallel nature of RE is challenged when the the computational-time cost for MD/MC simulation of different replicas varies a lot due to the different system sizes. The slowest replica makes all the other replicas wait, that is, all the other jobs are idling and waiting for the slowest one to finish, leading to loading unbalance. A simple and effective solution is to partition a REGC simulation involving a large number of replicas into several REGC calculations. Notice that the computation cost will not increase because of the partition. For instance, a REGCMD simulation is performed as benchmark for Si(100) system in a H_2 gas phase with 64 replicas. This was performed on 10 240 cores (256 nodes $\times$ 40 cores) and 4 nodes are allocated for the MD run of each replica. In total, there are

2 000 REGC steps performed for each replica. In each REGC step, 20 MD time steps (each is 1 fs) have been calculated. Therefore, 20 000 MD time steps (40 ps) have been performed for each replica. The ratio C is defined as

$$C = \frac{t_{\text{totalMD}}}{t_{\text{total}}} \tag{9.1}$$

where t_{totalMD} is total MD wall-clock time for each replica and t_{total} is computer time for this REGCMD simulation. The t_{total} is equal for all the 64 replicas due to the inherently parallel nature of REGC method. As shown in Fig. 9.4, C is around 0.82 for the quickest

```
lattice_vector      15.31876         0.00000         0.00000
lattice_vector       0.00000        15.31876         0.00000
lattice_vector       0.00000         0.00000       121.97400
      atom       3.61048         3.76291        40.76722      Si
      atom       7.48721         3.90726        40.81160      Si
      atom      -3.86810         3.82926        40.72837      Si
      atom       0.07297        -7.62687        40.86288      Si
      atom       3.75803         7.55604        41.02949      Si
      atom      -7.55796        -7.52169        41.10677      Si
      atom      -3.81030         7.63051        40.93392      Si
      atom      -0.07502        -3.77549        40.53570      Si
      atom       3.64360        -3.82375        40.65617      Si
      atom      -7.41398        -3.78388        40.53384      Si
      atom      -3.92054        -3.84561        40.92392      Si
      atom      -0.47228         2.08372        38.99632      Si
      atom       4.55376         2.00285        39.47984      Si
      atom       7.10019         1.78537        39.66821      Si
      atom      -3.17494         1.98201        39.27575      Si
      atom       0.62022         5.88138        39.54760      Si
      atom       3.06795         5.78004        39.56433      Si
      atom      -7.14170         5.93721        39.75051      Si
      atom      -4.53167         5.93344        39.47209      Si
      atom       0.41822        -5.73431        39.12856      Si
      atom       2.72225        -5.79752        40.29009      Si
      atom      -6.76469        -5.77301        39.40654      Si
```

Figure 9.3.: Example input file **geometry.in** for Si(100) surface. FHI-aims is used to perform MD calculations.
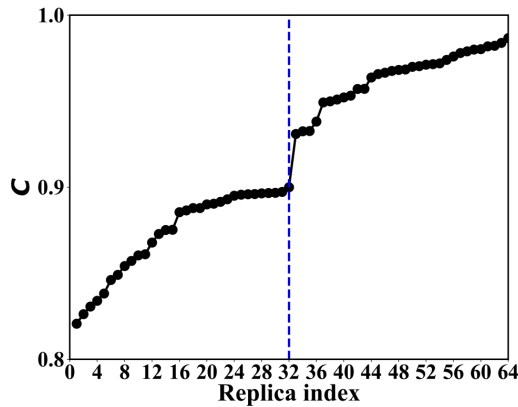
Figure 9.4.: The ratio of MD total wall time of each replica to the total computer time for each replica. Test made in Max-Planck-Gesellschaft (MPG) supercomputer COBRA. [134]
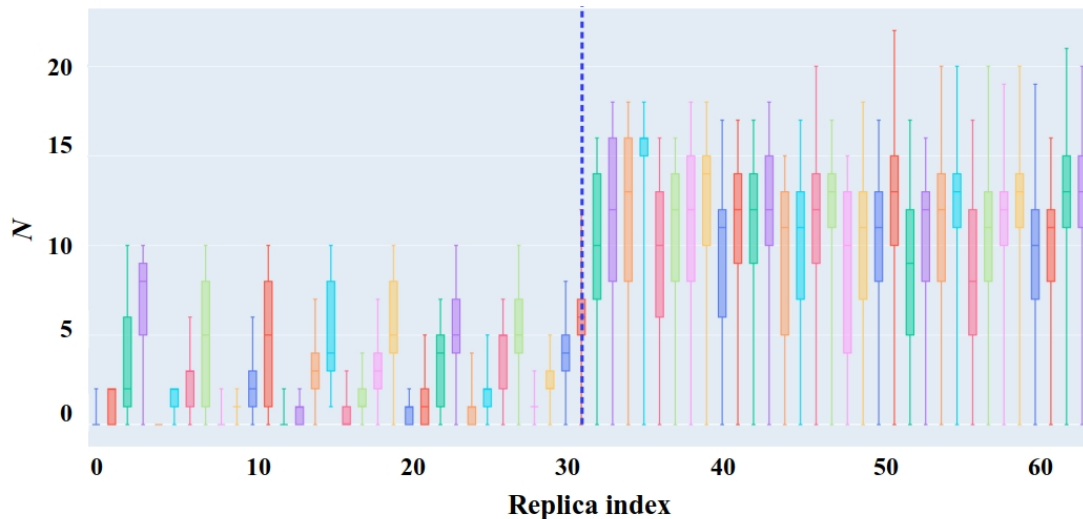
Figure 9.5.: The box-and-whisker plot of the number N of adsorbed H atoms in each replica.

replica while it is 0.98 for the slowest one. This means that for the 160 cores distributed for the quickest replica, the idle time is at most 0.16 to the total computer time. The idle time becomes less than 1/10 of the total computer time if the 64-replicas REGCMD simulation is divided into two 32-replicas REGCMD simulations as separated by the blue dash line in Fig. 9.4. All the MD simulations are performed in the electronic-structure code package FHI-aims [86]. The box-and-whisker plot of the number of adsorbed H atoms (N) is shown in Fig. 9.5. The box-and-whisker plot graphically depicts groups of data through their quartiles. In each box-and-whisker plot, the median Q_2 of the dataset is illustrated as a line inside the box while the first quartile Q_1 (25 %) and the third quartile Q_3 (75%) are the lower and upper boundary of the box. The upper whisker is the largest observed N in the range from Q_3 to $Q_3 + 1.5 \times (Q_3 - Q_1)$, while the lower whisker is the smallest observed N in the range from $Q_1 - 1.5 \times (Q_3 - Q_1)$ to Q_1. The box-and-whisker plots of N shows that the distribution of N in the first 32 replicas is much different from those in the last replicas.

In practice, the partitioning strategy is implemented by dividing the range of chemical potential into several non-overlapping intervals, while the whole range of tempera-

tures are kept in each partition. Though replica-exchange between neighbouring chemical potential values but belonging to different partitions can not attempt, it is not a problem as long as the distributions of sampled observables (primarily, the energy) overlap between partitions. In this way the MBAR post-processing takes care of properly normalizing the statistics.
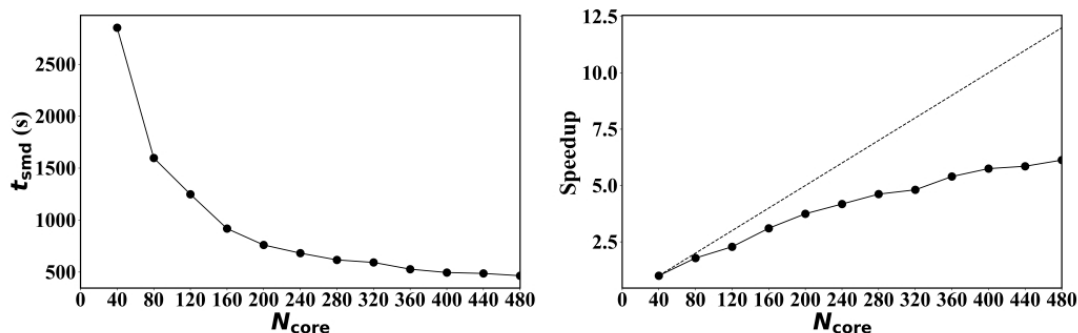
Figure 9.6.: Single molecular-dynamics t_{smd} (left panel) and speedup (right panel) as a function of the number of cores N_{core}. Test made in the HLRN-IV phase 1 in Göttingen System.

The scalability (SC) of a REGCMD calculation is the product of the scalability of REGC (SC_{regc}) and MD engine (SC_{md}) and the ratio (C) between the total MD wall-clock time and the computer time for the REGCMD simulation. Notice that for the ideal linear scaling, the SC should be equal to 1 independent of number of CPUs used. The REGC itself is linearly scaling, that is, $SC_{\text{regc}} = 1$. In Fig. 9.6, scaling test is shown for the computer time of a single MD calculation (t_{smd}) performed for every replica at each REGC step. It is seen that the speedup is close to ideal up to $N_{\text{core}} = 160$ cores, around 0.8 of the ideal speedup. Therefore,

$$SC = SC_{\text{regc}} \times SC_{\text{md}} \times C \tag{9.2}$$

Taking the above 32-replica REGCMD calcuation as example, the C is at least 0.84 and SC_{md} is around 0.8 when 160 cores are used for a single MD. Therefore, the scalability of this REGCMD simulation is around 0.67. This is not satisfactory and the improvement of scalability of REGC+MD engine is in progress.

In summary, the REGC approach by construction is embarrassingly parallel and requires little memory for particle exchange or replica exchange. In practice, after particle/replica exchange, MD/MC engine is required to diffuse the configuration in each

replica. Therefore, when coupled with MD/MC, in particular *ab initio* MD, the required memory for a REGCMD/MC simulation is fully given by the adopted MD/MC engine due to little memory required in REGC. The parallel scaling is also mainly given by the MD/MC engine since REGC is linearly scaling.

Part II.

Applications

10. Lennard-Jones Surface

In this chapter, the replica-exchange grand-canonical (REGC) approach is applied as a proof of concept to model system consisting of Lennard-Jones (LJ) particles adsorbing on the (111) surface of a fcc crystal, also modeled via LJ interactions. The purpose of this study is to demonstrate how an extensive REGC sampling of the system leads to the construction of the full T-p phase diagram as well as the *a posteriori* analysis of structural details of the identified (meta)stable phases.

The studies system consists of a fcc(111) frozen surface of species A which is in contact with a gas phase of species-B particles. The interaction between particles in the surface and gas phase was taken to be a 12-6 LJ potentials $E_{\mathrm{LJ}} = \sum_{i \neq j} 4\epsilon_{ij}[(\sigma_{ij}/r_{ij})^{12} - (\sigma_{ij}/r_{ij})^6]$. The parameters ϵ_{AB}, and ϵ_{BB} are 0.66 and 0.01 eV, respectively. The reason behind this choice is to have AB (attractive) interactions much stronger than BB interactions, in order to favor the adsorption of the B particles onto the A particles, as opposed to the formation of stable clusters of B clusters in the gas phase. The σ_{AA}, σ_{AB}, and σ_{BB} are 2.5, 1.91 and 1.2 Å. The length of the lattice vectors of this 2D hexagonal supercell is 11.489 Å. The equilibrium distances d_{ij}^{eql} are mismatched such that $d_{AB}^{\mathrm{eql}} > d_{BB}^{\mathrm{eql}}$, and both are shorter than the fixed AA first-neighbor distances. The LJ potential is truncated and shifted, such that the potential vanishes at the cutoff radius ($r_{ij}^c = 2.5\sigma_{ij}$). The sub-system labelled as A_{18} is a 2-layer slab with a 3×3 lateral supercell (i.e., 18 A atoms), periodically replicated in the x and y direction, while the z direction is aligned with the [111] direction of the slab. Here, the 3×3 lateral supercell is chosen as an example, in fact, any supercell size is possible to choose. The spacing between single layers is around 3.2 Å. Only 2-layer slab is selected since the spacing between the third layer and the first layer is around 6.4 Å, which is larger than the r_{AB}^c of 4.75 Å. Therefore, there is no interaction between the A particles in the third layer and B particles adsorbed in the vacuum. Notice that the 2-layer fcc(111) surface is equivalent to the 2-layer hcp(111) surface, therefore, the same results can be obtained for the hcp(111) with that for the fcc(111). The gas particle B is only allowed to adsorb (insert) in the "surface" zone. We defined the "surface" zone as a slab of height 48.0

Å above (i.e., in the positive z direction), starting from the z position of the topmost atoms of A_{18}. 48.0 Å is much larger than the thickness ($\sim$ 3 Å) of adsorbed multi-layer (before condensation). At the same time, particles B are inserted at all x and y coordinates, uniformly. Insertion and deletion attempts have been performed with equal probabilities. For every configuration, after each particle/replica exchange attempt, ten sequential MC moves are performed.

Figure 10.1.: Phase diagrams of a gas-phase (particles B) in contact with a frozen fcc(111) surface calculated via by MBAR from the REGCMC sampling (panel a) and aiAT (panel b) at (p_B, T) conditions corresponding to a range from zero adsorbed particles (region labeled as "pristine", referred to the surface) to the deposition of the B particles into a bulk solid. The red line is the melting line for the B particles, the sublimation line is blue, and the vaporization line is cyan. The cyan, green and pink stars correspond to the "corner" states for the REGCMC sampling: (650 K, −0.9 eV), (650 K, −2.4 eV) and (200 K, −0.9 eV), respectively. The fourth corner, (200 K, −2.4 eV) falls outside the (p_B, T) window shown in the plot. The blue circle indicates (600 K, 8.89×10^{-2} atm) and (200 K, 2.03×10^{-17} atm) is exactly the pink star, corresponding to two states in Fig. 10.4c and Fig. 10.4b, respectively.

In the calculations, 160 replicas are defined i.e., 10 temperatures ranging from 200 to 650 K, with an interval of 50 K, and 16 chemical potentials ranging from −2.4 to −0.9 eV, with an interval of 0.1 eV. This gives 160 parallel runs. The range of chemical potentials is selected such that the lowest value of μ is comparable to and slightly lower than the adsorption energy of one B particle on A_{18}, in order to assure that the sampling includes states where zero or few particles are adsorbed (in order to have the pristine surface appearing in the phase diagram). The highest value of μ is ideally always close to zero, in order to scan up to the condensation of B particles and formation of a bulk B phase. The range of temperature was chosen to be slightly lower than the solid/liquid/gas triple point of the B particles and ranging to few times (here, four) its critical temperature [135]. In practice, pre-knowledge of the studied system can be applied in order to frame a suitable (μ, T) window containing phases of interest. The spacing between T and μ values is more difficult to estimate *a priori*. The four "corner" states are (650 K, −0.9 eV), (650 K, −2.4 eV), (200 K, −0.9 eV) and (200 K, −2.4 eV)

on the 2D REGC schematic, that is, the choice of the highest temperature with the highest and lowest chemical potentials and the choice of the lowest temperature with the highest and lowest chemical potentials. During the simulation, one has to check that the acceptance ratio of RE attempted moves is not too low, in order to ensure a proper diffusion of replicas in the (μ, T) window. For instance, the present choice ensured an acceptance ratio of about 25%. Configuration swaps were attempted every 100 REGC steps, and x_0 was set equal to 0.99; a total of 1.2×10^5 REGC steps were performed to reach convergence, that is, there was no change in the density of reduced-energy states $\rho(U)$, with increasing simulation steps. The density $\rho(U)$ is sampled by binning the sampled configurations according to their value of U.

10.1. Phase diagram

The phase diagram shown in Fig. 10.1(a) is constructed by using MBAR and shows the (p_B, T) regions where different number of adsorbed B particles are in thermodynamic equilibrium with their gas phase. The B reservoir is assumed to be an ideal gas, so the chemical potential of the reference state is defined as $\mu_{id.gas}^0 \equiv k_B T \ln(\Lambda^3)$. The relationship between pressure $p_{id.gas}$ in the reservoir and the chemical potential μ is $\beta\mu \equiv \beta\mu_{id.gas}^0 + \ln(\beta p_{id.gas})$. The whole output data of REGCMC is sub-sampled every 100 REGC steps, that is, recording data after every attempted replica exchange, to remove correlations in the sampled quantities.

The MBAR@REGC phase diagram is compared to the aiAT@REGC phase diagram (Fig. 10.1(b)), which is calculated via the following steps: (*i*) For each observed number N_B of adsorbed (B) particles in the REGCMC sampling, the lowest LJ total energy configuration is selected. We note that identifying phases denoted by N_B via grand-canonical sampling is not the usual strategy for aiAT. Typically phases are enumerated on the basis of considering many plausible assumed candidate structures and minimization at fixed number of adsorbed particles and fixed unit cell size and shape. In other words, the aiAT study presented in this paragraph is already richer than usual due to the largely unbiased structure sampling. (*ii*) The Gibbs free energy for each of these phases is calculated via:

$$\Delta G_{A, N_B}^f(T, p_B) = F_{A, N_B} - F_{A, N_B=0} - N_B \mu(T, p_B) \tag{10.1}$$

Here, the free energy F_{A, N_B} of the system $A_{18}B_{N_B}$ and $F_{A, N_B=0}$ of the pristine A_{18}

59

slab is approximated by the LJ energies of the two systems, i.e., all the vibrational contributions to the free energy are neglected. There is no vibrational contribution from the surface since it is frozen. However, the adsorbate do vibrate and therefore there are vibrational contributions from adsorbate to the free energy, especially for the large coverages. This is often a justified assumption for systems studies via aiAT [12]. As we will see, it is not a good approximation for this LJ system, at least at larger N_B. (*iii*) As for MBAR@REGC, at each (T_i, μ_j) on a grid the phase with the lowest ΔG^f determines the color of the pixel of size $(\delta T, \delta \mu)$ centered at (T_i, μ_j). This aiAT@REGC approach, used here only for comparing to MBAR@REGC in order single out the role of the vibrational contribution to free energy, including anharmonic effects, is similar to the method recently proposed in Ref. [136]. There, the configurations are sampled by means of an approximated GC scheme at one temperature only and without replica exchange for either temperature or chemical potential. The effect of the reservoir to the free energy is taken care of by an expression similar to Eq. 10.1.

By comparing the two panels of Fig. 10.1, we note that up to $N_B = 18$, the two phase diagrams almost coincide, especially at lower temperatures (in the Appendix. A.1, we show a zoom-in of the region between 60 and 350 K). There are, however, significant differences at larger N_B: There are many more phases in Fig. 10.1(a) that are missing in Fig. 10.1(b) for $N_B > 18$ and the region of stability of larger coverages is shifted to higher temperatures and lower pressures. This can be understood as due to increasingly larger vibrational contributions of adsorbate, especially in the direction z, perpendicular to the slab, while at low coverage the free energy is indeed essentially given by the LJ energy. We come back to this in the next section, after analyzing the structural properties of the different phases.

The analysis of the phase diagram Fig. 10.1(b) reveals that for many values of number of adsorbed B particles, N_B, there is a region of stability in the phase diagram, however, for some specific values of N_B larger stability areas are found. Besides $N_B = 0$(the pristine surface), we recognize $N_B = 18$ as the first complete mono-layer, $N_B = 45$ as the addition of a second complete monolayer, plus a third phase, $N_B = 59$ with a thicker second monolayer (see further). We also identify a large-coverage phase, $N_B = 85$ which can be described by the formation of a "third" layer around 1.9 Å, but in this case the particle distribution does not go completely to zero between second and third layer as it does between first and second, as shown in Fig. 10.2. The diagram extends till the melting (red), vaporization (cyan), and sublimation (blue) line for bulk B particles.

The phase transition curves are derived from the published equations of state for the LJ system. [137–143] We underline that the phase diagram outside the (p,T) region sampled directly via the REGC run is not *extrapolated*. It is obtained as for all the diagram by Boltzmann re-sampling the configurations actually visited, using the measured (reduced) potential energies.

Figure 10.2.: Axial distribution function of adsorbed particles for each N_B composition generated in REGC sampling and identified to be the most thermodynamic stable phase on Fig. 10.1(a). The curves are displaced by 20 units and each dash line is a zero reference line for the curve with the same color.

10.2. Structural properties

The REGC sampling allows for much deeper analysis than the evaluation of the phase diagram. For instance, the structural properties of the adsorbed phases can be characterized in a statistical way. The axial distribution function $\rho(z)$ was calculated by dividing the cell into slabs of width 0.12 Å, parallel to the surface, and collecting a histogram of the number of particles in each slab along the REGC sampling. As shown in Fig. 10.2, the adsorbate has a clear layered structure up to the second layer. For larger N_B, i.e., $N_B > 59$, there are more and more particles adsorbed in the range $1.2 \leq z \leq 1.8$ Å, though another noticeable peak around 1.9 Å occurs. As intuitively predictable, before first layer, the B particle prefers to adsorb on the hollow sites of the surface, the first layer consists of 18 B particles located in all the hollow sites of the 3×3 surface. When the second full monolayer $N_B = 45$ is stable, the B particles occupy the 27 bridge sites of the A_9 surface layer.

To better characterize the structure of the adsorbate layers, in Figs. 10.3a–b and Figs. 10.4a–c we show the $g_{xy}(r)$, i.e., the radial distribution functions (RDF) in the *xy*-

Figure 10.3.: Lateral radial distribution functions $g_{xy}(r)$ for (a) first monolayer, and (b) second monolayer (I), respectively. The blue and pink balls in the insets indicate A and B particles, respectively.

Figure 10.4.: Lateral radial distribution function $g_{xy}(r)$ for (a) relaxed second monolayer (II) A_9B_{59}, average distribution function $< g_{xy}(r) >$ at (200 K, 2.03×10^{-17} atm) state (b), and at (600 K, 8.89×10^{-2} atm) (c) for the same composition. The blue and pink balls in the insets indicate A and B particles, respectively.

plane for the different adsorbate layers (i.e., for B-particles in a slab $z_0 \pm \delta z_0$ as specified in each panel). The structures shown in Fig. 10.4b–c are obtained via MBAR by evaluating Eq. 8.5. We observe that the first monolayer and second monolayer (I) $N_B = 45$ have a $g_{xy}(r)$ characteristic of the solid phase with well-defined peaks and long-range order, whereas for the second monolayer (II) $N_B = 59$, the $g_{xy}(r)$ is more disordered. In the relaxed structure of A_9B_{59} (Fig. 10.4(a)), B particles occupy approximately both hollow and bridge sites, relative to the top A_9 layer and form a ring-like structure around the projection of the A particles. At (200 K, 2.03×10^{-17} atm), the average radial distribution function $\langle g_{xy}(r) \rangle$ of this phase shares some similar peak positions with that of its lowest-energy isomer. It is clear that the ring structure formed by B particles can be still found in the average adsorbate structure though there are a few B particles diffusing

around the projection of the A particles. At (600 K, 8.89×10^{-2} atm), more and more B particles diffuse and the ring structure is not as noticeable as before. Consistently, the $\langle g_{xy}(r) \rangle$ shares a few major peaks with that of its lowest-energy isomer, but they appear more smeared.

The example of $\langle g_{xy}(r) \rangle$ at the two state points was selected in order to demonstrate the power of the REGC sampling to reveal detailed thermodynamic information on the simulated system. A crucial observation is that such information is already contained in the REGC sampling, no further simulation is needed, only post-processing statistical analysis of the sampled data points is required.

Coming back to the differences between aiAT@REGC and MBAR@REGC phase diagrams (Fig. 10.1), we observe, in Fig. 10.2 that up to the complete first monolayer ($N_B = 18$), the adsorbed particles have essentially no freedom to move in the z direction. As soon as the second monolayer is established, the adsorbed particles display a broader and broader distribution along the z direction. The distribution becomes even bimodal for $N_B \geq 62$. This enhanced configurational freedom creates a large, negative, vibrational free energy contribution that stabilizes the higher coverages compared to when only the energetic contribution is taken into account (as in the aiAT@REGC phase diagram).

10.3. Order-disorder phase transition temperature and pressure

The heat specific C_v is evaluated for the adsorbate surface in order to identify the temperature and pressure condition of the order-disorder phase transition. The C_v is calculated by the following equation:

$$C_{v,\,(T,\,p_{H_2})} = \frac{\langle E^2 \rangle_{(T,\,p_{H_2})} - \langle E \rangle^2_{(T,\,p_{H_2})}}{k_B T^2} \tag{10.2}$$

where E is the total LJ energy of the system in this application.

In practice, the ensemble averages of E and E^2 are evaluated at each state point (μ, β) of interest. For example, in Fig. 10.5(a), p_B is equal to 10^{-20} atm and T ranges from 60 to 650 K. The corresponding chemical potentials are calculated using $\beta\mu \equiv \beta\mu^0_{id.gas} + \ln(\beta p_B)$ every 1 K. The ensemble average value of E at given state point (μ,

63

β) and phase i, in the MBAR formalism, is estimated over the sampled points via:

$$\langle E \rangle_{\mu,\beta,i} = \sum_{n=1}^{\Omega_i} \frac{E(\boldsymbol{R}_n)\, c_{\mu,\beta}^{-1}\, q(\boldsymbol{R}_n; \mu,\beta)}{\sum_{l,m} \Omega_{l,m,i} c_{\mu_m,\beta_l}^{-1} q(\boldsymbol{R}_{l,m,i}; \mu_m,\beta_l)} \tag{10.3}$$

where Ω_i is the number of samples in phase i and therefore the sum over n runs over all samples belonging to phase i. Similarly, $\Omega_{l,m,i}$ is the number of samples in phase i in each sampled state point (m,l). $q(\boldsymbol{R}_n; \mu,\beta)$ is the grand-canonical density function, which is defined in Chapter. 8. $E(\boldsymbol{R}_n)$ is the LJ total energy of the whole configuration $\boldsymbol{R}_n$. The expectation value of $\langle E^2 \rangle_{\mu,\beta,i}$ follows the same way to estimate. Thus, the C_v is calculated at each (μ, β) state.

The results are illustrated in Fig.10.5. The following information are obtained when combining the Fig. 10.1(a) and Fig. 10.5: At $p_B = 10^{-20}$ atm shown in Fig. 10.5(a), the peak of C_v at around 373 K indicates the phase transition from the pristine to the phase with $N_B = 10$ transition; the phase transition from $N_B = 15$ to 1st monolayer occurs at around 358 K; at around 282 K, the 1st monolayer transforms into the $N_B = 34$ phase; at 268 K, the $N_B = 34$ phase transforms into the 2nd monolayer (I); the peaks at 172 K and 154 K signify the transitions from the 2nd monolayer (II) into the $N_B = 62$ phase and from the $N_B = 62$ phase into the $N_B = 76$ phase. The same phase transitions occur at $p_B = 10^{-15}$ atm and $p_B = 10^{-10}$ atm, but the corresponding peaks shift to higher temperature range as illustrated in 10.5(b) and 10.5(c). For instance, the transition from the pristine to the phase with $N_B = 10$ transition occurs at around ($T = 455$ K, $p_B = 10^{-15}$ atm) and ($T = 583$ K, $p_B = 10^{-15}$ atm), respectively.

From the pristine (ordered structure) to the $N_B = 10$ phase, B particles randomly adsorb on the hollow sites of the slab A with the vacancies diffusing (disordered structure compared to the pristine). Therefore, the system goes from *order to disorder* when increasing N_B. However, the hollow sites are fully occupied in the 1st monolayer (ML) phase (ordered structure) and there is no degree of freedom for the vacancies to diffuse in the 1st ML. Therefore, the transition from the $N_B = 15$ phase to the 1st monolayer is from *disorder to order*.

The similar case for the transitions from the 1st monolayer to $N_B = 34$ phase and from $N_B = 34$ phase to the 2nd monolayer (I). The particle B fully occupies hollow sites forming the 1 ML and adsorbs on the bridge site to form the 2nd monolayer. In the beginning of the formation of the 2nd monolayer, the particle B has much degree of freedom to choose which bridge site to adsorb, thus leaving the vacancies in the 2nd

monolayer diffusing (disorder structure). After the B particles occupy all the bridge site, the 2nd monolayer is an ordered structure.

The peaks at 154 K and 172 K at $p_B = 10^{-20}$ atm become the double peaks with the same C_v value at $p_B = 10^{-5}$ atm, finally merge into a broader peak at $p_B = 1$ atm.

The phase boundary can be estimated according to the above information. For instance, as shown in the left panel of Fig. 10.6, the solid grey line is the estimated phase boundary between the pristine and $N_B = 10$. The solid green line is the estimated phase boundary between the and $N_B = 15$ the 1st monolayer. In the right panel of Fig. 10.6, the average number of B particles ($\langle N_B \rangle$) is calculated as a function of temperature at constant pressures of $p_B = 10^{-20}$, 10^{-15}, and 10^{-10} atm.
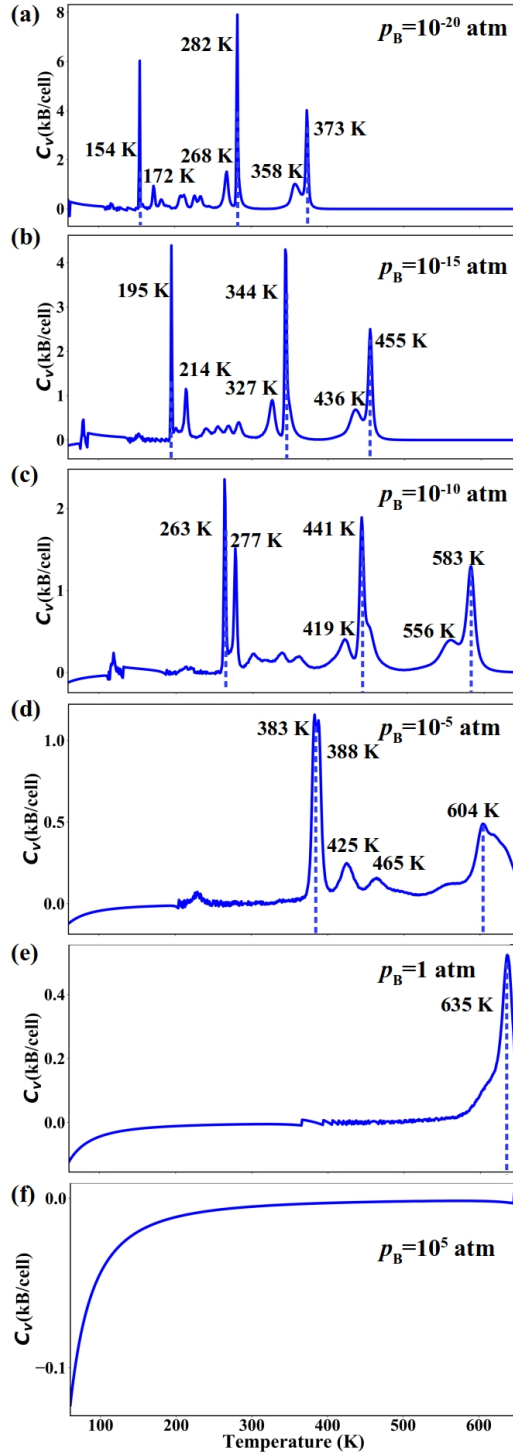
Figure 10.5.: The heat specific C_v of adsorbates vs. T at constant pressures, that is, $p_B = 10^{-20}$, 10^{-15}, 10^{-10}, 10^{-5}, 1, and 10^5 atm. The blue dash lines denote the peaks of heat specific indicating the phase transitions.
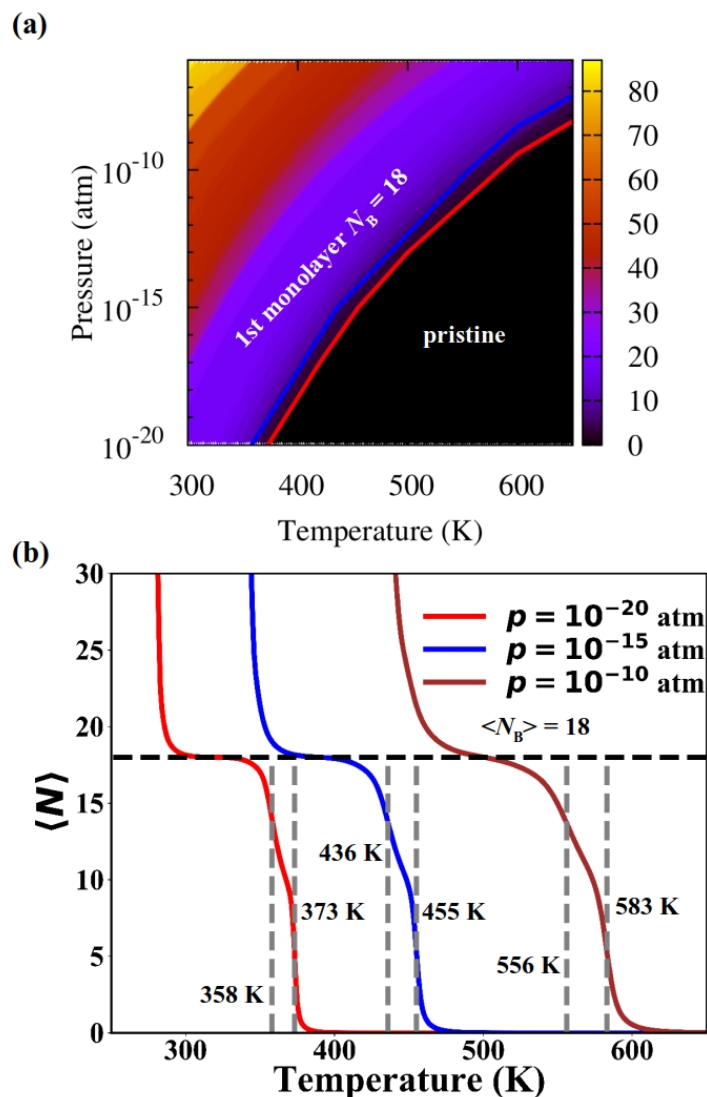
Figure 10.6.: (a) Phase diagrams of a gas-phase (particles B) in contact with a frozen fcc(111) surface calculated via by MBAR from the REGCMC sampling. The red line is the phase boundary between the pristine and $N_B = 10$. The blue line is the phase boundary between $N_B = 15$ and the 1st monolayer ($N_B = 18$). (b) The average number of particle B $\langle N_B \rangle$ as a function of temperature at constant pressures, that is, $p_B = 10^{-20}$, 10^{-15}, and 10^{-10} atm. The black dash line denotes the $\langle N_B \rangle = 18$. The grey dash lines denote the transition temperatures correspond to the right two peaks in Fig. 10.5(a-c)

11. *Ab initio* Si_2H_N and Si_4H_N clusters

The binary clusters of silicon and hydrogen play key roles in the chemical vapor deposition of thin silicon films and coatings, and photoluminescence of porous silicon. However, most of the previous research on silicon hydrides focused on the search of global minima structures, but the decisive issue of stability and metastability of silicon hydrides including anharmonic effect at realistic conditions (exchange of atoms with an environment) has not been addressed so far.

The REGC algorithm coupled to *ab initio* MD was applied to identify the thermodynamically stable and metastable compositions and structures of Si_MH_N (M=2, 4) clusters at realistic temperatures and pressure of the molecular hydrogen gas. Both the hydrogen atom and hydrogen molecule are allowed to exchange between the cluster and the reservoir, so that not only the adsorption of molecule but the dissociative atomic adsorption are treated in the simulation. All DFT calculations were performed with the all-electron, full-potential electronic-structure code package FHI-aims [86]. We used the Perdew-Burke-Ernzerhof (PBE) [30] exchange-correlation functional, with a correction for the van der Waals interactions (vdW), computed using the Tkatchenko-Scheffler scheme [109]. A "tier 1" basis for both Si and H with "light" numerical settings were employed. All aiMD trajectories between REGC attempted moves (0.02 ps each) are performed in the NVT ensemble. The equations of motion were integrated with a time step of 1 fs using the velocity-Verlet algorithm [80]. The stochastic velocity rescaling thermostat was adopted, with a decay-time parameter $\tau = 0.02$ ps, to sample the canonical ensemble [144]. Tests for the accuarcy of the choice of this time step is included in Appendix A.2, for H_2 molecule. The actual τ vaule has little effect on the performance of stochastic velocity rescaling thermostat, but usually τ is used to be $\approx 20 - 50$ time steps (here 20 time steps). The reflecting conditions to confine the system in a sphere of radius 4 Å are imposed via PLUMED [145] interfaced with FHI-aims, by applying a repulsive polynomial potential of order 4. The repulsive potential is expressed as $V_{\text{wall}} = \text{Kappa}(s - \text{LIMIT})^4$, where Kappa is the energy constant and LIMIT is the limited value of collective variable s. This avoids that H atoms diffuse at arbitrary distance

from the Si_M cluster, without perturbing the statistics as the cutoff distance is such that the H atoms are not any more interacting with the Si cluster.

11.1. Phase diagram

11.1.1. Si_2

Twenty replicas of Si_2 are selected in contact with different thermodynamic states, that is, with temperatures of 500, 650, 800, and 950 K and H_2 chemical potentials of -0.2, -0.16, -0.12, -0.08, and -0.05 eV. The selection of the temperature range is made according to the experimental deposition temperature of chemical vapor deposited silicon films [146, 147], which starts from around 600 K. Ideally, the lowest μ_{H} should be around -1.2 eV, which is the half adsorption energy of H_2 on Si_2, according to our DFT-PBE calculations. However, in order to focus the sampling on a more interesting region, where more H atoms are adsorbed, we started from a much higher minimum μ_{H_2}. The H_2 molecule adsorption includes the association adsorption where individual molecules remain intact and the dissociative adsorption where the H_2 molecule is dissociated into 2 H atoms. However, there exist strong activation barriers ($\sim$ several eV) for the dissociation. Here both H_2 molecule and H atom attempt to adsorb on the surface, thus circumventing activation barriers for the dissociation. *Ab initio* molecular dynamics is performed for each system after exchanging particle with the reservoir or swapping with neighboring replicas. For this REGCMD study, x_0 is chosen as 0.9.

For comparison, we analyzed the stability of Si_2H_N clusters using *ab initio* atomistic thermodynamics (aiAT) in Fig. 11.1(a). For each number of adsorbed hydrogens N_{H}, the lowest DFT energy isomer is identified among all the configurations obtained along the REGC *ab initio* MD sampling. The Gibbs free energy of each phase is calculated as:

$$\Delta G_f(T, p_{\text{H}_2}) = F_{\text{Si}_M\text{H}_N} - F_{\text{Si}_M} - N\mu_{\text{H}}(T, p_{\text{H}_2}) \tag{11.1}$$

Here, $F_{\text{Si}_M\text{H}_N}$ and F_{Si_M} are the Helmholtz free energies of the Si_MH_N and the pristine Si_M cluster (at their configurational ground state), respectively, where $M = 2, 4$. μ_{H_2} is the chemical potential of the hydrogen molecule. $F_{\text{Si}_2\text{H}_N}$ and F_{Si_2} are calculated using DFT information and are expressed as the sum of DFT total energy, DFT vibrational free energy in the quasi-harmonic approximation, as well as translational, and rotational free-energy contributions of H_2. The dependence of μ_{H_2} on T and p_{H_2} is calculated

Figure 11.1.: (a) aiAT@REGC phase diagram and (b) MBAR@REGC phase diagram of Si_2 with H_2 reactive gas phase. MBAR@REGC phase diagrams of (c) the number of chemically adsorbed H on the Si_2 cluster. (d) aiAT@REGC phase diagram and (e) MBAR@REGC phase diagram of Si_4 with H_2 reactive gas phase. MBAR@REGC phase diagrams of (f) the number of chemically adsorbed H on the Si_4 cluster.

using the ideal (diatomic) gas approximation with the same DFT functional as for the clusters. [17, 44, 148] So p_0 here is calculated as follows:

$$p_0 = [(\frac{2\pi m}{h^2})^{\frac{3}{2}}(k_B T)^{\frac{5}{2}}(\frac{8\pi^2 I_A k_B T}{h^2})\frac{e^{(\frac{k_B T}{E_{\text{DFT}}})}}{e^{(\frac{h v_{\text{HH}}}{k_B T})-1}}] \tag{11.2}$$

E_{DFT} is the DFT total energy, m is the mass, I_A is the inertia moments, v_{HH} is the H-H stretching frequency of 3080 cm^{-1}. The (p_{H_2}, T) phase diagram of Si_2H_N cluster is also constructed via the MBAR@REGC method. As shown in Fig. 11.1(b), besides Si_2, Si_2H_2, and Si_2H_6, which have their wide stability regions revealed in both phase diagrams, there is a narrow (T, p_{H_2}) stability domain for Si_2H_4, which is only revealed by the MBAR@REGC phase diagram that includes the anharmonic contributions to the free energy. Another difference between two phase diagrams is that the stable (p_{H_2}, T) range of each phase is quite different. The Si_2H_N phases in Fig. 11.1(b) may include not only chemically adsorbed H atom, but also H_2 molecules, weakly attracted to the Si

dimer (and therein adsorbed hydrogen atoms). All the weakly bonded H_2 molecules and chemisorbed H atoms together with Si atoms are collectively a thermodynamic phase, identified by the number N of hydrogen atoms. As shown in A.9, the density of H_2 gas in Si_2H_{20} phase at ($T = 500$ K, and $p_H = 2.3 \times 10^4$ atm) is orders of magnitude larger than the ideal H_2 gas phase at the same condition, which indicates that the system consisting of chemisorbed H atoms and physisorbed H_2 molecules is in equilibrium with a much less dense gas phase at the same chemical potential. The details regarding how the H_2 density is calculated is included in Appendix. A.2. In order to further investigate the chemisorbed phase stability, we construct the phase diagram (Fig. 11.1(c)) for a new observable: the number of adsorbed H atoms. A H atom is considered adsorbed on the Si cluster when the distance to the closest Si is smaller than 1.7 Å.

Figure 11.2.: Structures of Si_2H_N and Si_4H_N, found by the REGC sampling, that have a region of thermodynamic stability in the phase diagrams of Fig. 11.1.

11.1.2. Si$_4$

Twenty thermodynamic states for the Si$_4$H$_N$ system are selected, with temperature of 560, 685, 810, and 935 K, and chemical potentials of -0.3, -0.2, -0.17, -0.14, and -0.11 eV. The lowest value of μ_{H} is selected as a bit larger than the half adsorption energy (-0.6 eV) of H$_2$ on Si$_4$. The other settings are the same as in Si$_2$ simulation. As for the Si$_2$H$_N$ case, we construct both the aiAT@REGC and MBAR@REGC phase diagram, for comparison, plus the MBAR@REGC phase diagram for the adsorbed H atoms. In Fig 11.1(d) and 11.1(e), the results indicate that two stable Si$_4$H$_4$ and Si$_4$H$_6$ are missing in aiAT@REGC phase diagram. Si$_4$H$_4$ and Si$_4$H$_6$ have considerable larger stable range in chemisorbed phase diagram shown in Fig 11.1(f) than in both physi- and chemisorbed one. Besides, the stable (p_{H_2}, T) range of each phase transitions are quite different in phase diagrams calculated by two method.

11.2. Structural information of silicon hydrides

In Fig. 11.2, we show the structures of each thermodynamically stable cluster size appearing in the phase diagrams. All previously reported structures [31, 149] are found in our REGC *ab initio* MD simulations and illustrated in Fig. A.5. Besides, we identified many other isomers at each composition, via the REGC *ab initio* MD sampling, as shown in Fig. A.5.

In this chapter, the replica-exchange grand-canonical (REGC) *ab initio* molecule dynamics is applied to determine the phase diagram of Si$_M$ (M = 2, 4) in a H$_2$ gas phase, when coupled with MBAR. For comparison, the *ab initio* atomistic thermodynamics (aiAT) is also used to calculate the phase diagram of Si$_M$ (M = 2, 4) in a H$_2$ gas phase. The vibrational free energy is treated at harmonic approximation. Moreover, the aiAT study here is richer than the typical one since the lowest DFT total energy configurations for every composition are selected in the REGC sampling rather than enumerated on the basis of considering many plausible assumed candidate structures. Both the aiAT@REGC and MBAR@REGC phase diagrams reveal some of the same thermodynamically stable phases, e.g., Si$_2$, Si$_2$H$_2$, and Si$_2$H$_6$ for Si$_2$ cluster and Si$_4$, Si$_4$H$_2$, and Si$_4$H$_8$ for Si$_4$ cluster. However, there are significant differences between: aiAT@REGC phase diagram and REGC@MBAR phase diagram: (*i*) some phases are missing in aiAT@REGC phase diagram but revealed in MBAR@REGC phase diagram;(*ii*) the T-p

stable range for the same phase is different in both phase diagram. All these differences indicate the importance of the anharmonic contribution to the phase diagram.

12. *Ab initio* Si(100) surface in contact with H_2 reactive atmoshpere

In this chapter, we apply REGC *ab initio* MD to determine the phase diagram of Si(100) surface in a realistic H_2 atmosphere. The adsorption of molecular hydrogen on Si(100) surface represents a prototype for the adsorption of molecules on covalent surfaces. Moreover, the interaction of hydrogen with silicon is of great technological relevance for, e.g., the etching and passivation of Si surfaces or the growth of Si crystals due to the crucial role of hydrogen in passivating dangling bonds. [150] Despite of its great importance, few studies have addressed the reconstruction of the Si(100) surface at realistic p_{H_2}, T conditions. The structure of the hydrogen-covered silicon surface has turned out to be a complex function of coverage and adsorption/annealing temperature. There is a general agreement that (2×1) pattern formed in contact with atomic hydrogen at 600 K. [151] An unexpected (3×1) structure was reported at around 4Tabl00 K. [34] In order to include adsorption patterns $(1 \times 1, 2 \times 1$ and $3 \times 1)$, we choose Si(100)-(3×3) and (4×4) systems to address the adsorption of hydrogen on silicon surface. Both hydrogen molecule and atomic hydrogen are only allowed to adsorb on the surface so that the dissociation barrier of H_2 molecule is circumvented in the Grand-Canonical scheme. We use the example of H_2 adsorption/dissociation/desorption over Si(100) surface model to illustrate the concepts and conclusions that can be derived from such an *ab initio* surface phase diagram calculated by our REGCMD method. Furthermore, a structural descriptor — coordination histogram — is defined as the observable of interest to reveal the structural information at realistic T, p_{H_2} condition. Using this structural descriptor, the unexpected (3×1) structure is identified in our calculated phase diagram at around 400 K, which has a good agreement with the experimental results. [34] The REGC *ab initio* MD simulation of Si(100)-(4×4) is in the progress, so only the results of Si(100)-(3×3) are discussed in this chapter.

The model system consists of 3-layer Si slab with a 3×3 lateral supercell, periodic along the [110] and [1$\bar{1}$0] directions. The benchmark study of the number of layers in

the Si slab reported in Appendix A.2 shows that the relative stability of surface energy for 12 different Si(100) structures and 13 Si(100)-H structures are converged when the number of layers in the silicon slab is at least three. The vacuum thickness between adjacent slabs along [001] is set at 100 Å. In FHI-aims [86], localized numeric atom-centred basis is used, which enables large vacuum distances between the slab images with a minor increase in computational cost. The gas H_2 molecule and atomic H are only allowed to insert in the "surface" zone. We defined the "surface" zone as a slab of height 3.0 Å above the slab along [001] direction, starting from the topmost atoms of Si(100) surface. The height value is chosen so that there is little interaction when H atom/molecule is 3.0 Å away from the surface. Further, an additional layer of 18 H atoms is arranged at the bottom of the slab to saturate dangling bonds of the Si atoms at the lower boundary.

In the REGCMD simulation, 16 replicas are defined, i.e., 4 different T ranging from 360 K to 960 K with an interval of 200 K and 4 different μ : -0.6, -0.4, -0.2, and -0.1 eV. The adsorption energy of H_2 molecule on Si(100)-3 $\times$ 3 surface is calculated to -1.8 eV at DFT-PBE level. The lowest chemical potential is chosen around half of it. In this study, a higher lowest chemical potential is chosen to focus on the sampling of adsorbate structures. The temperatures are selected to encompass the range of experimental results (600 K [151] or 400 K [34]). For this REGCMD simulation, 90% attempts to exchange particle with reservoir for each replica and 10% attempts to perform replica exchange. All aiMD trajectories are performed in an NVT ensemble. The equations of motion were integrated with a time step of 1 fs using the velocity-Verlet algorithm [80]. The stochastic velocity rescaling thermostat was adopted, with a decay-time parameter τ = 0.02 ps, to sample the canonical ensemble [144]. The reflecting wall is positioned 3 Å above the surface to confine the system in "surface" zone and is imposed via PLUMED [145] interfaced with FHI-aims. All DFT calculations were performed with the all-electron, full-potential electronic-structure code package FHI-aims [86].The Perdew-Burke-Ernzerhof (PBE) [30] exchange-correlation functional is used. A "tier 1" basis for Si and H with "light" numerical settings was employed.

12.1. Phase diagram

The phase diagram of Si(100) in contact with H_2 reactive gas atmosphere is obtained by MBAR as shown in Fig. 12.1(a). A variety of different phases are revealed: Besides

the bare surface, The Si(100)-H phase denoting the Si(100) surface with one adsorbed hydrogen atom has a narrow stable region at low temperature ($T < 500$ K) and high temperature ($T > 800$ K) ranges. In contrast, Si(100)-H_2 has a considerable region of phase stability in the temperature ranging from 500 to 800 K. While the stable region of Si(100)-H_3 is just a tiny piece in high T range, the stable region of Si(100)-H_4 is running through all the T range, and gradually becomes narrow with T increasing. The free energy of Si(100)-H_5 and Si(100)-H_6 two phase calculated by MBAR are very close to each other and the difference is within a few $k_B T$, regarded to be coexistence. The region of stability of phases Si(100)-H_N ($8 \leq N \leq 12$) is in the relatively low T range and high p_{H_2}.

The thermodynamic variable N does not distinguish the chemisorbed hydrogen and physisorbed hydrogen on the surface. In most cases, however, we are interested in the phases only including the chemisorbed ones, that is, the hydrogen molecule reacts with the silicon atom and the covalent bond is formed between hydrogen and silicon atoms. Therefore, the phase diagram is constructed by MBAR shown in Fig. 12.1(b) when only including the number of chemisorbed hydrogen in the configurations. A hydrogen atom is regarded as chemically adsorbed on to silicon surface when the shortest H-Si distance is smaller than 1.7 Å. To distinguish, Si(100)-H_N is referred to a phase Si(100) surface with N hydrogen while Si(100) surface with N chemisorbed hydrogen is termed as Si(100)H_N. Compared to the phase diagram in Fig. 12.1(a), the two diagrams share some similarities. For instance, the stable region of bare surface is kept constant and the stable T-p range of Si(100)H_{12} slightly expands to the Si(100)-H_{14} region. There are several differences between these two diagrams. The most significant one is that in the chemisorbed phase diagram, at most only 12 hydrogen atoms form the covalent bonds with silicon atoms on the surface. This finding is actuated by electron counting rule. We will come back to this issue later and explain together with the most probable structure in Fig. 12.3. Besides, the stable range of Si(100)H becomes broader and runs through the whole T range while a small stable range of Si(100)H_2 is remaining. Similarly, for $N = 3$, the stable range extends to 600 K, accordingly, Si(100)H_4 stable region shrinks below 600 K. The coexistence region of Si(100)-H_5 and Si(100)-H_6 in Fig. 12.1(a) is dominated by Si(100)H_5 with a small part of Si(100)H_6. The other coexistence phase range occurs for Si(100)H_8 and Si(100)H_9.
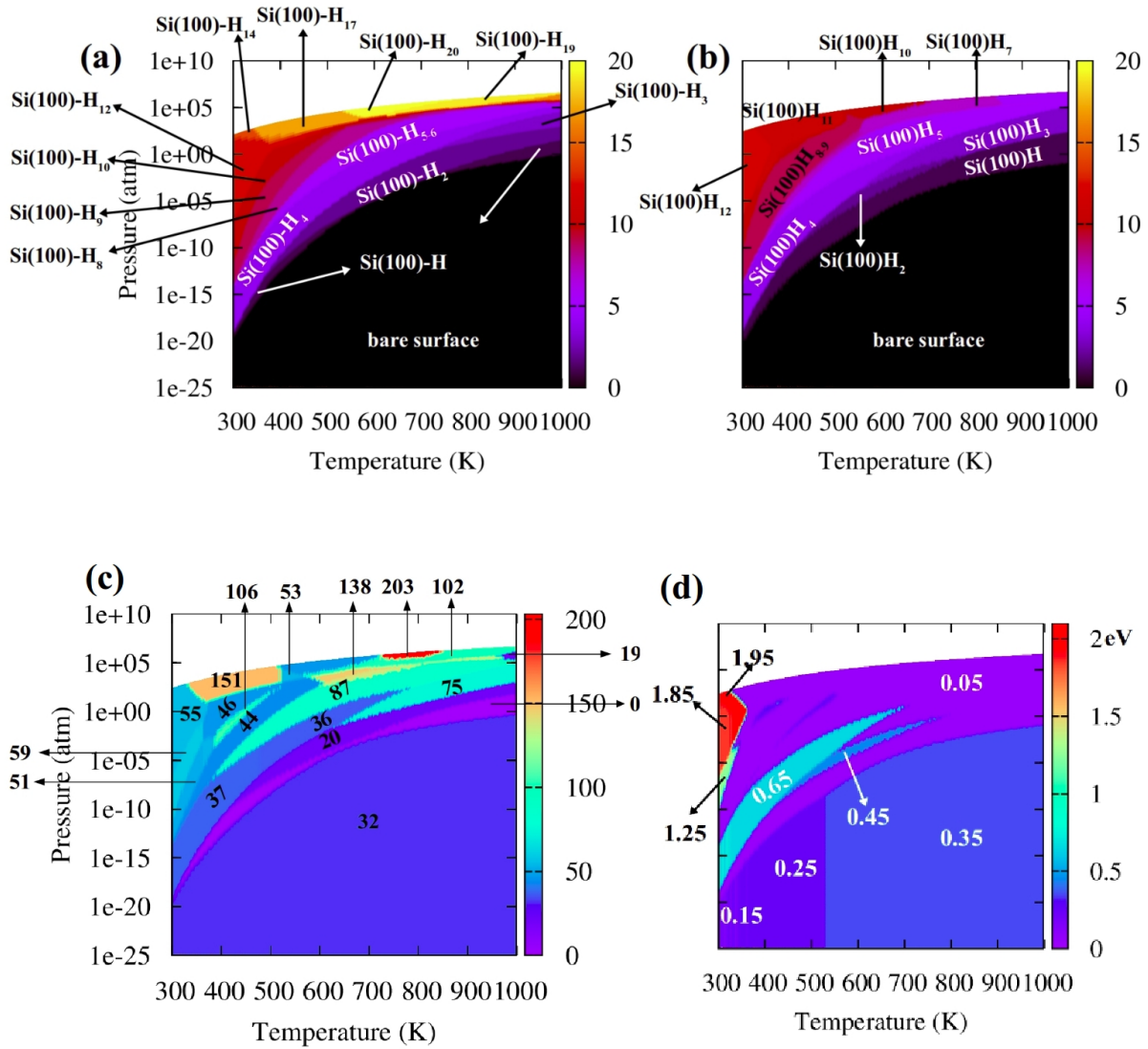
Figure 12.1.: Phase diagram of (a) Si(100) in a H_2 gas phase. Phase diagram of (b) the number of chemisorbed hydrogen on the Si(100) surface. HOMO-LUMO gaps T-p map in panel (c) is in eV at HSE level. Phase diagram of the coordination histogram (Ht_{coord}) of Si(100)-H_N in panel (d). The different color corresponds to the index of the coordination histogram of Si(100)-H_N structures.

12.2. Structural and electronic properties of Si(100)-H$_N$ surfaces

Up to this point, the phase diagrams in Fig. 12.1(a) and Fig. 12.1(b) only provide the information on how many number of (chemically) adsorbed H atoms in the stable phases and their own thermodynamic phase stable region. Little structural information is revealed for each thermodynamic stable Si(100)-H$_N$ phases. In order to reveal structural details, one structural observable was selected, namely, the coordination histogram of Si(100)-H$_N$ surfaces referred as Ht_{coord}. The Ht_{coord} is obtained by constructing a coordination histogram (distribution of Si-atoms coordination number) for each surface configuration including the number of Si atoms bonded to each Si atom and the number of H atoms bonded to each Si atom. [152] When the shortest Si-Si distance is less than 2.8 Å (120% proportional to 2.32 Å, the Si-Si shortest in diamond), the two Si atoms are regarded to be bonded together. The threshold of Si-H bond is the same threshold (1.7 Å) as that for the chemically adsorbed H atoms. By takin the Si(100)H$_{12}$ as an example (shown in Fig. 12.2), there are three green Si atoms and each coordinating with other two Si atoms and two H atoms. There are six purple Si atoms and each coordinating with other three Si atoms and one H atom. The Ht_{coord} of this structure is [0, 3, 6, 0, 0, 0, 6, 3]. The T-p phase diagram (map) of Ht_{coord} is constructed through post-processing
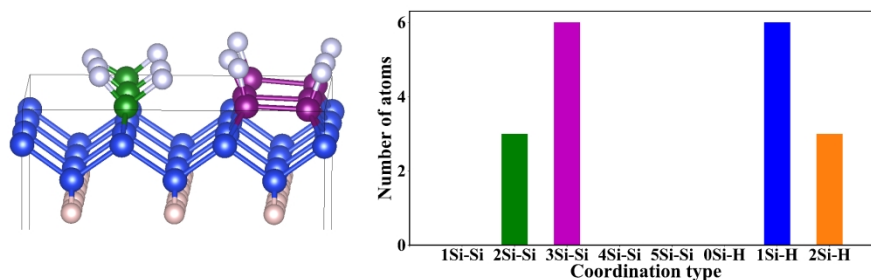
Figure 12.2.: Bond coordination histograms of the most stable Si(100)H$_{12}$.

analysis via Ht_{coord} as input to MBAR and shown in Fig. 12.1(c) The numbers in Fig. 12.1(c) illustrated by different colors are the indexes of different Ht_{coord}. The detailed information of each Ht_{coord} appearing on the map are listed in the Table. 12.1. The first column in the table shown as Table. 12.1 indicates the index of different coordination histogram for the Si(100)-H$_N$ configurations dominating the thermodynamic stable

index	1 Si-Si	2 Si-Si	3 Si-Si	4 Si-Si	5 Si-Si	0 Si-H	1 Si-H	2 Si-H
0	0	3	6	0	0	8	1	0
19	0	3	5	0	1	7	2	0
20	0	3	6	0	0	7	2	0
28	0	3	6	0	0	5	4	0
32	0	3	6	0	0	9	0	0
36	0	3	6	0	0	6	2	0
37	0	3	6	0	0	7	0	2
44	0	3	6	0	0	2	6	1
45	0	3	6	0	0	3	4	2
46	0	3	6	0	0	2	4	3
51	0	3	6	0	0	1	7	1
53	0	3	6	0	0	3	3	3
54	0	3	6	0	0	0	7	2
55	0	3	6	0	0	0	6	3
59	0	3	6	0	0	1	6	2
75	0	3	6	0	0	6	3	0
87	0	3	6	0	0	4	5	0
99	0	3	6	0	0	5	3	1
102	0	3	6	0	0	4	3	2
106	0	3	6	0	0	2	5	4
108	0	3	6	0	0	3	6	0
138	0	3	6	0	0	4	4	1
147	0	3	6	0	0	3	5	1
151	0	3	6	0	0	1	5	3
203	0	5	4	0	0	3	4	2

Table 12.1.: Table contains the coordination histogram (Ht_{coord}) of Si(100)-H$_N$ structures, found by the REGC sampling, that have a region of thermodynamic stability in the phase diagrams of Fig. 12.1(b). The index of the first column in the table corresponds to the number Fig. 12.3.

region on the phase diagram in Fig. 12.1. The second, third, forth, fifth and sixth columns represent the number of Si atom which bonds with one, two, three, four and five Si atoms. The last three columns signify the number of Si atoms which bond to zero, one or two hydrogen atoms.

According to the T-p map of Ht_{coord}, the reconstruction of bare Si(100)-(3 × 3) surface has index 32 with the coordination histogram of $[0, 3, 6, 0, 0, 9, 0, 0]$. That is three Si atoms with Si-Si coordination number of 2, and six Si atoms with Si-Si coordination number of 3. The representative configuration is illustrated in Fig. 12.3. The so-called representative configuration is explained in Sec. 12.4. Silicon crystals have the diamond structure, i.e. the atoms are sp^3 hybridized and bonded to four nearest neighbors in tetrahedral coordination. Therefore, each Si atom on the top layer has two dangling bonds. The surface energy is lowered by reducing the number of dangling bonds, and this leads to a wide variety of surface reconstructions on silicon surfaces. There are four well-known reconstruction models, that is, the symmetric p(2 × 1) [153], asymmetric p(2 × 1) [154, 155], asymmetric p(2 × 2) [156], and asymmetric c(4 × 2) [157]. The periodicity of above four reconstruction models is not compatible with (3 × 3) supercell, therefore they cannot appear exactly. However, each surface silicon atom tends to bond to a neighboring atom along the [110] direction using one of its dangling bonds. Thus, a row of silicon dimers (the purple balls) is created similar to the dimers row in asymmetric-p(2 × 1) model where one end of the dimer is up while the other end is down. Due to (3 × 3) periodicity, the green Si atoms can not form dimer to further reduce the number of dangling bond.

For Si(100)H$_{12}$, the Ht_{coord} is $[0, 3, 6, 0, 0, 0, 6, 3]$. The sum of the Ht_{coord} is 18, which means all the dangling bond of the top surface Si atoms are saturated either by Si-Si bonds or Si-H bonds, in turns, obeying electron counting rule. The representative structure of Si(100)H$_{12}$ is numbered as 55 shown in Fig. 12.3. The purple Si atoms form the dimer row decreasing one dangling bond for each purple atom. Each purple Si atom is also chemically bonded with one H atom, saturating the other dangling bond. The green Si atoms have no neighboring Si atoms to form dimer row, and each is bonded to two H atoms. Notice that, the dimer row forming by purple Si atoms in Si(100)H$_{12}$ is significantly different to that of Si(100) surface. Here the Si-Si dimer is almost flat and similar to the that of symmetric p(2 × 1) model. The similar case is for the green Si atoms the position of which is about the same position in perfect crystal. This H-saturated Si(100)-(3 × 1) phase is in excellent agreement with the reported experimental

Si(100)-(3×1) phase in Ref. [34] at around 400 K.

There are two different Ht_{coord} identified for Si(100)H$_4$, indexed to 37 and 36, respectively. At $T < 500$ K and $p_{\text{H}_2} < 4.0 \times 10^{-7}$ atm, the most probable coordination histogram $[0, 3, 6, 0, 0, 6, 0, 2]$ dominates while the $[0, 3, 6, 0, 0, 2, 1]$ gradually takes the place with increasing T and p_{H_2}. The Si-Si coordination number has not changed between the histogram 37 and histogram 36. But the Si-H coordination number varies from two SiH$_2$ units to one SiH$_2$ unit and two SiH units, where SiH$_2$ unit indicates one Si atom bonds to two H atoms while SiH unit means one Si atom bonds to one H atom.

For Si(100)H$_{11}$, at low pressure ($p_{\text{H}_2} < 2.0 \times 10^{-2}$ atm), the 54 Ht_{coord} is found to be the most probable one, the representative configuration of which shares the similarity with that of Si(100)H$_{12}$ despite of one missing H atom. For $p_{\text{H}_2} > 4.8 \times 10^2$ atm, the 151 Ht_{coord}, that is, $[0, 3, 6, 0, 0, 0, 1, 5, 3]$ become dominative. By comparing the two representative structures, the middle purple Si-Si dimer is used to be in 54 and breaks in 151. One is bonded with two H saturators and the other is bonded to the other neighboring Si atom

Overall, for different phases, at low T and low p_{H_2}, the Si-Si reconstruction pattern and the adsorption pattern are the precursors of those appearing in the 55 representative configuration. That is, the neighboring purple Si atoms tend to bond to each other forming the Si dimer row, and the remaining dangling bond of each purple Si atom is saturated by adsorbing one H atom while the only choice for remaining three green Si atoms to reduce their dangling bond is the adsorption two H atoms for each. At high T and high p_{H_2} of the stable region for each phases, the 55-like prototype breaks. The middle Si dimer breaks and each Si atom bonds to its another neighboring Si atom. Accordingly, the adsorption pattern changes.

Though the hydrogenated silicon surfaces are often used as the prototypical semi-conductors adsorption, little reported on their electronic properties as a function of temperature and pressure of the H$_2$ gas reservoir. Here the T-p map of the HOMO-LUMO gap is calculated shown in Fig. 12.1(d). The HOMO-LUMO is evaluated via the HSE06 hybrid xc functional. [107, 108] The very interesting findings are for the odd number of chemisorbed H phases, the HOMO-LUMO gap is close to 0 eV (0.05 eV is the center of the bin while the size of bin is 0.1 eV). The HOMO-LUMO gap, however, for the even number of chemisorbed H phases, gradually increases with the number of chemisorbed H atoms increasing. Besides, the HOMO-LUMO gap increases from 0.15 eV, 0.25 eV to 0.35 eV with the increasing T and p_{H_2}.
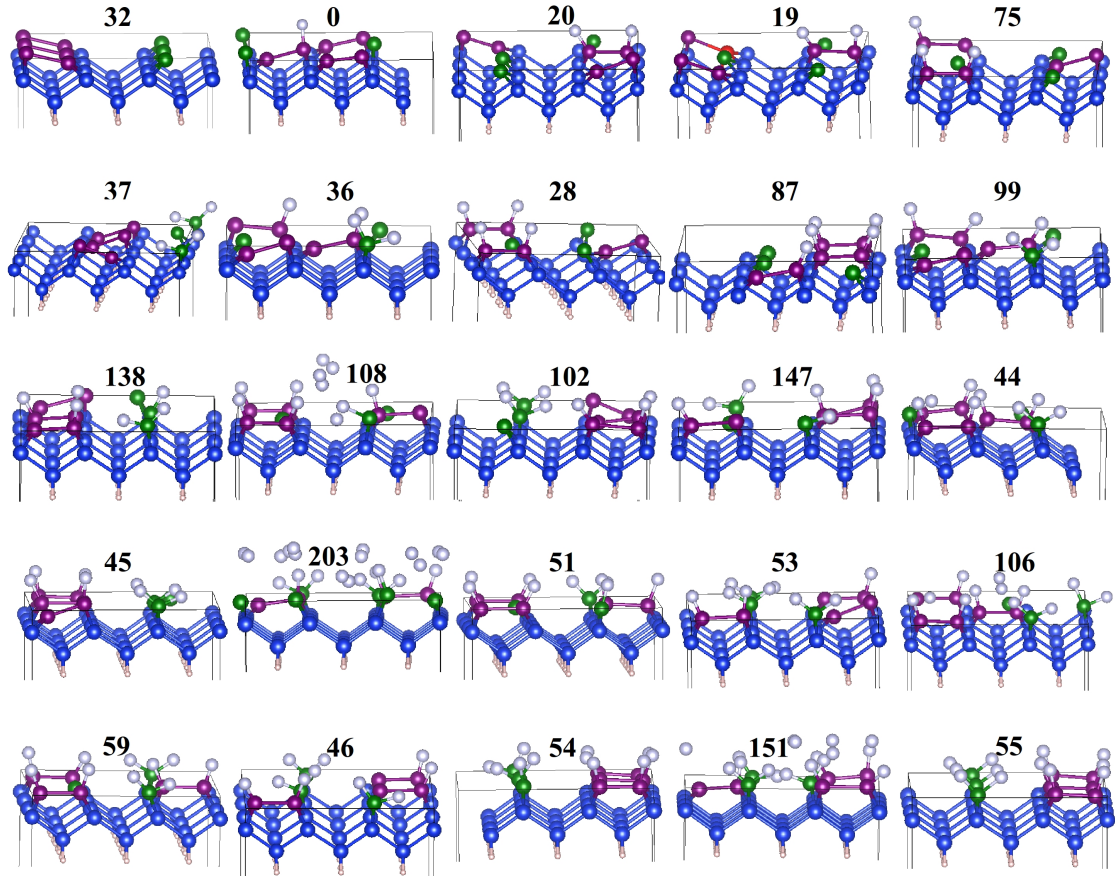
Figure 12.3.: The representative Si(100)-H$_N$ configurations share the same histogram related to those in Fig. 12.1(c) and Table. 12.1. The number on top of each structure corresponds to the number in Fig. 12.1 and the index in Table. 12.1. The green, purple and red balls indicate the Si atoms bonding to two, three and five other Si atoms. The blue balls are the Si atoms in the bottom two fixed layers regarding as bulk silicon. The pink balls are the hydrogen atom terminating the dangling bond for the bottom Si layer. The grey balls are the adsorbed H atoms.

12.3. Order-disorder phase transition temperature and pressure

The order to disorder phase transition T, p_{H_2} condition can be evaluated by just another post-processing of the REGC results via MBAR. The heat capacity C_v at each T, p condition is evaluated using the same equation as in the LJ surface:

$$C_{v,\,(T,\,p_{\mathrm{H}_2})} = \frac{\langle E^2 \rangle_{(T,\,p_{\mathrm{H}_2})} - \langle E \rangle^2_{(T,\,p_{\mathrm{H}_2})}}{k_B T^2} \tag{12.1}$$

In the equation, the expectations of E^2 and E are estimated at each specific $(T,\,p_{\mathrm{H}_2})$ condition. Before discussion of the order-disorder phase transition condition, N_{H} is defined to denote that the phase includes N_{H} chemically adsorbed H atoms. At pressure of 10^{-20} atm, there is no peak of the heat capacity with the temperature ranging from 300 to 1000 K. At 10^{-15} atm, an obvious peak around 343 K indicates the transition from $N_{\mathrm{H}} = 2$ to $N_{\mathrm{H}} = 4$. There is a plateau here, but no explicit peak. At 10^{-10} atm, the transition from $N_{\mathrm{H}} = 2$ to $N_{\mathrm{H}} = 4$ shift to 412 K. The peak around 449 K is the transition from bare surface to $N_{\mathrm{H}} = 1$. The peak around 345 K is the transition from $N_{\mathrm{H}} = 4$ to $N_{\mathrm{H}} = 8$ while the peak around 310 K is the transition from $N_{\mathrm{H}} = 9$ to $N_{\mathrm{H}} = 10$. At 10^{-5} atm, all the transitions mentioned above shift to higher temperature, and another peak aournd 320 K is the transition from $N_{\mathrm{H}} = 10$ to $N_{\mathrm{H}} = 12$. At 1 atm, the C_v peaks at 696 K, 523 K and 383 K are the transition temperatures from $N_{\mathrm{H}} = 2$ to $N_{\mathrm{H}} = 4$, from $N_{\mathrm{H}} = 4$ to $N_{\mathrm{H}} = 8$, and from $N_{\mathrm{H}} = 10$ to $N_{\mathrm{H}} = 12$, respectively. At 10^5 atm, the C_v peaks at 759 K and 512 K are the transition temperatures from $N_{\mathrm{H}} = 7$ to $N_{\mathrm{H}} = 10$, and from $N_{\mathrm{H}} = 10$ to $N_{\mathrm{H}} = 11$, respectively.

The estimation of phase boundary is straightforward since the phase transition condition can be obtained as described above. As shown in the fig. 12.5, the blue, red, cyan and black lines indicate the phase boundaries between bare surface and $N_{\mathrm{H}} = 1$, between $N_{\mathrm{H}} = 2$ and $N_{\mathrm{H}} = 4$, between $N_{\mathrm{H}} = 4$ and $N_{\mathrm{H}} = 8$, and between $N_{\mathrm{H}} = 10$ and $N_{\mathrm{H}} = 12$, respectively. The average number of H atoms $\langle N_{\mathrm{H}} \rangle$ is calculated as a function of temperature at constant pressures, that is, $p_{\mathrm{H}_2} = 10^{-20}$, 10^{-15}, 10^{-10}, 10^{-5}, 1, and 10^5 atm. The yellow dot at the end of blue/red/cyan line is the critical point. The critical point is estimated to be at T, p_{H_2} point where the C_v peak disappears. For instance, as shown in Fig. 12.5(b), at 1 atm, there is a step from $\langle N_{\mathrm{H}} \rangle = 0$ to $\langle N_{\mathrm{H}} \rangle = 1$ at $T = 984$ K. However, at 1 atm, the corresponding C_v peak disappears. Therefore, the

critical point for blue like is at around $T = 984$ K and $p_{H_2} = 1$ atm. The C_v peaks for from $N_H = 2$ to $N_H = 4$ and from $N_H = 4$ to $N_H = 8$ are present at 1 atm but disappear at $p_{H_2} = 10^5$ atm. Therefore, the critical points are at 1 atm $< p_{H_2} < 10^5$ atm while $T > 696$ K and $T > 523$ K, respectively.
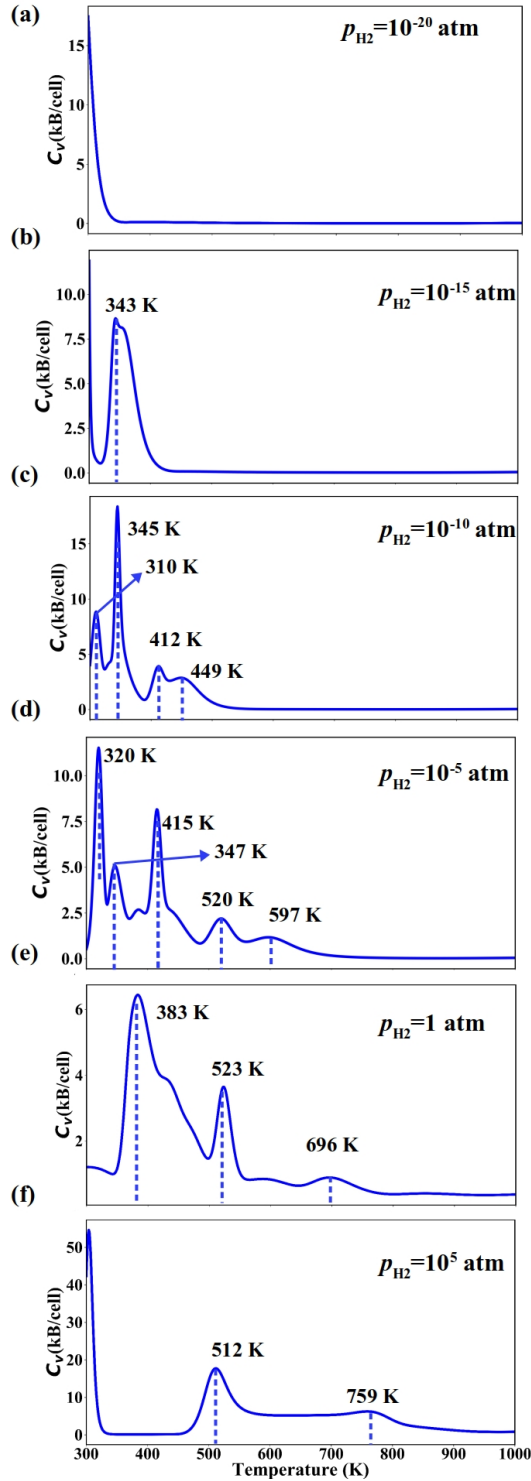
Figure 12.4.: The heat specific C_v of adsorbates vs. T at constant pressures, that is, $p_{H_2} = 10^{-20}$, 10^{-15}, 10^{-10}, 10^{-5}, 1, and 10^5 atm. The blue dash lines denote the peaks of heat specific indicating the phase transitions.
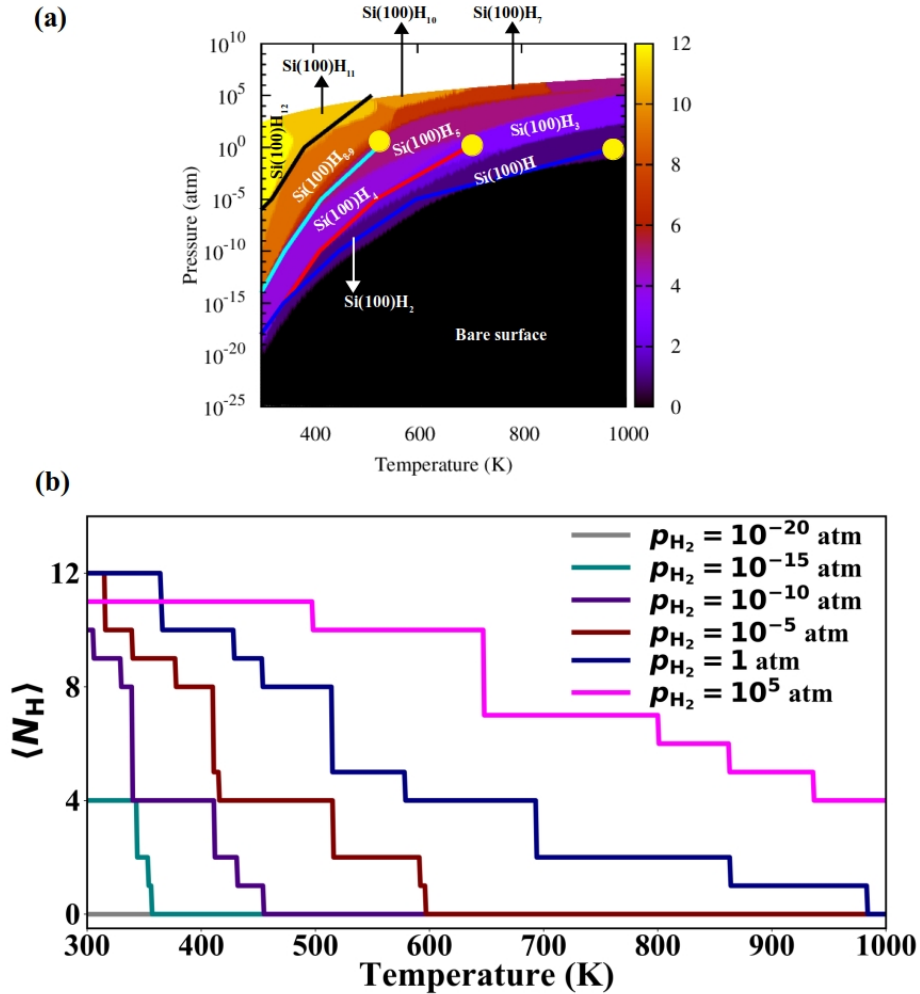
Figure 12.5.: (a) Phase diagram of the number of chemically adsorbed H atoms on the Si(100) surface. The blue line denotes the phase boundary between bare surface and $N_H = 1$. The red line denotes the phase boundary between $N_H = 2$ and $N_H = 4$. The cyan line indicates the phase boundary between $N_H = 4$ and $N_H = 8$. The black line indicates the boundary between the $N_H = 10$ phase and the $N_H = 12$ phase. (b) The average number of hydrogen atom $\langle N_H \rangle$ as a function of temperature at constant pressures, that is, $p_{H_2} = 10^{-20}$, 10^{-15}, 10^{-10}, 10^{-5}, 1, and 10^5 atm. The yellow dots are the estimated critical points.

12.4. Open questions

To end the analysis of the structures, two important obervations should be made. Firstly, the structures listed in Fig. 12.3 are just "representative" configurations having the same coordination histogram. This means that for the same coordination histogram, there is not only one specific structure corresponding to it, but several. For instance, twenty-seven configurations share the same coordination histogram of $[0, 3, 6, 0, 0, 0, 0, 0]$. Two representative structures are selected and illustrated in Fig. 12.6.In other words, the coordination histogram we choose to distinguish the different surfaces structures is not the unique representation of each $Si(100)$-H_N surfaces configurations. This motivates us to find a more refined *fingerprint* to distinguish among inequivalent structures. Probably, the radial distribution function is a good choice. However, the radial distribution function implies little information when surfaces undergo the reconstructions like $Si(100)$ e.g., the dimer up and down since the radial distribution function contains only radial information, but no information about the angular distribution of the atoms.
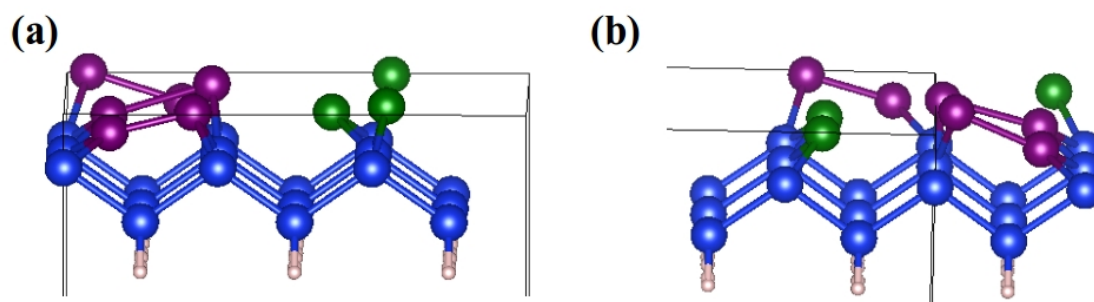
Figure 12.6.: Two selected representative $Si(100)$ configurations share the coordination histogram $[0, 3, 6, 0, 0, 0, 0, 0]$.

Secondly, so far, all the useful information obtained are quite straightforward from REGC sampling coupled with post-processing by MBAR. We know that for a specific (T, p) condition, what is the stable phase, its structural information (at least, the representative one) and its any electronic properties. But the physical mechanism behind any phase transition is unclear. For instance, why, for the same value of N, are there different configurations stable under different (T,p) regions? All these issues will be

addressed in the near future.

13. Conclusions and Outlook

13.1. Conclusions

In this thesis, the long-standing challenge of calculating complete surface phase diagrams, including anharmonic contributions and unexpected structures, is addressed by the development of Replica-Exchange Grand-Canonical Monte Carlo/*ab initio* Molecular-Dynamics (REGCMC/MD) approach.

The approach overcomes typical (but not necessary) shortcomings of the *ab initio* atomistic thermodynamics (aiAT) approach, which calculates surface phase diagrams at most at the harmonic approximation with the exception of the chemical potentials. The largely unbiased sampling of the configurational and compositional space of surfaces is achieved by taking advantage of replica exchange and grand-canonical ensemble. In particular, replica-exchange simulations improve the sampling by shuttling configurations from regions of low temperature or high chemical potential to regions of high temperature or low chemical potential to overcome the kinetic barrier. Considering the grand-canonical ensemble, thermodynamically possible defects can be effectively generated via particles' insertion or removal, thus identifying unexpected structures.

Th REGC output is post-processed via MBAR (the Bolzmann-reweighting-based estimator) to estimate the free energies and ensemble averages [29]. The REGC results are gathered and pooled together into a mixture distribution. Then MBAR reweights the samples to thermodynamic state (T_i, p_i) of interest from this mixture distribution.

The approach is demonstrated to a model surface described by Lennard-Jones force-fields. The phase diagram is constructed in two ways: The MBAR@REGC phase diagram is calculated through post-processing the REGC data by MBAR; The aiAT@REGC phase diagram is calculated by aiAT method with REGC sampling data. Both the MBAR@REGC and aiAT@REGC phase diagrams agree at very low temperature ($T <$ 350 K) and low coverage (< 1 monolayer), where the (quasi-) harmonic approximation is valid. At high temperature and high gas pressure, where anharmonic effects are dominant, however, the aiAT@REGC phase diagram provides quite different infor-

mation from MBAR@REGC phase diagram and becomes less valid. In contrast, the MBAR@REGC phase diagram shows that region of stability of higher coverages (above one monolayer) is shifted to higher temperatures and lower pressures. The driving force behind this shift is the increase of larger negative vibrational contributions due to enhanced configurational freedom, especially in the direction z perpendicular to the slab. Besides the *complete* phase diagram, the structural characteristics of adsorbate phases can also be evaluated in a statistical way. For instance, the average radial distribution functions can be evaluated at any selected thermodynamic states. The results reveal that the same phase (the same composition) exhibits the ordered characteristic at relatively low temperature and pressure ($T = 200\mathrm{K}$, $p_\mathrm{B} = 2.03 \times 10^{-17}$), but disordered nature at ($T = 600\mathrm{K}$, $p_\mathrm{B} = 8.89 \times 10^{-2}$). This information can not be obtained in the phase diagram constructed by ab initio atomistic thermodynamics since the same structure with lowest DFT energy is used for each composition for the whole temperature and pressure range. This demonstrates the capability of REGC sampling to uncover detailed thermodynamic information on the simulated system.

Coupled to *ab initio* MD, the REGC algorithm was applied to identify the thermodynamically stable and metastable compositions and structures of $\mathrm{Si}_M\mathrm{H}_N$ ($M = 2, 4$) clusters at realistic temperatures and pressure of the molecular hydrogen gas. A thermodynamically stable phase $\mathrm{Si}_2\mathrm{H}_4$ is missing in aiAT@REGC phase diagrams taking into account only harmonic effect. The similar case occurs to $\mathrm{Si}_4\mathrm{H}_4$ and $\mathrm{Si}_4\mathrm{H}_6$. When the surface is in contact with a reactive gas atmosphere, the gas atom/molecule adsorb on it in different ways: reacting with surface; just floating on top of surface without interaction. In practice, both the gas molecule and its atom are allowed to adsorb on the surface so that the configurations with dissociated molecule are accessible. The phase diagram can also be constructed in terms of an another observable, for instance, the number of adsorbed H in the system. The range of the stability of each phases also changed in this phase diagram. For instance, $\mathrm{Si}_4\mathrm{H}_4$ and $\mathrm{Si}_4\mathrm{H}_6$ have a considerably larger stable range. The thermodynamically stable structures of each cluster size appearing in the phase diagrams have been successfully identified and also many isomers reported previously are found in REGC sampling.

An extensive application of REGC method to the Si(100)-(3×3) surface in contact with H_2, modeled at the gradient-corrected DFT level, has been developed. Preliminary but promising results unveil the evolution of surface structure at the realistic T, p_{H_2} conditions. An insightful descriptor of configurations (coordination histogram) is selected as

the observable of interest to reveal detailed thermodynamic structural information evaluated via post-processing by MBAR, thereby, the most probable representative structures are identified at a given state point $(T, \mu_{\mathrm{H_2}})$ where $\mu_{\mathrm{H_2}}$ is a function of T and $p_{\mathrm{H_2}}$. The Si atoms at Si(100) surface tend to bond to the neighboring Si atoms along the [110] direction and form the Si-Si dimer row. A similar trend of reconstruction has been identified in previous experimental studies. [154, 155] Moreover, the Si(100)H$_{12}$ identified to be thermodynmically stable around 400 K is in good agreement with the experimentally reported Si(100)-(3×1) phase in Ref. [34]. More importantly, the T-p map of the electronic/physical properties of surfaces, e.g., HOMO-LUMO gap can also be constructed by the post-processing of the REGC data. These electronic-structure phase diagram reveal that the HOMO-LUMO gap increases with increasing T and $p_{\mathrm{H_2}}$ when N_{H} is even number. In other words, the electronic properties can be tuned by adjusting the realistic conditions of the reservoir surrounding the clusters/surfaces. In the future work, the finite-size effect on the reconstruction and adsorption patterns should be taken into account.
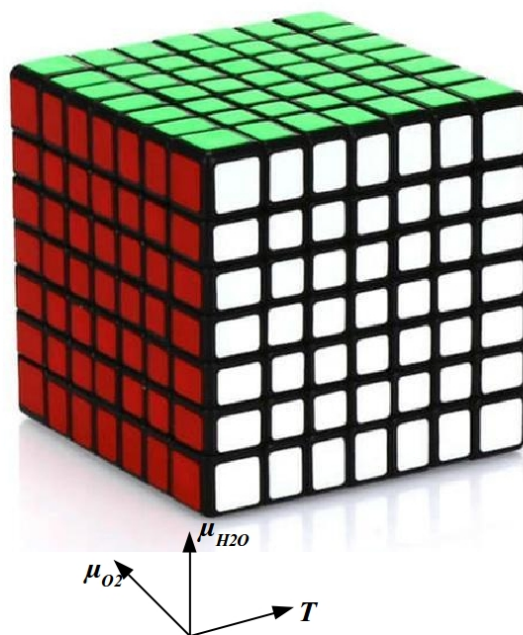
In summary, a Replica-Exchange Grand-Canonical method has been developed to successfully perform simulations on surfaces/nanoclusters in contact with reactive gas at realistic (T, p) conditions. We demonstrated how it can be used to determine (T,p) phase diagrams, in combination with the multistate-Bennet-acceptance-ratio (MBAR) reweighting approach (the Bolzmann-reweighting-based estimator). Besides free-energy (T, p) phase diagrams, the combination of the REGC sampling and *a posteriori* analysis via MBAR allows for the determination of phase diagrams for any (atom position dependent) observables, therefore indicating how to tune the environmental condition (T and p) to get a material with desired properties. This massively parallel algorithm requires no prior knowledge of the phase diagram and takes only the potential-energy function together with the desired μ and T ranges as inputs. The source code is incorporated in FHI-PANDA package [158] and free for academic use.

13.2. Outlook

The description of crystal surfaces in contact with realistic gas-phase environments is of critical importance for the manufacture and performance of advanced materials such as electronic, magnetic and optical devices, sensors, lubricants, catalysts, and coatings. Phase diagrams play the central role in describing the regions of stability and equilibria

of structurally distinct phases. The REGC method developed in this thesis performs simulations on surfaces/nanoclusters in contact with reactive (T, p) gas and determine (T, p) phase diagrams when coupled with the MBAR reweighting approach [29]. It can therefore be applied to a wide range of practical issues, e.g., dopant profiles, surface segregation, crystal growth and more. An obvious and indeed currently investigated generalization of the method is to consider more than one reactive gas in the so-called "constrained equilibrium" [12, 13](different species do not react in the gas phase, but only at the surface). For instance, the corrosion of metal surface in a humid environment (oxygen and water in the atmosphere). To model this, as required by the REGC approach, the temperature T sequence, oxygen chemical potential μ_{O_2} range, and the water chemical potential μ_{H_2O} range are required as input of REGC approach. In total, $L \times N \times M$ replicas will be selected that is, L different T, N different μ_{O_2} and M different μ_{H_2O}. As illustrated in Fig. 13.1, each little cube represents a replica in a specific $(T_l,$ $\mu_{O_2,n}$, $\mu_{H_2O,m})$ thermodynamic state, where l, n and m are the indices of T, μ_{O_2}, and μ_{H_2O}, respectively. The Rubik's Cube can be cleaved into planes parallel to the (T, μ_{O_2}) plane (the green one). At each of these planes, μ_{H_2O} is kept constant, therefore, the "collective" 2D scheme for the attempted swaps, illustrated in Fig. 5.1 is still suitable to each plane. The same strategy can also applied to the planes parallel to red or white plane. However, for the reservoir with more than two gas species, a valid thermodynamic state is referred to at least four variables. In order to avoid a dimensional explosion, an algorithm with an adaptive μ_i grid is under development. A flexible swap scheme could be to select randomly one replica and independently one neighbor to perform the attempted swap, then to repeat until no replica has an unselected neighbor.

The algorithm itself is embarrassingly parallel and in post-production allows for diverse analyses, not necessarily planned before starting the sampling. Moreover, its embarrassingly parallel nature makes the approach "towards exascale" friendly, and can be regarded as a very efficient and internally consistent high-throughput approach. Such an undertaking has its limitation in the cost of *ab initio* molecular dynamics needed for the REGC sampling. The expensive computational cost of *ab initio* molecular dynamics can be alleviated by solid-state embedding quantum and molecular mechanical (QM/MM) calculations implemented by integrating the FHI-aims package into Chemshell package. [159] The expensive quantum mechanical (QM) description is reduced to the central chemically active region. Long-range electrostatic interactions with the system remainder are accounted for on a classical level. Further implementation is needed and benefit

Figure 13.1.: Schematic illustration of the 3D Replica-Exchange Grand-Canonical scheme. Each miniature cube represent one replica at specific $(T_l, \mu_{\text{O}_2,n}, \mu_{\text{H}_2\text{O},m})$ thermodynamic state.

us to bridging the *materials gap* from simulating single-crystal surface to nanoparticle model catalysts.

Indeed, inherently parallel nature of RE breaks if the computer time cost for MD simulation of different replicas varied a lot. In particular, the self-consistent force (scf) calculations have different time length due to the different system size. Accordingly, the slowest replica (longest scf time length) makes all the other replicas wait, that is, all the other jobs are idling and waiting for the slowest one to finish, leading to the loading problem on HPC. A direct and simple solution is to divide a REGC simulation involving a large number of replicas into several REGC calculations and each each of them including a small number of replicas. For instance, for a system of interest, 128 replicas are needed and can be divided into 4 REGC simulations with each having 32 replicas, as discussed in chapter 9. Another solution can be to dynamically distribute the computational resources among replicas based on their system size. Otherwise, flexible number of time steps in MD simulation is adopted for different replicas. The last two

solutions need further development.

The surface/cluster systems studied in the thesis is one-component and the gas particles are only allowed to adsorb on top of the surface. When studying the multi-component surfaces, like GaAs under As pressure or Ga_2O_3 in contact with O_2 gas, the arsenic or oxygen atoms in the subsurface are also involved in the exchange with the gas atmosphere. However, like the grand-canonical ensemble scheme, the method does rely on a reasonable number of successful particle insertions to achieve compositional equilibrium. As a consequence,the GC ensemble method cannot be used to study phase equilibria involving very dense phase or crystalline solids/surfaces. There exists a technique that greatly facilitates the numerical study of such phase equilibria, that is, the so-called "semi-grand canonical (sGC) ensemble method". [160] In the sGC ensemble, temperature, pressure, and the total number of molecules are fixed. During a sGC simulation, particles are allowed to change their species identity, keeping the total number of molecules fixed. Based on the particle interchanges, the sGC method works while the GC scheme fails in inserting particles in a crystalline solid/surface. Therefore, a very imperative further implementation of semi-grand canonical MC will be realized in the future release of the FHI-PANDA package. [158]

The ultimate goal of theoretical heterogeneous or computational material science is to lead the design of desired material e.g., catalysts, semiconductors, and topological insulators, not just to agree with the experimental findings. Correspondingly, computational initiatives [161–164] have already handled many thousands of different systems. Due to the wealth of calculated data increase exponentially with time, artificial-intelligence (AI) or (big-)data analytics are needed finding the underlying physical mechanisms in terms of a set of physically meaningful descriptors invisible to the human eye. Thus, it may lead to accelerate discoveries of new materials or phenomena.

Plenty of data including configurations, their corresponding forces, velocities and physical properties are generated in a REGC simulation. So far, we only make use of a tiny fraction of the data to construct phase diagrams with respect to any observable dependent of atom position with the help of MBAR. Large portion of the data are so far inefficiently exploited. Novel big-data analytics tools, e.g., based on machine learning [165–169] or compressed sensing (CS) [170–173], promise to do so. Moreover, due to the complexity of the data generated by REGC, further development of AI tools is necessary when analyzing the REGC results or even unveiling the actuating mechanism behind the phase diagrams.

A. Appendix

A.1. Lennard-Jones surface

Figure A.1.: Equation of state of the Lennard-Jones fluid; isotherm at $T = 2.0$. The solid line is the equation of state of Johnson et al. [138] and the squares are the results from our grand-canonical simulations. The dotted line is the excess chemical potential as calculated from the equation of state of Johnson et al in Ref. [174] and the circles are the results of our simulations. All variables are in reduced units. The translation of reduced units to real units for Lennard-Jones argon are the same in Ref. [46]

A.2. Silicon clusters and surfaces at *ab initio* level

Figure A.4.: Phase diagrams of chemical adsorption of H_2 on Si_2 cluster (a), vertical electronic affinity (VEA) (b) and vertical ionization potential (VIP) (c) of Si_2H_N at reactive gas phase, respectively. Phase diagrams of chemisorbed Si_4H_N (a), vertical electronic affinity (VEA) (b) and vertical ionization potential (VIP) (c) of Si_4H_N at reactive gas phase, respectively. The scale of panels (a) and (d) is the number of chemically adsorbed H atoms. VEA and VIP in panels (b), (c), (e) and (f) are in eV.

Figure A.6.: Distribution of adsorption energy $(E_{\mathrm{Si_4H}_N} - N/2E_{\mathrm{H_2}})$ of each thermodynamical state in the REGCMD simulation for $\mathrm{Si_4}$. Each trajectory is divided into three same interval (2000 REGCMD steps). The distribution is calculated at every interval for each trajectory. The blue, orange and green bars indicate the energy distribution of first, second and third interval of each trajectory, respectively.

Figure A.7.: The diffusion probability of each thermodynamical state in each configuration (replica) in the REGCMD simulation for $\mathrm{Si_4}$; Inset on the bottom right: the standard deviation of each state.

Figure A.8.: Molecular dynamics pseudo-Hamiltonian H in stochastic velocity rescaling thermostat [144] as a function of AIMD time step. Upper panel is $\mathrm{H_2}$ molecule; the other is $\mathrm{D_2}$ molecule Black: time step of 1 fs. Red: time step of 2 fs. Red: time step of 3 fs. The pseudo-Hamiltonian is kept constant for $\mathrm{H_2}$ system when time step is 1fs. The pseudo-Hamiltonian is kept constant for $\mathrm{H_2}$ system when time step is 1fs or 2fs.

Figure A.9.: The $\mathrm{H_2}$ gas density in the $\mathrm{Si_2H_{20}}$ phase at ($T = 500$ K and $p_{\mathrm{H2}} = 2.3 \times 10^4$ atm). A sphere is defined as following: the center of mass for $\mathrm{Si_2H_{20}}$ phase is the center of every sphere, and the radius increases every 1 Å. The $\mathrm{H_2}$ gas density is calculated by counting the number of H atoms per Å^{-3}. The dash line denote the density of ideal (ρ_{ideal}) $\mathrm{H_2}$ gas at ($T = 500$ K and $p_{\mathrm{H2}} = 2.3 \times 10^4$ atm) condition. For the ideal gas, $\rho_{\mathrm{ideal}} = \beta \times p_{\mathrm{H2}}$. [46]

Figure A.10.: Convergence of relative stability of isomers of Si_4H_N at DFT-PBE level. The "light", "tight", and "really-tight" labels correspond to the three default levels for the basis set size and numerical settings in the FHI-aims program package.
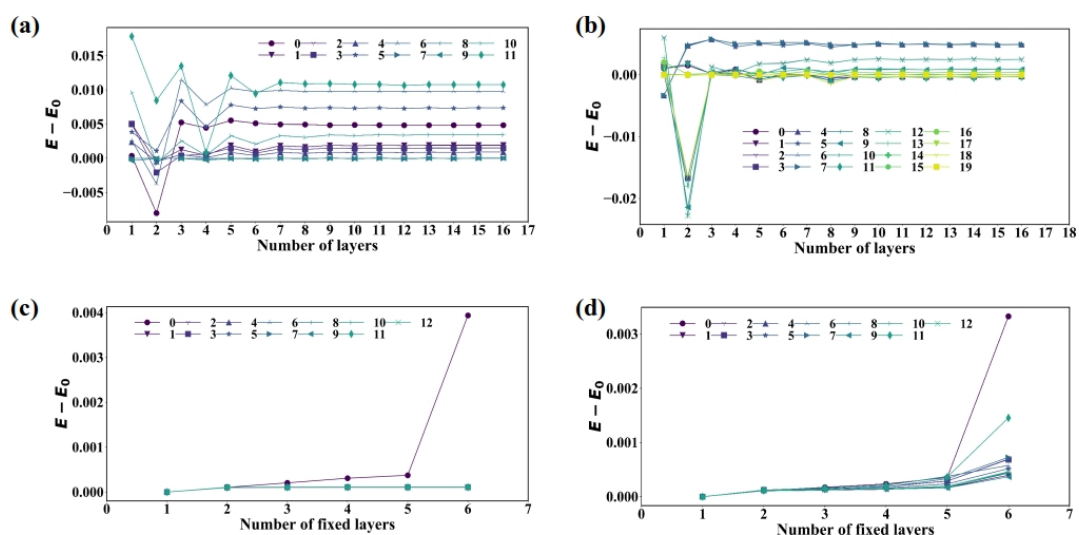

Figure A.11.: (a) Relative stability of surface energy per area (eV) as a function of number of layers. 12 different Si(100) structures. (b) Relative stability of surface energy per area (eV) of adsorbed structures as a function of number of layers. 20 different Si(100) with one H adsorbed structures. (c) Relative stability of surface energy per area (eV) as a function of fixed number of layers. 13 different Si(100) structures. (d) Relative stability of surface energy per area (eV) of adsorbed structures as a function of fixed number of layers. 13 different Si(100) with one H adsorbed structures.
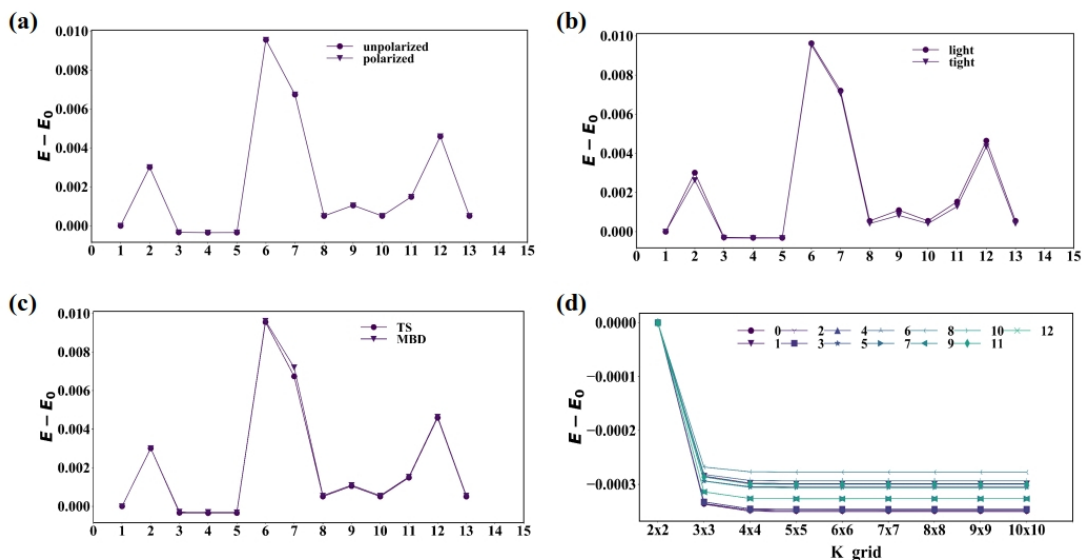
Figure A.12.: (a) Relative stability of 13 different Si(100) surface structures with light and tight basis functions. (b) *k*-grid convergence test for 13 different Si(100) surface structures.
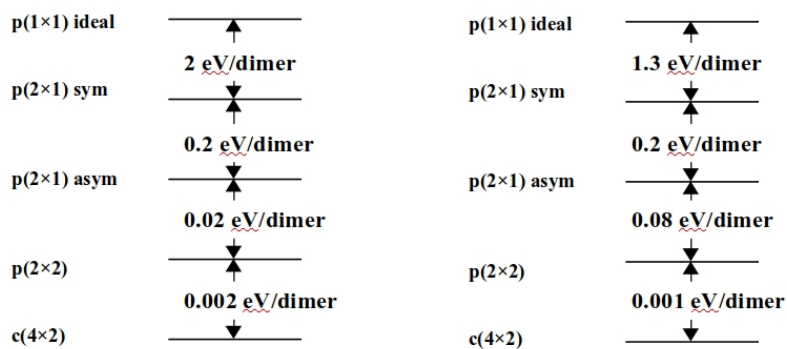
Figure A.13.: Energy differences between different reconstructions of Si(100) calculated in Ref. [175] (left panel) and by the our DFT settings (right panel).

103

Acknowledgements

It would not have been possible to pursue my PhD career without the support and guidance that I received from many people.

First and foremost, I would like to express my sincere gratitude to my supervisor Matthias Scheffler for providing me the chance to conduct my PhD career. I do appreciate him creating such an ideal academic atmosphere. Here I got plenty of opportunities to discuss with great scientists and exchange ideas with great minds, which I have never imaged before. Thank you for the continuous support of my PhD study, especially wise advices on my research and insightful comments on my paper.

Then, I want to give my great thanks to Luca M. Ghiringhelli. As my direct supervisor during the last four years, he has been giving me countless support: the stimulating discussions on this work or sometimes beyond it, critical reading on proposal, abstracts, paper and this thesis. Without his guidance and constant feedback this PhD would not have been achievable. I could not think of a better advisor for my PhD study. I'm pretty sure that Luca and I will stay in contact and collaborate together to solve many other scientific puzzles for the coming many years.

My deep appreciation goes out to Chunye Zhu. The numerous discussions I had with him are always enlightening and resulted in the insightful ideas in the work here. A big thank to Bryan R. Goldsmith who was always so helpful and provided me with his assistance in the initial stage of this work. I'm especially grateful to Fawzi Mohamed for the helpful support of the parallel scheme of our code. I greatly appreciate Sergey Levchenko and Ruihai Ouyang for the sharing of their expertise in heterogenous catalysis and big-data analytics. A special thank to Igor Ying Zhang for the useful guidance and advice in the initial stage of my PhD career.

I also want to thank my wonderful colleagues. The first one, my officemate, Florian Knoop, with whom I have shared the office T1.07 for almost three years. Great thanks to him for the interesting scientific discussion, invaluable feedback on the work, especially my presentation, and critical reading many parts of the thesis. Also thank my former officemates, Susmita Basak and Sebastián Alarcón Villaseca, for the wonderful time

Bibliography

[1] G. Somorjai and J. Park, "Molecular factors of catalytic selectivity," *Angewandte Chemie International Edition*, vol. 47, no. 48, pp. 9212–9228, 2008.

[2] C. Stampfl, M. V. Ganduglia-Pirovano, K. Reuter, and M. Scheffler, "Catalysis and corrosion: the theoretical surface-science context," *Surface Science*, vol. 500, no. 1, pp. 368 – 394, 2002.

[3] H.-R. Volpp and J. Wolfrum, "Sum-frequency generation (sfg) vibrational spectroscopy as a means for the investigation of catalytic combustion," *Applied combustion diagnostics*, 2002.

[4] G. A. Somorjai, A. M. Contreras, M. Montano, and R. M. Rioux, "Clusters, surfaces, and catalysis," *Proceedings of the National Academy of Sciences*, vol. 103, no. 28, pp. 10577–10583, 2006.

[5] M. Salmeron and R. Schlögl, "Ambient pressure photoelectron spectroscopy: A new tool for surface science and nanotechnology," *Surface Science Reports*, vol. 63, no. 4, pp. 169 – 199, 2008.

[6] H. Bluhm, M. Hävecker, A. Knop-Gericke, M. Kiskinova, R. Schlögl, and M. Salmeron, "In situ x-ray photoelectron spectroscopy studies of gas-solid interfaces at near-ambient conditions," *MRS Bulletin*, vol. 32, no. 12, p. 1022–1030, 2007.

[7] B. J. McIntyre, M. B. Salmeron, and G. A. Somorjai, "A scanning tunneling microscope that operates at high pressures and high temperatures (430 k) and during catalytic reactions," *Catalysis Letters*, vol. 14, pp. 263–269, Sep 1992.

[8] F. Tao, D. Tang, M. Salmeron, and G. A. Somorjai, "A new scanning tunneling microscope reactor used for high-pressure and high-temperature catalysis studies," *Review of Scientific Instruments*, vol. 79, no. 8, p. 084101, 2008.

[9] C. Weinert and M. Scheffler, "Chalcogen and vacancy pairs in silicon: Electronic structure and stabilities," in *Materials Science Forum*, vol. 10, pp. 25–30, Trans Tech Publ, 1986.

[10] M. Scheffler, "Thermodynamic aspects of bulk and surface defects–first-principle calculations -," in *Physics of Solid Surfaces 1987* (J. Koukal, ed.), vol. 40 of *Studies in Surface Science and Catalysis*, pp. 115 – 122, Elsevier, 1988.

[11] K. Reuter and M. Scheffler, "Composition, structure, and stability of $ruo_2(110)$ as a function of oxygen pressure," *Phys. Rev. B*, vol. 65, p. 035406, Dec 2001.

[12] K. Reuter and M. Scheffler, "Composition and structure of the $ruo_2(110)$ surface in an o_2 and co environment: Implications for the catalytic formation of co_2," *Phys. Rev. B*, vol. 68, p. 045407, Jul 2003.

[13] K. Reuter and M. Scheffler, "First-principles atomistic thermodynamics for oxidation catalysis: Surface phase diagrams and catalytically interesting regions," *Phys. Rev. Lett.*, vol. 90, p. 046103, Jan 2003.

[14] E. Kaxiras, Y. Bar-Yam, J. D. Joannopoulos, and K. C. Pandey, "Ab initio theory of polar semiconductor surfaces. i. methodology and the (22) reconstructions of gaas(111)," *Phys. Rev. B*, vol. 35, pp. 9625–9635, Jun 1987.

[15] G.-X. Qian, R. M. Martin, and D. J. Chadi, "First-principles study of the atomic reconstructions and energies of ga- and as-stabilized gaas(100) surfaces," *Phys. Rev. B*, vol. 38, pp. 7649–7663, Oct 1988.

[16] N. Moll, M. Scheffler, and E. Pehlke, "Influence of surface stress on the equilibrium shape of strained quantum dots," *Phys. Rev. B*, vol. 58, pp. 4566–4571, Aug 1998.

[17] E. C. Beret, M. M. van Wijk, and L. M. Ghiringhelli, "Reaction cycles and poisoning in catalysis by gold clusters: A thermodynamics approach," *International Journal of Quantum Chemistry*, vol. 114, no. 1, pp. 57–65, 2014.

[18] S. Bhattacharya, S. V. Levchenko, L. M. Ghiringhelli, and M. Scheffler, "Stability and metastability of clusters in a reactive atmosphere: Theoretical evidence for unexpected stoichiometries of $mg_M\mathbf{o}_x$," *Phys. Rev. Lett.*, vol. 111, p. 135501, Sep 2013.

[19] S. Bhattacharya, S. V. Levchenko, L. M. Ghiringhelli, and M. Scheffler, "Efficient ab initio schemes for finding thermodynamically stable and metastable atomic structures: benchmark of cascade genetic algorithms," *New Journal of Physics*, vol. 16, no. 12, p. 123016, 2014.

[20] D. A. McQuarrie, *Statistical mechanics / Donald A. McQuarrie.* Harper Row New York, 1975.

[21] H. A. Jahn, E. Teller, and F. G. Donnan, "Stability of polyatomic molecules in degenerate electronic states - i—orbital degeneracy," *Proceedings of the Royal Society of London. Series A - Mathematical and Physical Sciences*, vol. 161, no. 905, pp. 220–235, 1937.

[22] D. S. Kim, O. Hellman, J. Herriman, H. L. Smith, J. Y. Y. Lin, N. Shulumba, J. L. Niedziela, C. W. Li, D. L. Abernathy, and B. Fultz, "Nuclear quantum effect with pure anharmonicity and the anomalous thermal expansion of silicon," *Proceedings of the National Academy of Sciences*, vol. 115, no. 9, pp. 1992–1997, 2018.

[23] R. H. Swendsen and J.-S. Wang, "Replica monte carlo simulation of spin-glasses," *Phys. Rev. Lett.*, vol. 57, pp. 2607–2609, Nov 1986.

[24] E. Marinari and G. Parisi, "Simulated tempering: A new monte carlo scheme," *EPL (Europhysics Letters)*, vol. 19, no. 6, p. 451, 1992.

[25] C. J. Geyer and E. A. Thompson, "Annealing markov chain monte carlo with applications to ancestral inference," *Journal of the American Statistical Association*, vol. 90, no. 431, pp. 909–920, 1995.

[26] Y. Sugita and Y. Okamoto, "Replica-exchange molecular dynamics method for protein folding," *Chemical Physics Letters*, vol. 314, no. 1, pp. 141 – 151, 1999.

[27] Q. Yan and J. J. de Pablo, "Hyper-parallel tempering monte carlo: Application to the lennard-jones fluid and the restricted primitive model," *The Journal of Chemical Physics*, vol. 111, no. 21, pp. 9509–9516, 1999.

[28] R. Faller, Q. Yan, and J. J. de Pablo, "Multicanonical parallel tempering," *The Journal of Chemical Physics*, vol. 116, no. 13, pp. 5419–5423, 2002.

[29] M. R. Shirts and J. D. Chodera, "Statistically optimal analysis of samples from multiple equilibrium states," *The Journal of Chemical Physics*, vol. 129, no. 12, p. 124105, 2008.

[30] J. P. Perdew, K. Burke, and M. Ernzerhof, "Generalized gradient approximation made simple [phys. rev. lett. 77, 3865 (1996)]," *Phys. Rev. Lett.*, vol. 78, pp. 1396–1396, Feb 1997.

[31] D. Balamurugan and R. Prasad, "Effect of hydrogen on ground-state structures of small silicon clusters," *Phys. Rev. B*, vol. 64, p. 205406, Oct 2001.

[32] E. Srinivasan, H. Yang, and G. N. Parsons, "Ab initio calculation of hydrogen abstraction energetics from silicon hydrides," *The Journal of Chemical Physics*, vol. 105, no. 13, pp. 5467–5471, 1996.

[33] M. Springborg, "Electronic properties of polymeric silicon hydrides," *Phys. Rev. B*, vol. 40, pp. 7839–7851, Oct 1989.

[34] Y. J. Chabal and K. Raghavachari, "New ordered structure for the h-saturated si(100) surface: The (3×1) phase," *Phys. Rev. Lett.*, vol. 54, pp. 1055–1058, Mar 1985.

[35] D. D. Frantz, D. L. Freeman, and J. D. Doll, "Reducing quasi-ergodic behavior in monte carlo simulations by j-walking: Applications to atomic clusters," *The Journal of Chemical Physics*, vol. 93, no. 4, pp. 2769–2784, 1990.

[36] W. Ortiz, A. Perlloni, and G. E. López, "Extending the j-walking monte carlo algorithm to the isothermal–isobaric ensemble: solid–liquid equilibrium in clusters," *Chemical Physics Letters*, vol. 298, no. 1, pp. 66 – 70, 1998.

[37] B. A. Berg and T. Neuhaus, "Multicanonical algorithms for first order phase transitions," *Physics Letters B*, vol. 267, no. 2, pp. 249 – 253, 1991.

[38] B. A. Berg and T. Neuhaus, "Multicanonical ensemble: A new approach to simulate first-order phase transitions," *Phys. Rev. Lett.*, vol. 68, pp. 9–12, Jan 1992.

[39] R. J. N. Baldock, L. B. Pártay, A. P. Bartók, M. C. Payne, and G. Csányi, "Determining pressure-temperature phase diagrams of materials," *Phys. Rev. B*, vol. 93, p. 174108, May 2016.

[40] A. P. Lyubartsev, A. A. Martsinovski, S. V. Shevkunov, and P. N. Vorontsov-Velyaminov, "New approach to monte carlo calculation of the free energy: Method of expanded ensembles," *The Journal of Chemical Physics*, vol. 96, no. 3, pp. 1776–1783, 1992.

[41] B. Hesselbo and R. B. Stinchcombe, "Monte carlo simulation and global optimization without parameters," *Phys. Rev. Lett.*, vol. 74, pp. 2151–2155, Mar 1995.

[42] F. Wang and D. P. Landau, "Efficient, multiple-range random walk algorithm to calculate the density of states," *Phys. Rev. Lett.*, vol. 86, pp. 2050–2053, Mar 2001.

[43] F. A. Escobedo and J. J. de Pablo, "Expanded grand canonical and gibbs ensemble monte carlo simulation of polymers," *The Journal of Chemical Physics*, vol. 105, no. 10, pp. 4391–4394, 1996.

[44] S. Bhattacharya, S. V. Levchenko, L. M. Ghiringhelli, and M. Scheffler, "Efficient ab initio schemes for finding thermodynamically stable and metastable atomic structures: Benchmark of cascade genetic algorithms," *New Journal of Physics*, vol. 16, no. 12, p. 123016, 2014.

[45] D. McQuarrie, *Statistical Mechanics*. University Science Books, 2000.

[46] D. Frenkel and B. Smit, *Understanding molecular simulation: From algorithms to applications*. Elsevier, 2002.

[47] A. Laio and M. Parrinello, "Escaping free-energy minima," *Proceedings of the National Academy of Sciences*, vol. 99, no. 20, pp. 12562–12566, 2002.

[48] M. Iannuzzi, A. Laio, and M. Parrinello, "Efficient exploration of reactive potential energy surfaces using car-parrinello molecular dynamics," *Phys. Rev. Lett.*, vol. 90, p. 238302, Jun 2003.

[49] G. M. Torrie and J. P. Valleau, "Monte Carlo free energy estimates using non-Boltzmann sampling: Application to the sub-critical Lennard-Jones fluid," *Chemical Physics Letters*, vol. 28, no. 4, pp. 578–581, 1974.

[50] G. M. Torrie and J. P. Valleau, "Nonphysical sampling distributions in Monte Carlo free-energy estimation: Umbrella sampling," *Journal of Computational Physics*, vol. 23, no. 2, pp. 187–199, 1977.

[51] D. Hamelberg, J. Mongan, and J. A. McCammon, "Accelerated molecular dynamics: A promising and efficient simulation method for biomolecules," *The Journal of Chemical Physics*, vol. 120, no. 24, pp. 11919–11929, 2004.

[52] D. Hamelberg and J. A. McCammon, "Fast Peptidyl cis−trans Isomerization within the Flexible Gly-Rich Flaps of HIV-1 Protease," *Journal of the American Chemical Society*, vol. 127, no. 40, pp. 13778–13779, 2005.

[53] D. Hamelberg, T. Shen, and J. Andrew McCammon, "Relating kinetic rates and local energetic roughness by accelerated molecular-dynamics simulations," *The Journal of Chemical Physics*, vol. 122, no. 24, p. 241103, 2005.

[54] A. Mitsutake, "Simulated-tempering replica-exchange method for the multidimensional version," *The Journal of Chemical Physics*, vol. 131, no. 9, p. 94105, 2009.

[55] U. H. E. Hansmann, "Parallel tempering algorithm for conformational studies of biological molecules," *Chemical Physics Letters*, vol. 281, no. 1, pp. 140–150, 1997.

[56] Y. Sugita, A. Kitao, and Y. Okamoto, "Multidimensional replica-exchange method for free-energy calculations," *The Journal of Chemical Physics*, vol. 113, no. 15, pp. 6042–6051, 2000.

[57] D. J. Earl and M. W. Deem, "Parallel tempering: Theory, applications, and new perspectives," *Phys. Chem. Chem. Phys.*, vol. 7, pp. 3910–3916, 2005.

[58] A. Laio, A. Rodriguez-Fortea, F. L. Gervasio, M. Ceccarelli, and M. Parrinello, "Assessing the accuracy of metadynamics," *The Journal of Physical Chemistry B*, vol. 109, no. 14, pp. 6714–6721, 2005. PMID: 16851755.

[59] F. L. Gervasio, A. Laio, and M. Parrinello, "Flexible docking in solution using metadynamics," *Journal of the American Chemical Society*, vol. 127, no. 8, pp. 2600–2607, 2005. PMID: 15725015.

[60] R. H. Swendsen and J.-S. Wang, "Replica monte carlo simulation of spin-glasses," *Physical review letters*, vol. 57, no. 21, p. 2607, 1986.

[61] C. J. Geyer, "Markov chain monte carlo maximum likelihood," 1991.

[62] Y. Sugita and Y. Okamoto, "Replica-exchange molecular dynamics method for protein folding," *Chemical physics letters*, vol. 314, no. 1-2, pp. 141–151, 1999.

[63] C.-Y. Lin, C.-K. Hu, and U. H. Hansmann, "Parallel tempering simulations of hp-36," *Proteins: Structure, Function, and Bioinformatics*, vol. 52, no. 3, pp. 436–445, 2003.

[64] A. Schug, T. Herges, A. Verma, and W. Wenzel, "Investigation of the parallel tempering method for protein folding," *Journal of Physics: Condensed Matter*, vol. 17, no. 18, p. S1641, 2005.

[65] H.-H. G. Tsai, M. Reches, C.-J. Tsai, K. Gunasekaran, E. Gazit, and R. Nussinov, "Energy landscape of amyloidogenic peptide oligomerization by parallel-tempering molecular dynamics simulation: significant role of asn ladder," *Proceedings of the National Academy of Sciences*, vol. 102, no. 23, pp. 8174–8179, 2005.

[66] M. Habeck, M. Nilges, and W. Rieping, "Replica-exchange monte carlo scheme for bayesian data analysis," *Phys. Rev. Lett.*, vol. 94, p. 018105, Jan 2005.

[67] M. Falcioni and M. W. Deem, "A biased monte carlo scheme for zeolite structure solution," *The Journal of chemical physics*, vol. 110, no. 3, pp. 1754–1766, 1999.

[68] A. de Candia and A. Coniglio, "Spin and density overlaps in the frustrated ising lattice gas," *Physical Review E*, vol. 65, no. 1, p. 016132, 2001.

[69] R. G. Melko, "Simulations of quantum xxz models on two-dimensional frustrated lattices," *Journal of Physics: Condensed Matter*, vol. 19, no. 14, p. 145203, 2007.

[70] V. I. Manousiouthakis and M. W. Deem, "Strict detailed balance is unnecessary in monte carlo simulation," *The Journal of chemical physics*, vol. 110, no. 6, pp. 2753–2756, 1999.

[71] D. A. Kofke, "On the acceptance probability of replica-exchange monte carlo trials," *The Journal of Chemical Physics*, vol. 117, no. 15, pp. 6911–6914, 2002.

[72] D. A. Kofke, "On the acceptance probability of replica-exchange monte carlo trials," *The Journal of chemical physics*, vol. 117, no. 15, pp. 6911–6914, 2002.

[73] D. A. Kofke, "Erratum: "on the acceptance probability of replica-exchange monte carlo trials" [j. chem. phys. 117, 6911 (2002)]," *The Journal of chemical physics*, vol. 120, no. 22, pp. 10852–10852, 2004.

[74] C. Predescu, M. Predescu, and C. V. Ciobanu, "The incomplete beta function law for parallel tempering sampling of classical canonical systems," *The Journal of Chemical Physics*, vol. 120, no. 9, pp. 4119–4128, 2004.

[75] K. Y. Sanbonmatsu and A. E. García, "Structure of met-enkephalin in explicit aqueous solution using replica exchange molecular dynamics," *Proteins: Structure, Function, and Bioinformatics*, vol. 46, no. 2, pp. 225–234, 2002.

[76] N. Rathore, M. Chopra, and J. J. de Pablo, "Optimal allocation of replicas in parallel tempering simulations," *The Journal of Chemical Physics*, vol. 122, no. 2, p. 024111, 2005.

[77] R. Car and M. Parrinello, "Unified approach for molecular dynamics and density-functional theory," *Phys. Rev. Lett.*, vol. 55, pp. 2471–2474, Nov 1985.

[78] H. H, "Zur rolle der kinetischen elektronenenergie f{"ur die zwischenatomaren kr{"afte," *Zeitschrift fuer Physik*, vol. 85, pp. 180–190, 1933.

[79] R. P. Feynman, "Forces in molecules," *Phys. Rev.*, vol. 56, pp. 340–343, Aug 1939.

[80] L. Verlet, "Computer "experiments" on classical fluids. i. thermodynamical properties of lennard-jones molecules," *Phys. Rev.*, vol. 159, pp. 98–103, Jul 1967.

[81] S. Nosé, "A unified formulation of the constant temperature molecular dynamics methods," *The Journal of Chemical Physics*, vol. 81, no. 1, pp. 511–519, 1984.

[82] T. Schneider and E. Stoll, "Molecular-dynamics study of a three-dimensional one-component model for distortive phase transitions," *Phys. Rev. B*, vol. 17, pp. 1302–1322, Feb 1978.

[83] W. G. Hoover, "Canonical dynamics: Equilibrium phase-space distributions," *Phys. Rev. A*, vol. 31, pp. 1695–1697, Mar 1985.

[84] G. Bussi, D. Donadio, and M. Parrinello, "Canonical sampling through velocity rescaling," *The Journal of chemical physics*, vol. 126, no. 1, p. 014101, 2007.

[85] J. Kolafa, "Numerical integration of equations of motion with a self-consistent field given by an implicit equation," *Molecular Simulation*, vol. 18, no. 3, pp. 193–212, 1996.

[86] V. Blum, R. Gehrke, F. Hanke, P. Havu, V. Havu, X. Ren, K. Reuter, and M. Scheffler, "Ab initio molecular simulations with numeric atom-centered orbitals," *Computer Physics Communications*, vol. 180, no. 11, pp. 2175 – 2196, 2009.

[87] J. E. Lennard-Jones, "Cohesion," *Proceedings of the Physical Society*, vol. 43, pp. 461–482, sep 1931.

[88] C. Y. H. Jiang, "A new approach to model adsorption in heterogeneous phase system with monte carlo method," *American Journal of Materials Science*, vol. 4, pp. 25–38, 2014.

[89] A. C. T. van Duin, S. Dasgupta, F. Lorant, and W. A. Goddard, "ReaxFF: A Reactive Force Field for Hydrocarbons," *The Journal of Physical Chemistry A*, vol. 105, no. 41, pp. 9396–9409, 2001.

[90] M. F. Russo and A. C. T. van Duin, "Atomistic-scale simulations of chemical reactions: Bridging from quantum chemistry to engineering," *Nuclear Instruments and Methods in Physics Research Section B: Beam Interactions with Materials and Atoms*, vol. 269, no. 14, pp. 1549–1554, 2011.

[91] T. P. Senftle, T. P. Senftle, M. M. Islam, S. B. Kylasa, Y. Zheng, Y. K. Shin, C. Junkermeier, R. Engel-Herbert, M. J. Janik, H. M. Aktulga, T. Verstraelen, A. Grama, and A. C. T. van Duin, "The reaxff reactive force-field: development, applications and future directions," *npj Computational Materials*, vol. 2, no. 1, pp. 2057–3960, 2016.

[92] M. Born and R. Oppenheimer, "Zur quantentheorie der molekeln," *Annalen der Physik*, vol. 389, no. 20, pp. 457–484, 1927.

[93] D. R. Hartree, "The wave mechanics of an atom with a non-coulomb central field. part i. theory and methods," *Mathematical Proceedings of the Cambridge Philosophical Society*, vol. 24, no. 1, p. 89–110, 1928.

[94] V. Fock, "Näherungsmethode zur lösung des quantenmechanischen mehrkörperproblems," *Zeitschrift für Physik*, vol. 61, pp. 126–148, Jan 1930.

[95] J. C. Slater, "The theory of complex spectra," *Phys. Rev.*, vol. 34, pp. 1293–1322, Nov 1929.

[96] I. Shavitt, *The Method of Configuration Interaction*, pp. 189–275. Boston, MA: Springer US, 1977.

[97] L. H. Thomas, "The calculation of atomic fields," *Mathematical Proceedings of the Cambridge Philosophical Society*, vol. 23, no. 5, p. 542–548, 1927.

[98] E. Fermi, "Un metodo statistico per la determinazione di alcune proprietà dell' atomo," *Rend. Accad. Naz.Lincei*, vol. 6, p. 602–607, 1927.

[99] P. Hohenberg and W. Kohn, "Inhomogeneous electron gas," *Phys. Rev.*, vol. 136, pp. B864–B871, Nov 1964.

[100] R. M. Martin, *Density functional theory: foundations*, p. 119–134. Cambridge University Press, 2004.

[101] M. Levy, "Universal variational functionals of electron densities, first-order density matrices, and natural spin-orbitals and solution of the v-representability problem," *Proceedings of the National Academy of Sciences*, vol. 76, no. 12, pp. 6062–6065, 1979.

[102] M. Levy, "Electron densities in search of hamiltonians," *Physical Review A*, vol. 26, no. 3, p. 1200, 1982.

[103] E. H. Lieb, "Density functionals for coulomb systems," in *Inequalities*, pp. 269–303, Springer, 2002.

[104] W. Kohn and L. J. Sham, "Self-consistent equations including exchange and correlation effects," *Phys. Rev.*, vol. 140, pp. A1133–A1138, Nov 1965.

[105] J. P. Perdew, K. Burke, and M. Ernzerhof, "Generalized gradient approximation made simple," *Phys. Rev. Lett.*, vol. 77, pp. 3865–3868, Oct 1996.

[106] J. Paier, R. Hirschl, M. Marsman, and G. Kresse, "The perdew–burke–ernzerhof exchange-correlation functional applied to the g2-1 test set using a plane-wave basis set," *The Journal of Chemical Physics*, vol. 122, no. 23, p. 234102, 2005.

[107] J. Heyd, G. E. Scuseria, and M. Ernzerhof, "Hybrid functionals based on a screened coulomb potential," *The Journal of Chemical Physics*, vol. 118, no. 18, pp. 8207–8215, 2003.

[108] J. Heyd, G. E. Scuseria, and M. Ernzerhof, "Erratum: "hybrid functionals based on a screened coulomb potential" [j. chem. phys. 118, 8207 (2003)]," *The Journal of Chemical Physics*, vol. 124, no. 21, p. 219906, 2006.

[109] A. Tkatchenko and M. Scheffler, "Accurate molecular van der waals interactions from ground-state electron density and free-atom reference data," *Phys. Rev. Lett.*, vol. 102, p. 073005, Feb 2009.

[110] P. Gori-Giorgi, F. Sacchetti, and G. B. Bachelet, "Analytic static structure factors and pair-correlation functions for the unpolarized homogeneous electron gas," *Phys. Rev. B*, vol. 61, pp. 7353–7363, Mar 2000.

[111] U. von Barth and L. Hedin, "A local exchange-correlation potential for the spin polarized case. i," *Journal of Physics C: Solid State Physics*, vol. 5, pp. 1629–1642, jul 1972.

[112] G. D. Mahan, *Many Particle Physics, Third Edition.* New York: Plenum, 2000.

[113] W. Hoheisel, V. Colvin, C. Johnson, and A. Alivisatos, "Threshold for quasicontinuum absorption and reduced luminescence efficiency in cdse nanocrystals," *The Journal of chemical physics*, vol. 101, no. 10, pp. 8455–8460, 1994.

[114] J. P. Perdew and M. Levy, "Physical content of the exact kohn-sham orbital energies: Band gaps and derivative discontinuities," *Phys. Rev. Lett.*, vol. 51, pp. 1884–1887, Nov 1983.

[115] L. J. Sham and M. Schlüter, "Density-functional theory of the energy gap," *Phys. Rev. Lett.*, vol. 51, pp. 1888–1891, Nov 1983.

[116] E. Wigner, "Effects of the electron interaction on the energy levels of electrons in metals," *Transactions of the Faraday Society*, vol. 34, pp. 678–685, 1938.

[117] G. I. Csonka, J. P. Perdew, A. Ruzsinszky, P. H. T. Philipsen, S. Lebègue, J. Paier, O. A. Vydrov, and J. G. Ángyán, "Assessing the performance of recent density functionals for bulk solids," *Phys. Rev. B*, vol. 79, p. 155107, Apr 2009.

[118] J. Harl, L. Schimka, and G. Kresse, "Assessing the quality of the random phase approximation for lattice constants and atomization energies of solids," *Phys. Rev. B*, vol. 81, p. 115126, Mar 2010.

[119] F. Herman, J. P. Van Dyke, and I. B. Ortenburger, "Improved statistical exchange approximation for inhomogeneous many-electron systems," *Phys. Rev. Lett.*, vol. 22, pp. 807–811, Apr 1969.

[120] S.-k. MA and K. A. BRUECKNER, "Correlation energy of an electron gas with a slowly varying high density," *Phys. Rev.*, vol. 165, pp. 18–31, Jan 1968.

[121] A. D. Becke, "Density-functional exchange-energy approximation with correct asymptotic behavior," *Phys. Rev. A*, vol. 38, pp. 3098–3100, Sep 1988.

[122] J. P. Perdew and Y. Wang, "Accurate and simple analytic representation of the electron-gas correlation energy," *Phys. Rev. B*, vol. 45, pp. 13244–13249, Jun 1992.

[123] A. D. Becke, "A new mixing of hartree–fock and local density-functional theories," *The Journal of Chemical Physics*, vol. 98, no. 2, pp. 1372–1377, 1993.

[124] A. D. Becke, "Density-functional thermochemistry. iii. the role of exact exchange," *The Journal of Chemical Physics*, vol. 98, no. 7, pp. 5648–5652, 1993.

[125] C. Adamo and V. Barone, "Toward reliable density functional methods without adjustable parameters: The pbe0 model," *The Journal of Chemical Physics*, vol. 110, no. 13, pp. 6158–6170, 1999.

[126] J. D. v. d. J. D. Waals, "Over de continuiteit van den gas- en vloeistoftoestand," 1873. Thesis–Leyden.

[127] R. Eisenschitz and F. London, "Über das verhältnis der van der waalsschen kräfte zu den homöopolaren bindungskräften," *Zeitschrift für Physik*, vol. 60, pp. 491–527, Jul 1930.

[128] F. London, "The general theory of molecular forces," *Trans. Faraday Soc.*, vol. 33, pp. 8b–26, 1937.

[129] F. London, "Zur theorie und systematik der molekularkräfte," *Zeitschrift für Physik*, vol. 63, pp. 245–279, Mar 1930.

[130] X. Chu and A. Dalgarno, "Linear response time-dependent density functional theory for van der waals coefficients," *The Journal of Chemical Physics*, vol. 121, no. 9, pp. 4083–4088, 2004.

[131] F. L. Hirshfeld, "Bonded-atom fragments for describing molecular charge densities," *Theoretica chimica acta*, vol. 44, pp. 129–138, Jun 1977.

[132] A. Tkatchenko, R. A. DiStasio, R. Car, and M. Scheffler, "Accurate and efficient method for many-body van der waals interactions," *Phys. Rev. Lett.*, vol. 108, p. 236402, Jun 2012.

[133] Private communication with M.R. Shirts.

[134] https://www.mpcdf.mpg.de/services/computing/cobra/about-the-system.

[135] L. Rowley, D. Nicholson, and N. Parsonage, "Grand ensemble monte carlo studies of physical adsorption," *Molecular Physics*, vol. 31, no. 2, pp. 365–387, 1976.

[136] R. B. Wexler, T. Qiu, and A. M. Rappe, "Automatic prediction of surface phase diagrams using ab initio grand canonical monte carlo," *The Journal of Physical Chemistry C*, vol. 123, no. 4, pp. 2321–2328, 2019.

[137] J. Nicolas, K. Gubbins, W. Streett, and D. Tildesley, "Equation of state for the lennard-jones fluid," *Molecular Physics*, vol. 37, no. 5, pp. 1429–1454, 1979.

[138] J. K. Johnson, J. A. Zollweg, and K. E. Gubbins, "The lennard-jones equation of state revisited," *Molecular Physics*, vol. 78, no. 3, pp. 591–618, 1993.

[139] J. Kolafa and I. Nezbeda, "The lennard-jones fluid: An accurate analytic and theoretically-based equation of state," *Fluid Phase Equilibria*, vol. 100, pp. 1–34, 1994.

[140] Y. Tang and B. C.-Y. Lu, "Phase equilibria study of lennard–jones mixtures by an analytical equation of state," *Fluid phase equilibria*, vol. 165, no. 2, pp. 183–196, 1999.

[141] W. Okrasinski, M. Parra, and F. Cuadros, "Mathematical modeling of the vle curve of lennard-jones fluids. application to calculating the vapour pressure," *Physics Letters A*, vol. 282, no. 1-2, pp. 36–42, 2001.

[142] M. A. Van der Hoef, "Free energy of the lennard-jones solid," *The Journal of Chemical Physics*, vol. 113, no. 18, pp. 8142–8148, 2000.

[143] M. A. van der Hoef, "Gas–solid coexistence of the lennard-jones system," *The Journal of chemical physics*, vol. 117, no. 10, pp. 5092–5093, 2002.

[144] G. Bussi, D. Donadio, and M. Parrinello, "Canonical sampling through velocity rescaling," *The Journal of Chemical Physics*, vol. 126, no. 1, p. 014101, 2007.

[145] M. Bonomi, D. Branduardi, G. Bussi, C. Camilloni, D. Provasi, P. Raiteri, D. Donadio, F. Marinelli, F. Pietrucci, R. A. Broglia, and M. Parrinello, "Plumed: A portable plugin for free-energy calculations with molecular dynamics," *Computer Physics Communications*, vol. 180, no. 10, pp. 1961 – 1972, 2009.

[146] K. Nakazawa, "Recrystallization of amorphous silicon films deposited by low-pressure chemical vapor deposition from si2h6 gas," *Journal of Applied Physics*, vol. 69, no. 3, pp. 1703–1706, 1991.

[147] P. A. Breddels, H. Kanoh, O. Sugiura, and M. Matsumura, "Chemical vapour deposition of amorphous silicon with silanes for thin film transistors –the influence of the amorphous silicon deposition temperature–," *Japanese Journal of Applied Physics*, vol. 30, no. 2R, p. 233, 1991.

[148] S. Bhattacharya, S. V. Levchenko, L. M. Ghiringhelli, and M. Scheffler, "Stability and metastability of clusters in a reactive atmosphere: Theoretical evidence for unexpected stoichiometries of mg m o x," *Physical review letters*, vol. 111, no. 13, p. 135501, 2013.

[149] H. Lischka and H. J. Koehler, "Ab initio investigation on the lowest singlet and triplet state of disilyne (Si2H2)," *Journal of the American Chemical Society*, vol. 105, no. 22, pp. 6646–6649, 1983.

[150] K. W. KOŁASIŃSKI, "DYNAMICS OF HYDROGEN INTERACTIONS WITH Si(100) AND Si(111) SURFACES," *International Journal of Modern Physics B*, vol. 09, no. 21, pp. 2753–2809, 1995.

[151] J. J. Boland, "Scanning tunnelling microscopy of the interaction of hydrogen with silicon surfaces," *Advances in Physics*, vol. 42, no. 2, pp. 129–171, 1993.

[152] M. Ceriotti, G. A. Tribello, and M. Parrinello, "Demonstrating the transferability and the descriptive power of sketch-map," *J. Chem. Theory Comput.*, vol. 9, p. 1521, March 2013.

[153] R. E. Schlier and H. E. Farnsworth, "Structure and adsorption characteristics of clean surfaces of germanium and silicon," *The Journal of Chemical Physics*, vol. 30, no. 4, pp. 917–926, 1959.

[154] G. Le Lay, A. Cricenti, C. Ottaviani, P. Perfetti, T. Tanikawa, I. Matsuda, and S. Hasegawa, "Evidence of asymmetric dimers down to 40 k at the clean si(100) surface," *Phys. Rev. B*, vol. 66, p. 153317, Oct 2002.

[155] M. Ono, A. Kamoshida, N. Matsuura, E. Ishikawa, T. Eguchi, and Y. Hasegawa, "Dimer buckling of the si(001)2×1 surface below 10 k observed by low-temperature scanning tunneling microscopy," *Phys. Rev. B*, vol. 67, p. 201306, May 2003.

[156] K. Hata, S. Yoshida, and H. Shigekawa, "$p(2\times2)$ phase of buckled dimers of si(100) observed on n-type substrates below 40 k by scanning tunneling microscopy," *Phys. Rev. Lett.*, vol. 89, p. 286104, Dec 2002.

[157] R. A. Wolkow, "Direct observation of an increase in buckled dimers on si(001) at low temperature," *Phys. Rev. Lett.*, vol. 68, pp. 2636–2639, Apr 1992.

[158] https://gitlab.com/zhouyuanyuan/fhi-panda.

[159] D. Berger, A. J. Logsdail, H. Oberhofer, M. R. Farrow, C. R. A. Catlow, P. Sherwood, A. A. Sokol, V. Blum, and K. Reuter, "Embedded-cluster calculations in a numeric atomic orbital density-functional theory framework," *The Journal of Chemical Physics*, vol. 141, no. 2, p. 024105, 2014.

[160] D. A. Kofke and E. D. Glandt, "Monte carlo simulation of multicomponent equilibria in a semigrand canonical ensemble," *Molecular Physics*, vol. 64, no. 6, pp. 1105–1131, 1988.

[161] W. S. R. C. G. H. O. L. S. Curtarolo, D. Morgan, "Aflow: software for high-throughput calculations of materials properties,"

[162] A. Jain, G. Hautier, C. J. Moore, S. P. Ong, C. C. Fischer, T. Mueller, K. A. Persson, and G. Ceder, "A high-throughput infrastructure for density functional theory calculations," *Computational Materials Science*, vol. 50, no. 8, pp. 2295 – 2310, 2011.

[163] J. E. Saal, S. Kirklin, M. Aykol, B. Meredig, and C. Wolverton, "Materials design and discovery with high-throughput density functional theory: The open quantum materials database (oqmd)," *JOM*, vol. 65, pp. 1501–1509, Nov 2013.

[164] D. D. Landis, J. S. Hummelshøj, S. Nestorov, J. Greeley, M. Dułak, T. Bligaard, J. K. Nørskov, and K. W. Jacobsen, "The computational materials repository," *Computing in Science Engineering*, vol. 14, pp. 51–57, Nov 2012.

[165] S. Lorenz, A. Groß, and M. Scheffler, "Representing high-dimensional potential-energy surfaces for reactions at surfaces by neural networks," *Chemical Physics Letters*, vol. 395, no. 4, pp. 210 – 215, 2004.

[166] G. Hautier, C. C. Fischer, A. Jain, T. Mueller, and G. Ceder, "Finding nature's missing ternary oxide compounds using machine learning and density functional theory," *Chemistry of Materials*, vol. 22, no. 12, pp. 3762–3767, 2010.

[167] W. J. Szlachta, A. P. Bartók, and G. Csányi, "Accuracy and transferability of gaussian approximation potential models for tungsten," *Phys. Rev. B*, vol. 90, p. 104108, Sep 2014.

[168] T. Mueller, E. Johlin, and J. C. Grossman, "Origins of hole traps in hydrogenated nanocrystalline and amorphous silicon revealed through machine learning," *Phys. Rev. B*, vol. 89, p. 115202, Mar 2014.

[169] K. T. Schütt, H. Glawe, F. Brockherde, A. Sanna, K. R. Müller, and E. K. U. Gross, "How to represent crystal structures for machine learning: Towards fast prediction of electronic properties," *Phys. Rev. B*, vol. 89, p. 205118, May 2014.

[170] L. M. Ghiringhelli, J. Vybiral, S. V. Levchenko, C. Draxl, and M. Scheffler, "Big data of materials science: Critical role of the descriptor," *Phys. Rev. Lett.*, vol. 114, p. 105503, Mar 2015.

[171] L. M. Ghiringhelli, J. Vybiral, E. Ahmetcik, R. Ouyang, S. V. Levchenko, C. Draxl, and M. Scheffler, "Learning physical descriptors for materials science by compressed sensing," *New Journal of Physics*, vol. 19, no. 2, p. 023017, 2017.

[172] R. Ouyang, S. Curtarolo, E. Ahmetcik, M. Scheffler, and L. M. Ghiringhelli, "Sisso: A compressed-sensing method for identifying the best low-dimensional descriptor

in an immensity of offered candidates," *Phys. Rev. Materials*, vol. 2, p. 083802, Aug 2018.

[173] R. Ouyang, E. Ahmetcik, C. Carbogno, M. Scheffler, and L. M. Ghiringhelli, "Simultaneous learning of several materials properties from incomplete databases with multi-task SISSO," *Journal of Physics: Materials*, vol. 2, p. 024002, mar 2019.

[174] J. K. Johnson, J. A. Zollweg, and K. E. Gubbins, "The lennard-jones equation of state revisited," *Molecular Physics*, vol. 78, no. 3, pp. 591–618, 1993.

[175] A. Ramstad, G. Brocks, and P. J. Kelly, "Theoretical study of the Si(100) surface reconstruction," *Phys. Rev. B*, vol. 51, pp. 14504–14523, May 1995.